Effects of Superbubbles on Near-IR and Sub-millimeter Polarization

A DISSERTATION
SUBMITTED TO THE FACULTY OF THE GRADUATE SCHOOL
OF THE UNIVERSITY OF MINNESOTA
BY

Jennifer Amanda Delgado

IN PARTIAL FULFILLMENT OF THE REQUIREMENTS
FOR THE DEGREE OF
Doctor of Philosophy

Terry J. Jones and Thomas W. Jones

May, 2013

© Jennifer Amanda Delgado 2013
ALL RIGHTS RESERVED

Acknowledgements

I'm fairly certain that the Acknowledgments are the most-read portion of a thesis. Since I think at least part of this is just people looking for their own names[1] I decided to provide an outline of sorts. In the first part I thank my advisors and other faculty, then staff from Physics and Astronomy and also MSI followed by graduate students. Finally, I thank family members.

I found out my advisors Terry Jones and Tom Jones had more in common than a last name whenever they would meet with me together. What they seemed to have most in common with each other was the kind of patience that can only come from telling someone something that the speaker knows the listener is just going to have to find out for themselves. I know that my stubbornness and desire to race ahead and solve complex problems before I had solved the simple problems tried their patience. I fixedly wandered off into dead ends and mistakes, repeatedly, due to my inability to acknowledge their experience and expertise. I really can't thank either of them enough for not only letting me make these mistakes, since I think it's the only way I am able to learn some things, but more importantly for being just as willing to help me understand whatever problem I was trying to tackle as they were the first time I asked for their help and didn't take their advice! Though their guidance on this project dealt with very different areas of astronomy, both of my advisors taught me how to better approach problems. Thank you Terry and Tom, for having the humor, patience and insight to help me learn to *just start with something 'simple.'*

I would also like to thank my current and former committee members. A big, job-saving, thank you is due to Lucy Fortson for agreeing to be on my committee on short notice even when I know you already had a full schedule. Thank you to Cynthia Cattell

[1] Or that is just me.

for being on my committee for my preliminary orals. Evan Skillman was always a source of humorous honesty and apparently, Care Bear DVDS. I'm thankful that he gave me the opportunity to be UITP director.

Larry Rudnick was incredibly helpful to my development as an instructor. He clearly cares about teaching effectively and was very helpful through our multiple discussions for Outreach and teaching duties in getting me to think about how I could better teach and communicate. Liliya Williams deserves all kind of thanks for constantly dealing with my various half-baked ideas relating to the Astronomy 1001 course and outreach. She even endured my less than awesome driving skills to fulfill and outreach when we really needed the help. Paul Woodward was always very generous with the wonderful resources of the LCSE. I would also like to thank Aigen Li and Angela Speck at the University of Missouri. They both encouraged me to give astronomy research a try. In particular Aigen put me on the path to studying astronomical dust.

Terry Thibeault fixed every problem I ever caused for her and even some of the ones I caused for myself. She pulled the magic strings of the administrative spider web for me every time I was too clumsy and became tangled. I would not be graduating without her willingness to help me. Thank you to Corinne Komor for all her help with funding. Julie Murphy gave me a key to the room I felt most comfortable at Tate in after Calvin was born. The MSI technical and scientific help staff dealt with all of my cryptic and confusing email requests. In particular Shuxia Zhang made sure my 'big runs' actually ran. David Porter beyond his contributions to WOMBAT patiently endured my requests for executables and questions about source codes. Mike Knox endured countless emails asking for information he had already given me at some point. He also reset my password more times than I would like to admit when I forgot it.

I would be horribly ungrateful to not thank my fellow graduate students, past and present. Kyle Neary, Jake Simones and Ted Wahl drew me into some of the most ridiculous and amusing arguments and conversations I've ever had. They and Karl Isensee, Steve Warren, Damon Farnsworth, Sklyer Grammer, Danielle Berg, Dinesh Shenoy and Karlen Shahinyan made Friday afternoons completely unproductive in the best way possible. I miss Friday beers even though I never really liked the beer. Chelsea Tiffany and Andrea Mehner let me hide in the APS lab and ramble about nonsense my first few years. Barun Dhar gave me a reason to keep visiting the APS after they had

left. I never did get him to do any outreach, but his responses still cheered me up! Andrew Helton showed me how to run the department's telescope on Mt Lemon, my only real observing run.

The graduate students who have had the largest influence on me are Tom's other students. Andrew Johnson was a great person to get lunch with when we couldn't find enough free food near our office. He can't draw squares, but he was a great person to talk to when my ideas needed a sounding board. I thought of Paul Edmon and Pete Mendygral as 'academic big brothers.' They were always there to help me with the ins and outs of computational work and the physics of MHD. They even gave me a mock run through of my preliminary orals questioning. I would not have a thesis if Pete had not written WOMBAT or GRIZZLYEYE. Nor would I have one if he had not been so willing to help me through all the problems I ran into trying to get my own research accomplished with his codes (my faults, not his). I really could not have asked for a better group of people to work with and I genuinely look forward to continuing work on WOMBAT 2.

My grandparents, Gay, Diane and Robert really encouraged me throughout this thesis and during my years as a graduate student. Phone calls from my uncle Tommy inspired me think positively as well. My brother Justin was awesome for making me feel like what I was doing was awesome even when the work he is doing literally protects lives. I'm so proud of him!

My parents are incredibly supportive and helpful. They always made me feel like my accomplishments were important to them, even if it was just getting 2nd place in "Reach for the Stars." I know that if they hadn't babysat Calvin for that last week, this thesis would not exist.

My step-son Grant came to UITPs, summer lectures, regular work days and even my defense and endured it all without complaint. He is the most patient and helpful child (now teenager!) that I have ever had the pleasure of knowing. I'm sorry my experience has convinced him to never try for a PhD, but I know he'll find something that he'll love doing. Calvin had to share my attention with my laptop all too often, but I'm so glad I've gotten to stay home with him! I would say he's probably gotten more accomplished this last year than I did.

Finally, I owe a huge debt of gratitude to my husband Arturo. You not only moved to

"Minnesnowta" for me, despite your hatred of cold, you endured my stubborn, obsessive and often erratic personality about work and school. I love you. Thank you for being my best friend, even when I was not the best of friends.

Dedication

To my parents who got me started, to Arturo who kept me going and to Justin, Grant and Calvin who gave me a reason to finish.

Abstract

Associations of young, massive stars can collectively energize the interstellar medium through stellar winds and SNII. The energy injected into the ISM can produce large regions of hot, diffuse gas surrounded by a swept-up dense shell of gas, dust and magnetic fields. Such structures are often termed 'superbubbles' and the change they produce in local galactic magnetic field geometry could be detectable in polarization observations. We create semi-analytical models and large 3D MHD numerical simulations of superbubbles in plane-parallel galactic atmospheres in order to produce synthetic polarization maps in 100 micron polarized dust emission and 2.2 micron starlight polarized by transmission through dust. Polarization maps that included galactic contributions to the polarization were also created. We find that luminous superbubbles that 'breakthrough' the galactic plane could produce polarization signature that is observable for favorable lines of sight.

Contents

List of Tables

List of Figures

Chapter 1

Introduction

In broad terms the purpose of this thesis is to relate theoretical understanding with observations. More specifically we create semi-analytical and numerical models of a theoretical object called a 'superbubble' in a segment of a spiral galaxy. These models are used to predict the change in and detectability of superbubbles in near-IR and dust emission polarization maps. The goal is to create maps useful to observers in understanding the role superbubbles might play in affecting polarization observations. Section §1.1 will cover the theory of superbubbles and some the observational evidence for them, §1.2 will provide a brief description of the environment in which superbubbles are located, §1.3 will detail more of the motivation for this work. An outline for the thesis is also given.

1.1 Superbubbles

O and B stars are the hottest, most luminous and most massive of all stars. They live very short lifetimes, some as short as a few million years though lifetimes of a few tens of millions of years is possible. It is expected that the majority of OB stars form in groups called OB associations. Surrounding these stars are regions of ionized gas [1] which are produced by large number of ionizing photons from the stars themselves. Additionally, as these massive stars age, the tremendous luminosities they produce leaves them susceptible to mass loss from line driven winds. Such winds can pour dramatic

[1] HII regions

amounts of kinetic energy into the ISM, with wind speeds of a few $10^3 kms^{-1}$ and mass loss rates of $10^{-6} M_{\odot} yr^{-1}$ Castor et al. (1975b). Additionally, such stars affect the ISM in their deaths as supernova type II. Stars that end their lives as SNII release $10^{51} ergs$ of energy in one massive explosion that shocks the surrounding ISM.

The relatively short lifetimes of these stars means that without a large natal kick, they can live and die in much the same location in which they were born. The expected result of this is that the energy produced by these stars is put into the ISM in a small region of space in a short amount of time. With a dozen or so of such stars, more than $10^{52} ergs$ of energy could be released into a few parsecs on the order of 10 million years. Luminosities for superbubbles are expected to range between $10^{37} ergss^{-1}$ to $10^{39} ergss^{-1}$ depending on star formation rates. The released energy accelerates and ionizes the surrounding ISM to create a hot, low density bubble surrounded by a dense, possibly strongly cooled shell of shocked ISM. We call the region of ISM affected by this combined stellar activity a superbubble. [2] The energy of a superbubble drives the gas, dust and magnetic fields out away from the OB association location, shocks the gas and compresses and displaces the magnetic fields while changing the field orientation.

In a stratified atmosphere the pressure and density gradient provide less resistance to the superbubble's expansion leading to preferential growth perpendicular to the plane which could lead to the escape of heated superbubble material from the disk of the galaxy into the halo (eg. Tomisaka & Ikeuchi (1986), Mac Low & McCray (1988)). We adopt a modified classification scheme from Heiles (1990), defining 'breakthrough' superbubbles as those that grow to sizes larger than the effective scale height of the disk and become elongated perpendicular to the plane of the gas. Such bubbles do not necessarily 'blow out', which Heiles (1990) define as communication with the halo. It is possible that the magnetic field would be drastically affected and be transformed from lying largely in the plane of the galaxy to a geometry with significant components perpendicular to the plane for breakthrough and breakout superbubbles.

[2] Chu (2008) defines a bubble as the product of one star, a superbubble as the product of one OB association and a supergiant shell as the product of more than one OB association. For this work we ignore this distinction. We only consider the products of more than one star, but may refer to this as a bubble or superbubble.

1.2 The ISM and Galactic Magnetic Fields

The interstellar medium is the collective energy and matter that exists surrounding stars in galaxies. It is composed of radiation, ionized, atomic and molecular gas, 'dust', magnetic fields and cosmic rays. Stars constantly recycle the ISM through their birth, life and death, a process by which elements heavier than Lithium are produced. We will focus on the ISM as it is currently understood in the Milky Way and generalize this to spiral-type galaxies.

The ISM is thought to have the following components: cold ($< 10K$) and dense ($> 100cm^{-3}$) dark clouds of molecular hydrogen, cold ($10 - 100K$) and diffuse ($> 10cm^{-3}$) clouds of neutral atomic hydrogen, warm ($\sim 10^4K$) neutral and ionized inter-cloud medium with densities of $< 1cm^{-3}$ and hot ($\sim 10^6K$) ionized inter-cloud medium with densities of $< 0.1cm^{-3}$ or in HII regions $100cm^{-3}$ Ferrière (2001).

For this work we primarily focus on the warm neutral and ionized inter-cloud medium. Clouds are ignored because of their small volume, though we quasi-include the mass present in these clouds by increasing the central density in our modeled atmosphere (see section 2.2.2).

The magnetic field in spiral type galaxies is thought to lie predominately parallel the plane. The field geometry in the plane is largely toroidal, though closely aligned with spiral arm structure Beck (2009).

For our analysis we consider only scenarios where diffusion of the magnetic field is ignorable. The large physical scales and low resistivity of the ISM mean that the magnetic Reynolds number is large enough to assume a 'frozen-in field.' This is true even for a very poorly ionized medium with ionization fractions as low as 10^{-3}. Field strengths relevant for the ISM, (on the order of a few microGauss) and densities of about $1cm^{-3}$ mean that the ambipolar diffusion timescale remains within an order of magnitude of the sound crossing time. Ambipolar diffusion timescales shorter than the sound crossing time would mean that the magnetic field could not be expected to remain frozen-in. Such diffusion of the magnetic field could make it more difficult to produce vertical field components. With the ions remaining largely coincident with the neutral gas, the field will also be coincident with the neutral gas. This is also important in justifying our use of ideal MHD to simulate superbubbles.

1.3 Motivation and Science Goals

Elongated dust grains in the ISM align themselves perpendicularly to the magnetic field Davis & Greenstein (1951). This alignment enables mapping of the field geometry through observed polarization of light emitted from and extinguished by these grains. For this work we will focus on creating two types of synthetic polarization observations, near-IR transmitted starlight which is selectively extinguished by the dust and sub-millimeter light emitted by the dust.

The goals for this work are three-fold.

1) Gain a better understanding of the interaction of superbubbles with the ISM, most importantly with the magnetic field.

2) Predict the detectability of superbubbles in near-IR and sub-millimeter polarization, and characterize this detection.

3) Determine the efficacy of superbubbles in reproducing polarization observations attributed to them.

Though the current picture of the ISM magnetic fields is improving, a fundamental theoretical understanding of the role magnetic fields play in the evolution of galaxies is still lacking Beck (2009). Superbubbles provide an important link in our understanding the of the evolution of star clusters to the evolution of the ISM and galactic magnetic fields as a whole de Avillez & Breitschwerdt (2005). Recent work has focus on modeling the turbulent nature of the ISM and the role supernova and superbubbles play in generating driving energy for this turbulence (eg. Korpi et al. (1999)). Some of this work has also explored the generation of galactic fields from this turbulence (eg. de Avillez & Breitschwerdt (2005)). However, as mentioned by Stil et al. (2009) it is difficult to relate these papers to specific objects. With a simpler model it can be easier to isolate the relevant physics in observations and build our understanding of more complex cases from the simple ones.

There is already significant work on the development of a single superbubble in the ISM (eg. Mac Low & McCray (1988), Tenorio-Tagle et al. (1990)) and its affects on the galactic magnetic field (eg. Tomisaka (1992), Ferriere et al. (1991)) though these have been limited in their number of dimensions or the time they allow the simulation

to evolve. More recent work Stil et al. (2009) modeled a three-dimensional superbubble with and without cooling, but was limited in resolution and likely suffered from numerical instabilities.

There have also been attempts at predicting the observational signatures of superbubbles. Notably, Basu et al. (1999) create synthetic observations of superbubble W4 in H α by calculating the shape of a Kompaneet's-like superbubble, its shell thickness and shell density in an exponentially stratified atmosphere. Predictions about observations relating to the magnetic field have also been made. Rotation measure maps were produced by Stil et al. (2009). Kothes & Brown (2009) show that supernova remnants have an expected signature in radio polarization measurements. However, there is a dearth of work on how starlight polarized by dust or polarized dust emission is affected by superbubble development.

With the large scale surveys that will map the Galaxy in polarized starlight and polarized dust emission theoretical work for these types of polarization is necessary. Missions to study the CMB such as Planck and EBEX will observe, at relatively high angular resolution, the galactic polarized dust emission as foregrounds to the CMB (see The Planck Collaboration (2006), and Reichborn-Kjennerud et al. (2010)). These observations can then be used to study galactic fields through the polarized dust emission created by elongated, cool (10-50K) sub-micron sized grains in the ISM radiating in the sub-millimeter. We are interested in characterizing the observable effects of a superbubble on the structure of the Milky Way's magnetic field in order to connect observed polarized emission with a theoretical understanding of the effects of a superbubble's evolution into the ISM.

Additionally, GPIPS, the Galactic Plane Infrared Polarization Survey will take about 1 million linear stellar polarization measurements in the H-band (1.6 microns) over a 76 square degree area of the sky. The stated goals of the survey include the desire to understand the role of the magnetic field in the galaxy Clemens et al. (2012). This thesis can provide the preliminary groundwork to relating such large scale observations to specific theories about stellar feedback and how it affects the galactic field.

Some galaxies like M82 show evidence for vertical components to their magnetic fields in the disk. The vertical components present in M82 can be seen in near-IR band polarimetry (Jones (2000)). The presence of a vertical magnetic field in M82,

which has a very prominent bipolar outflow from the center, suggests that superbubbles that are capable of breaking out of the disk are also capable of dragging the magnetic field along to create a vertical field. Transmission of starlight through this region of vertical field geometry will polarize the light perpendicular to the polarization from the intervening disk, causing a net reduction in total observed polarization. Jones (1993) used this interpretation to explain the low polarization seen in several galaxies with lower fractional polarization. This model was also invoked by Jones (1997) to explain the anomalously low polarization and peculiar position angle geometry in NGC 891. The polarization angle found by Jones (1997) shows good agreement with radio synchrotron emission from Sukumar & Allen (1991). The agreement between the two position angles, that should be perpendicular to each other, is a strong confirmation that the near infrared polarimetry is measuring the interesting magnetic field geometry in NGC 891.

In Chapter 2 we describe the methods used to create our simulations and synthetic images. Chapter 3 outlines the theoretical development of a superbubble before breakthrough, particularly determining the properties that will most affect near-IR and sub-millimeter dust polarization. Chapter 4 explores the consequences of a stratified atmosphere on superbubble development. Chapter 5 discusses the numerical simulations preformed and what insight these simulations can provide about individual superbubbles on interstellar and dust emission polarization. Chapter 6 discusses some of the results of this work as well as some conclusions and future work.

Chapter 2

Methods

This thesis requires the creation and use of many computational methods. This chapter will provide a reference for these techniques. This chapter is split into two main sections, section §2.1 discusses the changes made to the ray casting synthetic observation generator GRIZZLYEYE, with subsections on non-parallel lines of sight (§2.1.1), dust polarization (§2.1.2) and image foreground and background additions (§2.1.3). Section §2.2 details the setup and methods used for numerical modeling superbubbles in a Milky Way -like galactic environment. The subsections are: a brief discussion of the 3D MHD code used for our simulations, WOMBAT (§2.2.1), atmosphere initialization (§2.2.2), galactic magnetic field configuration (§2.2.3) and superbubble energy and mass injection (§2.2.4).

2.1 Method of Synthetic Image Generation: GRIZZLYEYE

Synthetic observations of the superbubble simulations were made using a rewritten version of the code GRIZZLYEYE. In this section we will discuss the original code, the need for modification and the rewrite and supplementation of the code. GRIZZLYEYE [1] is a ray casting code developed by Pete Mendygral (Mendygral, 2011). One of the advantages of using this code for creating synthetic images of the superbubble

[1] hereafter GE 1.0 will refer to the first version of this code, while GRIZZLYEYE will refer to the modified version used for this thesis

simulations is that GE 1.0 was built specifically for the output from WOMBAT. This is useful because the entire framework for reading in information from simulations for this work was already written. Another advantage of the code is that it is written with Open MP, allowing for load balancing of the work across a single computing node.

The basic structure of GE 1.0 is as follows. Simulation data is read in. What data is specifically read in is dependent on the type of observation to be performed. Three-dimensional arrays of quantities needed for radiative transfer integration such as emissivity and absorption are created using the read in data. The image is then created by looping over image axes to create a collection of cast rays that act as lines of sight. These lines of sight are numerically integrated to create an intensity value for each image location. It is important to note that image axes and coordinates are not necessarily aligned with data axes and coordinates; similarly pixel size does not correspond to simulation voxel size. This flexibility allows the user to view the simulation from any angle and also to define the resolution of the image.

It is important to note that the GE 1.0 code was designed for creating images of objects at cosmological distances and so used parallel rays for image production. This means that when defining the rays to be cast through the image, a single rotation was defined for all rays and the locations in the grid corresponding to positions along these rays are found using this one rotation.

A number of modifications were needed to make synthetic images for this thesis. The largest changes were non-parallel rays, polarization and the inclusion of foregrounds and backgrounds to read in data. The need for each of these is explained in this section. To create images at galactic distances with GE 1.0 it was necessary to keep the images very small in angular extent or risk violating the assumption of parallel lines of sight. However, large superbubbles can be several hundreds of parsecs to even a few kiloparsec in size Chu (2008). At a distance of 5 kpc, a superbubble extending 2 kpc will subtend over 20 degrees on the sky. To consider superbubbles closer than this would violate the assumption of parallel lines of sight in increasingly noticeable ways. Since we create synthetic images of superbubbles at closer distances than the parallel line of sight assumption would allow, a modification of GE 1.0 to include non-parallel line of sight integration was necessary.

More fundamental to this work was the inclusion of linear polarized radiative transfer. This is necessary because the unpolarized equation of radiative transfer has no way of tracking vector-like information, without which polarization observations of any kind are impossible. To understand galactic field geometries through polarization maps, linear polarized radiative transfer must be included. As dust emission requires modeling polarized emission and the transmission of starlight through aligned dust grains requires polarized absorption it was necessary to include both polarized emission and absorption in the new version of GRIZZLYEYE

For synthetic observations of superbubbles in our own galaxy the inclusion of foregrounds and backgrounds is crucial if our synthetic observations are to be useful for comparison with actual observations. By including foreground and background information it is also possible to investigate how distance to the superbubble affects its observational signature. It should also be noted that adding foreground information to the synthetic observations makes the use of non-parallel lines of sight mandatory for foregrounds extending to the location of the observer. Even for small images of superbubbles at large distances, the convergence of the lines of sight to the observer will ultimately lead to a noticeably incorrect use of the parallel approximation the closer the foreground components are to the observer.

2.1.1 Non-Parallel Lines of Sight

In this section we explain the methods used to create synthetic images using non-parallel lines of sight.

The 'camera' in GE 1.0 and GRIZZLYEYE has a default pointing in space oriented relative to the expected data. We'll call this unit vector $\vec{C}$. The camera location is then the separation distance between the camera and the data, l, multiplied by $\vec{C}$. The data used for creating synthetic images is assumed to be located at the origin of this vector. To view the data from different angles, we can rotate the camera vector to a new location. We define a rotation matrix $\mathbf{A}$ in data coordinates x, y and z such that the default camera location is located on the positive z axis looking toward the origin when this rotation matrix is equal to the identity matrix. To rotate the camera pointing we multiply the vector $\vec{C}$ by the rotation matrix $\mathbf{A}$ to produce vector $\vec{C}'$ to give the new camera location $l\vec{C}'$. The line of sight vector, $\vec{V}$, which passes through the data

coordinate origin is then integration path length D in the direction of the rotated vector: $\vec{V} = D\hat{C'}$. In the parallel case we could integrate along multiple rays cast parallel to this vector $\vec{V}$, however the non-parallel case will be more complex. The plane perpendicular to vector $\vec{V}$ (vector $\vec{V}$ would be parallel to the plane normal) is defined as the local 'image plane.'

In the non-parallel case in GRIZZLYEYE, the rays we will cast through the data will not be parallel, so it is necessary to trace multiple non-parallel vectors to produce an image. To create these non-parallel vectors we must take advantage of the fact that we are creating an image by artificially starting our line of sight integration somewhere, so to remain a self-consistent assumption each of the non-parallel vectors must have the same length over the solid angle that defines our image. We know this length to be the magnitude of vector $\vec{V}$. At the origin in image coordinates i and j (where the camera location, data origin and image origin all lie on a single line) the line of sight vector would lie parallel to the vector $\vec{V}$. The magnitude of any other line of sight vector must also have this magnitude, so a line of sight beginning any where not on the image coordinate origin would have to have a smaller component in the direction of vector $\vec{V}$ and some components in two other directions orthogonal to the line of sight vector. These orthogonal directions would define a new image plane. In fact, every location in the image would have its own line of sight vector and corresponding image plane.

The result of each line of sight having its own image plane is that the non-parallel case has a curved image surface, with the line of sight vectors converging at the camera location. Though the physical distance between each line of sight will change, the angular separation remains constant. The image plane corresponding to $\vec{V}$ we define as having the orthogonal vectors 'up' and 'right' $\vec{J_0}$ and $\vec{I_0}$ respectively. This image plane lies tangential to the image coordinate origin (i=0,j=0) and image coordinates are defined such that there is no rotation about the line of sight vector in the image plane defined by $\vec{J}$ and $\vec{I}$ from the plane defined by $\vec{J_0}$ and $\vec{I_0}$.

We can now define $\vec{U}$ as the vector pointing to a location in our data (or foreground or background) from the camera location. The direction of this vector will be in the opposite direction of our line of sight and defined from rotating our image plane normal

from the image plane normal defined for $\vec{V}$. $\vec{U}$ will make an angle:

$$\theta_i = (i - \frac{n_i}{2} - 0.5)\alpha \tag{2.1}$$

with $\vec{V}$ in the direction of $\vec{I_0}$ and an angle:

$$\theta_j = (i - \frac{n_j}{2} - 0.5)\alpha \tag{2.2}$$

with $\vec{V}$ in the direction of $\vec{J_0}$. Here α is the angular size of a pixel. It assumed that i has the range $-\frac{n_i}{2}$ to $\frac{n_i}{2}$ and j $-\frac{n_j}{2}$ to $\frac{n_j}{2}$ where n_i and n_j are the total number of pixels in the image.

The vector $\vec{U}$ will have a magnitude based on the number of integration steps remaining till the camera location is reached.

$$\vec{U} = D - n\vec{dl} \tag{2.3}$$

Where the magnitude of $\vec{dl}$ is the integration step size, and n is the number of integration steps taken.

Using vectors $\vec{V}$ and $\vec{U}$ we can determine the location of data to be used in our numerical integration. Vector $\vec{V}$ points from the origin to the camera location. Vector $\vec{U}$ points from the camera location to the data location. To get the vector $\vec{W}$ that points from the origin to the data location (necessary for the determination of what read-in data is needed) we can add these two vectors.

$$\vec{W} = \vec{U} + \vec{V} \tag{2.4}$$

All that remains is a conversion from physical units to integer counts corresponding to data array locations, which is simple as long as the physical size of a data voxel is known.

2.1.2 Polarization

In this section we detail the method for creating synthetic polarization from numerical integration for transmitted starlight and dust emission.

Unpolarized starlight is linearly polarized by being preferentially extinguished by elongated dust grains that are aligned by the local magnetic field. This extinction is due to the increased absorption and scattering when the electric field component of the light is parallel to the major axis of the grain. This results in light with a net polarization parallel to the grain's minor axis. Since grains align perpendicular to the field, the resultant polarization from transmitted starlight will lie parallel to the field Davis & Greenstein (1951).

Dust emission is produced by warm grains radiating as a blackbody at 30 K. Light emitted from the grain will be polarized parallel the grain's major axis. The grain's alignment perpendicular to the magnetic field means that the emitted light will be polarized perpendicular to the orientation of the field lines.

Both transmission and emission synthetic observations require information on the dust density and the orientation of the magnetic field. To create synthetic observations we need to create this information along each line of sight.

The gas distribution is used to estimate a dust density by assuming a gas to dust mass ratio of 100 to 1. For simplicity we ignore any variation in dust grain size or composition. Grains are always assumed to be perfectly aligned [2] . For this work we consider only sub-micron sized grains that will emit maximally in the sub millimeter (as blackbodies with temperatures of a few tens Kelvins) and scatter with increasing efficiency the shorter wavelengths. Dust grains are assumed to be largely silicates, with a density of roughly $2.5 gcm^{-3}$. [3] Using these fixed parameters, we find the mass of a dust grain, and using the mass ratio previously mentioned, we are able to estimate a grain number density. Having the number of grains in a set volume enables us to determine the column depth and volume emissivity necessary for our synthetic observations.

This is not intended to be a sophisticated attempt at modeling grains in radiative transfer, but a reasonable approximation of generalized dust properties in the ISM.

[2] We set the polarizing efficiency of each grain, however, from empirical values of observed polarization. Really we are lumping the degree of grain alignment and the individual grain polarizing properties into one value. Assuming grain alignment for the phase of the ISM we consider is not unreasonable, since it likely only in cold, dark clouds that grains lose alignment (see Draine (2003))

[3] Though silicates compose a large portion of the total dust grain composition Draine (2003), there are many additional contributions to dust in the ISM, including but not limited to water ice, carbon, iron and magnesium. The advantage in modeling our dust grains as silicate is that the density of silicate provides a rough average of the various contributing components.

In fact, since the observations we produce are only concerned with relative intensities even this level of sophistication is not really necessary. A more detailed exploration of dust grain size distribution and composition and the survivability of dust within and surrounding a superbubble is discussed by Everett & Churchwell (2010).

Transmission

For polarized transmission of starlight, synthetic observations are made by numerically integrating the equations describing the transfer of linearly polarized light from Jones & Odell (1977). The equations are

$$I = (I_0 cosh\tau_P + \zeta sinh\tau_P + I_{0,star})e^{-\tau} \tag{2.5}$$

$$Q = (I_P cos(2\theta) + Q_0)e^{-\tau} \tag{2.6}$$

$$U = (I_P sin(2\theta) + U_0)e^{-\tau} \tag{2.7}$$

$$I_P = I_0 sinh\tau_P + \zeta cosh\tau_P - \zeta \tag{2.8}$$

$$\zeta = Q_0 cos(2\theta) + U_0 sin(2\theta) \tag{2.9}$$

Where θ is the angle between the vertical line on the plane of the sky and the projected component of the magnetic field on the sky. τ_P is defined as:

$$\tau_P = \eta sin^2(\alpha)\tau \tag{2.10}$$

where α is defined as the angle between the magnetic field and the line of sight. This angle determines the efficiency of polarization for the orientation of a dust grain aligned with the magnetic field. A grain spinning around a field line that is parallel to the line of sight will produce no polarization, but one aligned on a magnetic field perpendicular to the line of sight will polarize light at the maximum efficiency of that grain.

In order to solve for τ and then τ_P , we use the gas density to define a column

depth for each integration step using the physical size of the step. This column depth is then used to define a visual extinction A_V by assuming $A_V = \frac{N_H}{1.87x10^{21}cm^2}$. This A_V is then used to define the extinction in the observation wavelength, λ by assuming an extinction law of $A_\lambda = A_V\left(\frac{\lambda_V}{\lambda}\right)^\beta$ where β is set at 1.7. From A_λ we find $\tau_\lambda = \tau$.

We define $\eta = 0.06$. This value is empirically found in regions where the field is expected to be well ordered and the grains well aligned Serkowski et al. (1975).

$I_{0,star}$ is found by assuming a constant background radiation intensity at the observation wavelength from Red Giant Star-like blackbodies at the back of the integration volume, or in the case of the map of the galaxy mentioned in §2.1.3 from Red Giant Star-like blackbodies distributed throughout the volume. For the maps of superbubbles produced in Chapters 3, 4 and 5 $I_{0,star}$ is non-zero only for locations in the integration volume behind the object of interest. This is like observing light from a wall of stars behind whatever polarizing source we are interested in studying.

The above method assumes that we are in the optically thin limit. This is because our analysis includes nothing about scattering of light into our integration path. As the opacity rises and more light is extinguished from our line of sight, it also means that the chances increase for light from outside our integration path to contribute to the observed intensity. As the opacity grows our synthetic images for this type of polarization become less reliable.

Emission

To solve for the integrated emission we solve the following equations for each integration step, n :

$$I_n = \eta_{n,dust}\delta l \tag{2.11}$$

$$I_{n,P} = \epsilon I_n sin^2(\phi_n) \tag{2.12}$$

where $\eta_{n,dust}$ is the local dust volume emissivity and ϕ_n is the angle between the line of sight and $\vec{B}$ at the step i. We assume a uniform polarizing efficiency, ϵ, of 10% Ponthieu et al. (2005).

We numerically integrate though each step n along all lines of sight. The total I,Ip,Q

and U for each line of sight:

$$Q = \sum_n I_n cos(2\theta_n) \tag{2.13}$$

$$U = \sum_n I_n sin(2\theta_n) \tag{2.14}$$

$$I = \sum_n I_n \tag{2.15}$$

$$I_P = \sum_n I_{n,P} \tag{2.16}$$

Where θ_n is the angle between the vertical line on the plane of the sky and the projected component of the magnetic field on the sky in the n^{th} integration step. Extinction has been ignored because of the very small opacity in the sub millimeter range.

To find the dust volume emissivity we assume grains with a radius of a tenth of a micron and with temperatures of $30K$ and model the grains as blackbodies. Since we know the number density of the dust, we can find the total emissivity of a volume by multiplying the number of emitters in that volume by the emissivity of a single grain.

2.1.3 Foreground and Background Modeling

We also create synthetic images that include integration through foreground and background. [4] To create these components, we place the superbubble density and magnetic field information at a location in a simple model galaxy and then integrate from the edge of the galaxy, defined at 10 kpc from galactic center, [5] through the bubble location to our own location in the galaxy defined at 8.5 kpc from galactic center Kerr & Lynden-Bell (1986). The model of the galaxy through which we numerically integrate assumes a dust distribution that follows the Dickey & Lockman (1990) gas profile with an additional parameter that includes the scale length of the gas from galactic center.

[4] We model only the diffuse ISM, ignoring cold dark clouds.

[5] Only dust emission is integrated from the edge of the galaxy. For starlight polarized by dust, we start the integration at a 'wall of stars' at just beyond the distance our superbubble is located at.

This modification of the density distribution is done like so:

$$\rho(r, z) = e^{-\frac{r}{h_r}} \rho(z) \tag{2.17}$$

where $\rho(z)$ is the DL density distribution (see §2.2.2) and h_r is the radial scale length of the gas in the Milky Way. The value for h_r is assumed to be $2.26kpc$.

The galactic magnetic field is modeled as a toroidal field with no change in magnitude. This is done for simplicity; field strength does not affect dust emission or the polarization of transmitted starlight. We are only concerned with the orientation of the magnetic field.

Polarization maps of our simple model galaxy in dust emission and transmitted starlight can be found in Figures 2.2.4 and 2.2.4 respectively. For Figure 2.2.4 we distribute stars uniformly throughout the galaxy instead of creating a wall of stars. With both of these maps we can see the effects of projection on the observed polarization. When looking towards regions of the galaxy where our (central) line of sight is parallel to the magnetic field, the polarization should decrease dramatically. Surrounding this location, we see the magnetic field projected onto the plane of the sky to produce polarization that would appear as if the magnetic field is curved, when really we are just seeing the effects of projection!

2.2 Numerical Modeling of Superbubble Evolution

In this thesis we discuss simulations of a superbubble expanding into spiral type galactic disc. For every simulation the galactic mid-plane is in the $\hat{x}$-$\hat{y}$ plane of the simulation. A magnetic field oriented in the $\hat{x}$-direction is also included for every simulation. This magnetic field varies with height above the plane to maintain a constant β, but is uniform in the $\hat{x}$-$\hat{y}$ plane for any given $\hat{z}$.

2.2.1 WOMBAT

The simulations were created using an updated version of the TVD 3D ideal MHD code discussed in Ryu & Jones (1995) and Ryu et al. (1995). This code explicitly enforces the divergence free condition of the magnetic field with a constrain transport method

discussed Ryu et al. (1998). This code has been updated by Pete Mendygral to focus on optimizing parallel operations on multiple computer cores at once, making large simulations more computationally practical. The equations of ideal MHD, written below, are solved on an Eularian grid that has been divided into sub-grids amongst computer cores. Sub-grid work can be accelerated by Open MP. Boundary information for these sub grids is then passed between cores using MPI communications Mendygral (2011). Where radiative cooling is used, we followed the exact integration scheme proposed by Townsend (2009)

$$\frac{\partial \rho}{\partial t} + \vec{\nabla} \cdot (\rho \vec{v}) = 0 \tag{2.18}$$

$$\frac{\partial \vec{v}}{\partial t} + \vec{v} \cdot \vec{\nabla} \vec{v} + \frac{1}{\rho} \vec{\nabla} P - \frac{1}{\rho} (\vec{\nabla} \times \vec{B}) \times \vec{B} = 0 \tag{2.19}$$

$$\frac{\partial P}{\partial t} + \vec{v} \cdot \vec{\nabla} P + \gamma P \vec{\nabla} \cdot \vec{v} = 0 \tag{2.20}$$

$$\frac{\partial \vec{B}}{\partial t} - \vec{\nabla} \times (\vec{v} \times \vec{B}) = 0 \tag{2.21}$$

$$\vec{\nabla} \cdot \vec{B} = 0 \tag{2.22}$$

Where the units of $\vec{B}$ are chosen so that the factor of 4π does not appear in the equations.

2.2.2 Atmosphere Initialization

The simulated ambient medium models the atomic component of a simple and quiescent ISM with a hydrostatic atmosphere centered in $\hat{z}$. The number density of the atomic gas in the mid-plane is set at $1cm^{-3}$. The pressure at the mid-plane is derived using this number density and a temperature of 10^4 K assuming an adiabatic index of $\gamma = \frac{5}{3}$. To maintain hydrostatic equilibrium, it is necessary to set the vertical profile of two out of the three following parameters: pressure, density and gravity, and then solve for the third. We set the density according to the vertical distribution described by Dickey &

Lockman (1990) (hereafter DL90).

$$\rho(z) = \frac{\rho_0}{0.566}\left(0.395e^{-\frac{1}{2}(\frac{z}{90})^2} + 0.107e^{-\frac{1}{2}(\frac{z}{225})^2} + 0.064e^{-\frac{z}{403}}\right) \tag{2.23}$$

Since using a constant gravity with the DL90 density profile produces an unrealistically high temperature at large z, we use instead a gravity with an exponential dependence on $\hat{z}$:

$$\vec{g} = -G\Sigma_0(1 - e^{-\frac{z}{h_{stars}}})\hat{z}. \tag{2.24}$$

Where $\Sigma_0 = 48 M_\odot pc^{-2}$ Veltz et al. (2008) and h_{stars} is an intermediate value for the scale height of the stars. Pressure is solved for numerically. This arrangement produces a realistic profile for the gravity with height, and keeps the temperature reasonable within the physical extent of the grid. The atmosphere produced from this method is static to within less than four orders of magnitude of the sound speed in mid-plane of the atmosphere for the timescale of the simulations. This implies that numerical error in maintaining a hydrostatic atmosphere do not contribute significantly to the motion of the gas.

2.2.3 Magnetic Field Configuration

All simulations included the regular component of the ISM magnetic field, oriented in the simulation along the $\hat{x}$-direction. The pressure created by this magnetic field is accounted for by splitting the numerically solved pressure required for hydrostatic equilibrium into a gas pressure and a magnetic field pressure. Because this total pressure decreases with height above the plane, so too must the magnitude of the magnetic field or else the ratio of gas pressure to magnetic field pressure, β, would grow very small and leave the simulation susceptible to Parker's Instability. For simplicity β is kept constant with height above the galactic mid-plane (large $\mid z \mid$), and therefore the magnitude of the magnetic field decreases with height. Gas pressure and the magnitude of the magnetic field are defined from the total pressure as follows:

$$P_{gas} = \frac{P_{tot}}{1 + \frac{1}{\beta}} \tag{2.25}$$

$$B = \sqrt{8\pi \frac{P_{tot}}{\beta + 1}}. \tag{2.26}$$

2.2.4 Energy and Mass Injection

Energy deposited from the superbubble into the ISM is modeled as a kinetic 'wind' in order to reproduce most of the elements of a wind blown bubble described by Weaver et al. (1977). Modeling sequential discrete supernova burst as a continuous wind is a reasonable approximation since supernova expanding into the hot interior of a superbubble become subsonic before reaching the bubble shell dissipating the energy of the burst as thermal energy into the superbubble interior Mac Low & McCray (1988).

Weaver et al. (1977) outlines the structure of a wind blown bubble. The 'fast wind' solution, explored more explicitly in Koo & McKee (1992), requires that the wind velocity is large enough to keep the wind density low enough so that cooling in the wind and in the wind shock is irrelevant. It a widely used model for understanding superbubble evolution in a quiescent medium (eg.Heckman et al. (1990) Mac Low & McCray (1988) Stil et al. (2009)). The structure of a superbubble in this model has four parts, a) wind, b) shocked wind, c) shocked ISM and d) the ambient ISM. Though the wind shock is adiabatic because of low densities and large temperatures, the forward shock quickly becomes an isothermal shock as the high density of the shocked ISM means that the cooling rate in region c) becomes very rapid. The result is a superbubble with a hot, adiabatic interior surrounded by a very thin, dense shell of ISM material. Additionally, there is a conduction zone between the cool shell and the hot interior. The rate of mass loss from the shell into the bubble interior can cool the bubble interior and slow the expansion rate Weaver et al. (1977).

Energy from multiple supernova events is approximated as a constant luminosity equivalent to the the number of SN going off in a given time. The luminosity is then:

$$L = \frac{NE_{SN}}{\tau}. \tag{2.27}$$

where N is the number of type II supernova events, $E_{SN,avg}$ is the average energy released per supernova event and τ is the timescale for energy injection (10^7 years). The luminosity this produces has been used by many previous authors (e.g. Stil et al.

(2009), Mac Low & McCray (1988), Ferriere et al. (1991),Mac Low et al. (1989)).

Mass is injected into a region twenty voxels in radius. Numerical shocks are generally several voxels thick, and the driving region requires a radius exceeding the numerical shock thickness in order to produce a smooth, symmetric outflow. Twenty voxels was established as the minimum practical radius so that the outflow had little to no lasting artifacts from the injection method.

The mass is injected with a radial velocity whose magnitude is equal to the wind speed times a spacial ramping function. The ramp is:

$$J(r) = TANH\left(3\left(\frac{3r}{r_0}\right)^3\right). \tag{2.28}$$

Where r_0 is the radius of the driving region. This function gives a slow enough increase in the velocity to avoid creating regions of too low pressure near the center of the driving region where the flow is strongly divergent. It also gives a value close to one when $r = r_0$.

The luminosity is initially determined by kinetic energy loss only, however, the injected mass comes with some thermal energy. So where we would wish to describe the luminosity as $L = 0.5\dot{m}v^2$ (where $\dot{m}$ is the mass loss rate) in reality, the luminosity is given by:

$$L = 0.5\dot{m}v^2\left(1 + \frac{2\gamma}{(\gamma-1)M^2}\right) \tag{2.29}$$

Where $\dot{m}$ is the mass loss rate ($\dot{m} = 4\pi r^2\rho(r)v(r)$) and M is the Mach number of the wind defined from internal parameters. The fraction of power injected as kinetic power is the kinetic power divided by the total luminosity, which is given by:

$$F_{KE} = \left(1 + \frac{2\gamma}{(\gamma-1)M^2}\right)^{-1} \tag{2.30}$$

We set the Mach by setting the fraction of kinetic power to 0.9. (This would leave an error of about 10% in the superbubble luminosity, except that we scale the kinetic luminosity to be 90% of the total luminosity by decreasing the mass loss rate.) Larger fractions face numerical difficulties in establishing forward and reverse shocks.

Another method of energy injection was also explored. Following Mac Low & McCray (1988) we injected the energy as mass with high thermal energy into a region with a 5 voxel radius. Injection of the energy as pressure was found to produce the two shock structure of the Weaver et al. (1977) model with a few caveats, discussed further below. Even with the two shock structure present, there are differences in the structure of the SB. Most obviously, since energy was not added to the simulation as mostly kinetic energy, but rather as thermal energy, the unshocked 'wind' region was not cold but instead very hot. In this case, the 'wind' region could be susceptible to cooling. Should the 'wind' cool before being shocked the simulation would no longer be able to produce the Weaver model. Care must be taken to insure that the 'wind' is not so dense as to increase the cooling rate enough that cooling is important in freely expanding wind if it is important to reproduce the Weaver model.

The other notable difference between the Weaver et al. (1977) model and our pressure injected simulations was the change in temperature and velocity of the wind with radial distance. As seen in Fig. 3 of Weaver et al. (1977) the temperature is expected to be roughly constant in the wind. Also assuming a constant velocity and using mass conservation means that the density should drop off as $r^{-}2$, which would require the pressure to also drop off as r^{-2} as well. In the Weaver et al. (1977) model the energy flux from the wind is assumed to be almost all kinetic so pressure is a negligible contribution to the energy density. The very small magnitude of the pressure means the pressure gradient is a weak force and the velocity should grow slowly enough with radius as to be assumed constant. However, by injecting the energy as thermal energy, the pressure in the wind is much larger, and it can no longer be assumed that the pressure gradient will change the velocity in the wind by a negligible amount. (In fact, we are relying on the pressure gradient to drive material out and create a kinetic component to energy flux from the wind.)

A full analysis of energy injection methods is not possible here so we kept with the kinetic energy injection that more closely matched the often cited Weaver et al. (1977) model. Should future work investigate this aspect of superbubble modeling (which is likely since superbubbles are increasingly constructs created organically within turbulent structure simulations) the simulations produced here can provide a point of comparison.

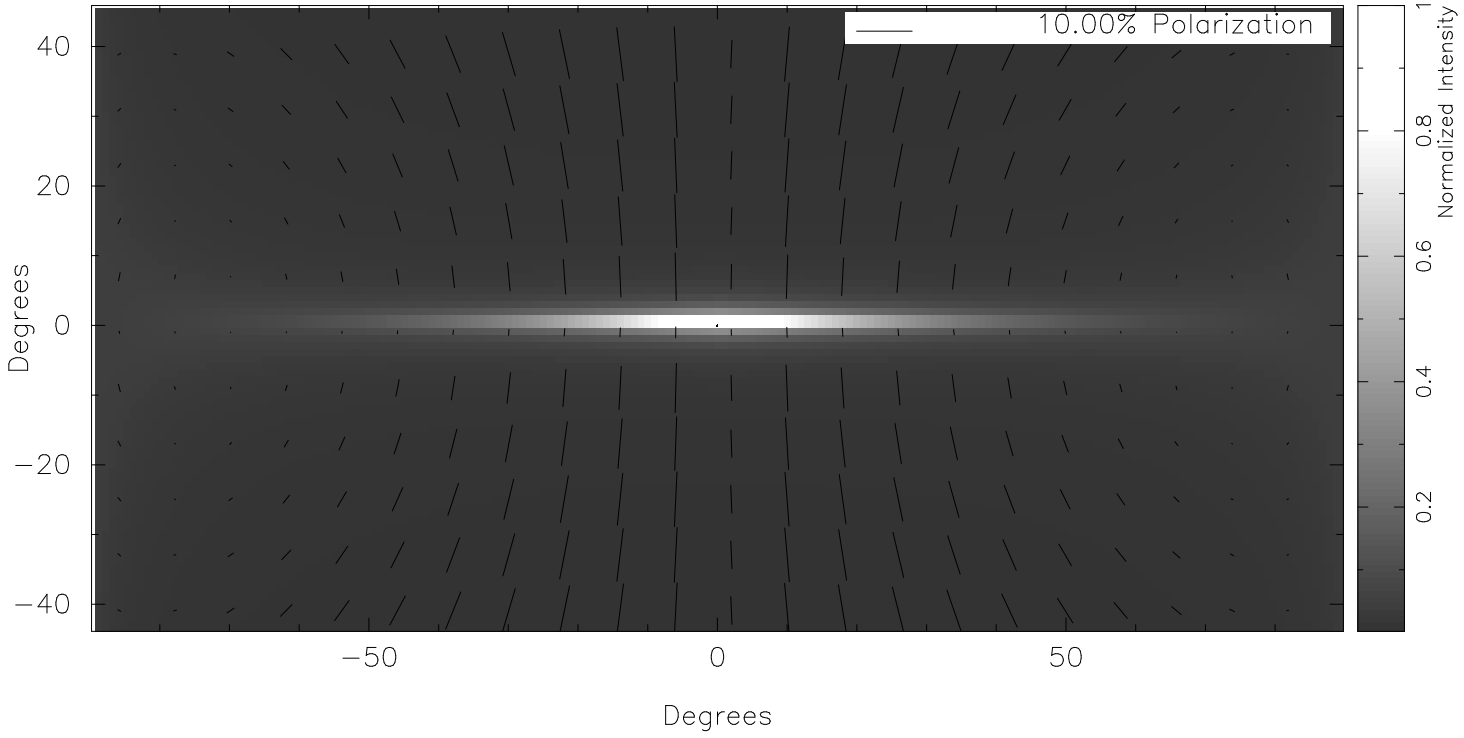

Figure 2.1 Polarization map of dust emission at 100 microns looking toward galactic center with a resolution of approximately 1 deg.

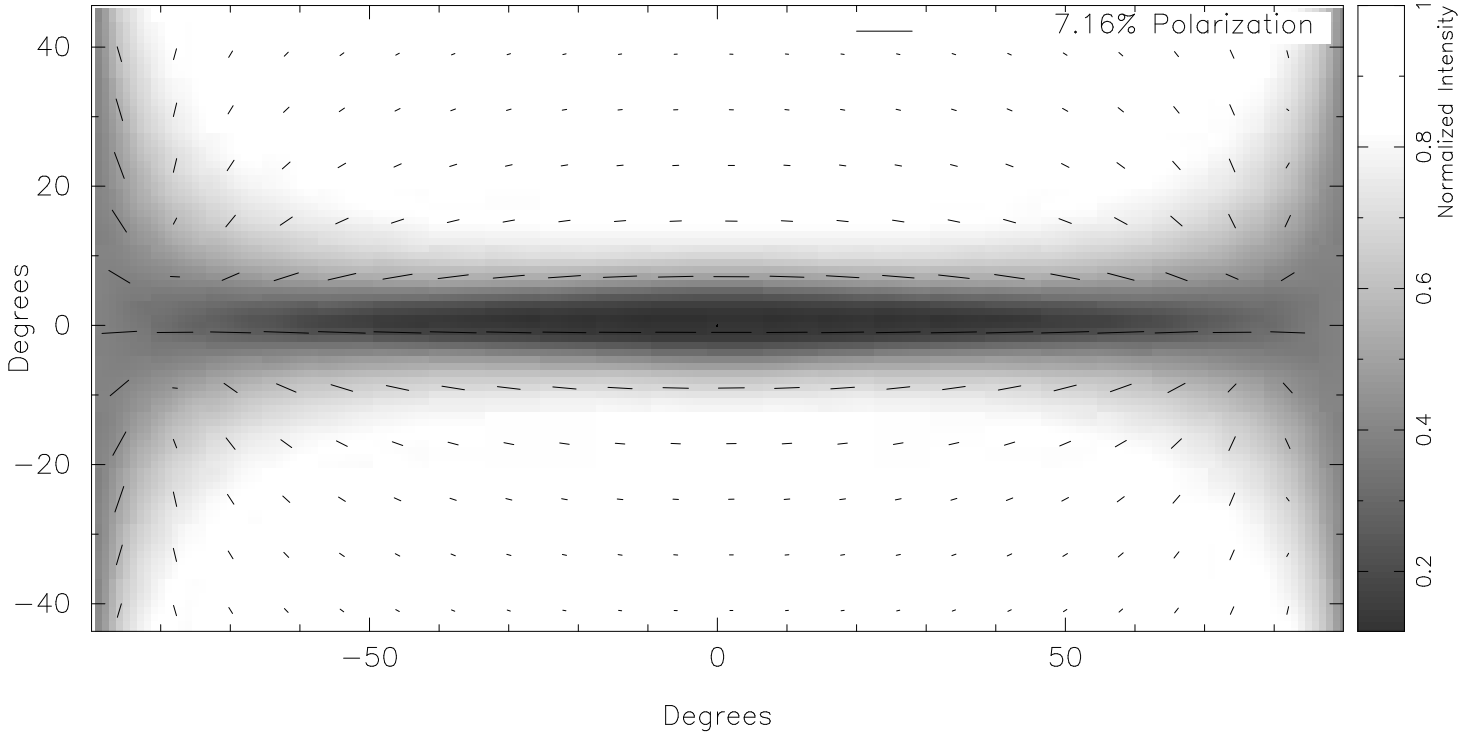

Figure 2.2 Polarization map of transmitted starlight at 2.2 microns looking toward galactic center with a resolution of approximately 1 deg.

Chapter 3

Superbubbles Before Breakthrough

3.1 Introduction

We consider the effect of a superbubble on the density of dust and the orientation of the field in a Milky-Way analog to understand the change in polarization the superbubble would produce. In this chapter we limit ourselves to a superbubble that remains much smaller than the effective scale height of the disk. [1] The problem of a breakthrough superbubble is explored in Chapter 4. As the superbubble expands it will create a region that has a density lower than the ambient medium, assuming a low enough mass loss rate from the supernova creating the superbubble. The material displaced from the evacuated region will create a shell surrounding it that has a density higher than the ambient medium. The magnetic field will be transported by this expansion as well. As the superbubble expands, regions of low density will also be largely devoid of magnetic field energy assuming a small enough added magnetic energy density from the supernovas. The high density shell will see a compressional increase in field magnitude. The shock will produce and strengthen components of the magnetic field orthogonal to the original field orientation by increasing the magnitude of the field components tangential to the shock normal. Should these post-shock field components that

[1] For the Dickey & Lockman (1990) atmosphere this is about 350 pc.

are differentially orientated from the background field be coincident with large enough variations in dust density, it is possible that they would produce an effect on near-IR and sub-millimeter polarization measurements. The purpose of this chapter will be to determine semi-analytically the plausibility of this hypothesis. §3.2 will overview the theoretical development of an adiabatic wind-driven superbubble. Using this description §3.3 will investigate the effect of a spherical superbubble on polarization measurements.

3.2 Analytical Spherical Superbubble Development

We explore very idealized and simple models of superbubble evolution. For early development, before the superbubble would reach roughly a scale height in size, the stratification of the environment external to the superbubble is ignorable, though the orientation of the magnetic field is not. For this model it is possible to use the analysis of Castor et al. (1975a), Weaver et al. (1977) and Ferriere et al. (1991).

For all subsequent discussions, superbubble will refer to the entirety of the material and magnetic field affected by the collective action of multiple supernova. Shell will refer to the region between the forward shock and the contact discontinuity. Cavity will to the region behind the contact discontinuity to the central region of the superbubble.

Following Weaver et al. (1977) the radius of a wind-blown bubble can be found from the similarity relation:

$$r(t) = \alpha(\frac{L}{\rho_0})^{1/5}t^{3/5} \tag{3.1}$$

assuming radiative losses in the shocked wind region are negligible. Here $\alpha = 0.88$ for a weakly cooled forward shock and $\alpha = 0.76$ for a strongly cooled shock.

The thickness of the shell can be found by assuming all of the mass swept up from the interior of the bubble remains in the shell. This requires knowing the density of the shell, which is dependent on the compression ratio. For a thin shell, to first order the shell thickness is:

$$\Delta r(t) = \frac{r(t)}{3}\frac{\rho_0}{\rho_{shell}}. \tag{3.2}$$

From this we can see that for large compression ratios the shell thickness decreases.

For a strong adiabatic shock with a maximal compression ratio of four, the shell will be a 12^{th} the radius of the bubble. However, for a strongly cooled shell, the forward shock can be considered an isothermal one, in which case the compression ratio goes as the square of the Mach number. This can create very thin, very dense shells. To find the Mach number, we need to know the velocity of the forward shock, which is the time derivative of the bubble radius.

$$v(t) = \beta(\frac{L}{\rho_0})^{1/5} t^{-2/5} \tag{3.3}$$

Where $\beta = 0.6\alpha$. This and the ambient sound speed give the Mach number $M = \frac{v(t)}{c_s}$, which defines a compression ratio of:

$$\frac{\rho_{shell}}{\rho_0} = \frac{\gamma + 1}{(\gamma - 1) + \frac{2}{M^2}}. \tag{3.4}$$

For an isothermal shock, the compression ratio is simpler:

$$\frac{\rho_{shell}}{\rho_0} = M^2. \tag{3.5}$$

We assume the shell is strongly cooled if the cooling length is smaller than the width of the shell. Where the cooling length is approximated by:

$$l_{cool} \simeq v(t) \frac{kT}{n_e \Lambda(T)} \leq \Delta r(t). \tag{3.6}$$

For very early times in the superbubble's lifetime the shell thickness will be very thin, the expansion velocity very fast and the temperature very high. Early in its evolution the bubble shell will not be strongly cooled since the temperature will be too high for efficient cooling. As the bubble ages the shell will thicken, the expansion slow and the temperature drop. The temperature at which cooling becomes very efficient is dependent on the cooling curve. Using the curve of Dalgarno & McCray (1972) radiative cooling becomes very efficient for temperatures between 10^4 K and 10^6 K. Using a crude version of this cooling curve we find the approximate cooling length. Looking to figure 3.3 we see that the shell is strongly cooled for superbubble ages greater than about $36,000$ years for a luminosity of 10^{37} $ergss^{-1}$ and about $120,000$ years for a luminosity of 10^{39} $ergs$. This is longer than the age expected by Mac Low & McCray (1988) who

use the cooling curve given by Gaetz & Salpeter (1983).

This difference likely exists because of the difference in how to define when to expect the shell to become cooled. The definition used by Mac Low & McCray (1988), who use the argument as it was made by Castor et al. (1975a), is that the shell can be considered strongly cooled when the age of system is larger than the cooling time ($l_{cool}/v(t)$). However, not all the gas heated by the shock will have been in the system this long. In order to assume that the gas in the shell is strongly cooled, the gas must have the time to cool before significant amounts of shock heated gas are added to the shell. Once the shell thickness is larger than the cooling length, we can assume that the gas in the shell can cool strongly and that the shell thickness will decrease. This ignores the non-linear nature of cooling, since the cooling rate is dependent on density and cooling increases the density.

So far we have only considered the pressure support provided by the thermal motion of the gas in determining shell thickness. Should β be small enough such that the magnetic field provides a notable portion of the pressure support in the shell, then the shell thickness would not be determined by the compression ratio of the gas in the shell. This means even for a shell with the conditions necessary for rapid cooling the shell might not collapse and increase shell density as in an isothermal shock. From Ferriere et al. (1991) we see that from the conservation of field flux, the shell thickness for a magnetically supported shell would approximately be:

$$\Delta r(t) = \frac{B_0 R_s sin\theta}{2B_s}. \tag{3.7}$$

Where θ is defined from the ambient magnetic field line direction. To find the magnetically supported shell thickness we need to know both θ and the ratio of the shell field magnitude to the ambient field magnitude. Using equation 3.7 to find the shell thickness runs into the dilemma that a larger shell thickness would also mean a smaller compression ratio, but how to reconcile this with the compression ratio found from the jump shock conditions? To find the shell thickness for the most general case in which both thermal and magnetic pressure support for the shell are accounted for we set the ram pressure equal to the total pressure. This is the same as assuming the thermal and magnetic pressures in the ambient medium are negligible, as is the kinetic

energy in the shell.

$$\rho_0 v(t)^2 = \frac{B_{shell}^2}{8\pi} + P_{shell} \tag{3.8}$$

Substituting equations 3.2 and 3.7 we find a modified version of equation 43 in Ferriere et al. (1991) which gives the shell thickness as:

$$\Delta r(t) = \frac{R_s}{2}\left(\frac{T_s}{3T_0\gamma M^2} + \sqrt{\left(\frac{T_s}{3T_0\gamma M^2}\right)^2 + \frac{sin^2\theta}{\beta\gamma M^2}}\right). \tag{3.9}$$

Here β and the Mach number are defined from ISM properties. For a large β or small angle θ this reduces to a shell thickness determined only by thermal pressure. However, even for small β if the shock is strongly cooled enough to be considered an isothermal shock, then the shell temperature would equal the ambient temperature and the shell thickness is determined by the field pressure.

The field from the interior of the superbubble will be swept up into the shell due to the frozen-in condition. The strength and orientation this field can be found following Ferriere et al. (1991). There they show that using the MHD jump-shock conditions and the divergence-free condition the field components in the shell are (assuming no velocity in the ambient medium):

$$B_{1n} = B_{0n} \tag{3.10}$$

$$B_{1t} = B_{0t}\left(\frac{1 - \frac{B_{0n}^2}{4\pi\rho_0 v_s^2}}{\frac{\rho_0}{\rho_1} - \frac{B_{0n}^2}{4\pi\rho_0 v_s^2}}\right). \tag{3.11}$$

Should the ram pressure be much larger than the normal component of the ambient magnetic energy density, $\rho_0 v_{SN}^2 \gg \frac{B_{0n}^2}{8\pi}$ then the tangential component of the magnetic field in the shell will increase over the ambient field by the compression ratio of the gas, $\frac{\rho_1}{\rho_0}$.

Since compression increases the field strength by increasing the magnitude of components tangential to the shock, the magnetic field will have an increasing contribution to the pressure of the shell for large θ. This is thoroughly examined by Ferriere et al.

(1991), who find that with strong cooling the shell should have dimples where the shell's shock normal lies parallel to the ambient field orientation. These dimples are created by the shell being supported by thermal pressure only and therefore susceptible to collapse when radiative cooling becomes efficient. Locations in the shell away from these two points have greater contributions to the shell pressure from the field. The maximal contribution of the magnetic field is found in a ring lying in a plane normal to the ambient field orientation. This ring sees the maximal compression of the magnetic field since it is in this plane that the shock normal is perpendicular to the ambient field orientation. However, this increase in field strength in the ring does not affect our polarization observations since the tangential component in the ring lies parallel to the plane.

It may appear then that there are three possible shells. One for a thermally supported gas without efficient cooling, a thin shell from a large beta gas with efficient cooling and finally a shell supported through magnetic pressure for select locations in the shell and thermally supported elsewhere. The largest shell densities are possible in a shell with the large beta and efficient cooling. Is this shell possible with typical ISM conditions?

For the magnetic field to be negligible in terms of pressure support, its energy density must be small compared to the thermal energy density in the shell. As the shell cools the magnetic energy density becomes a larger portion of the total pressure support in the shell, particularly since the larger compression ratio for the isothermal shock means a larger compression ratio for the field.

If the ambient medium has a large β then the shell is thermally supported, at least until the cooling becomes efficient. It is then left to determine if when cooling becomes efficient the shell will have a small enough β that at least part of it will be magnetically supported.

We choose an environment with a higher than typical β for the ISM to see how plausible a strongly cooled, thermally supported shell is. The ISM environment we consider has a field strength of $1\mu Gauss$, number density of $1cm^{-3}$ and temperature of 10^4K we find $\beta \simeq 35$.

For a superbubble with a luminosity of $L \sim 3x10^{39}ergss^{-1}$, we expect the superbubble to cool the shell effectively at about 120,000 years. Using the ISM parameters defined earlier we find the Mach number to be ~ 13. Plugging in the appropriate values

we find the ratio of shell thickness to superbubble radius for an isothermal shock to be $\sim 1.8x10^{-2}$ at $\theta = 0$. For the shell ring where we expect the maximal magnetic pressure support we find the ratio of shell thickness to superbubble radius for an isothermal shock to be $\sim 2x10^{-2}$. Obviously, the magnetic field is providing some of the pressure support in the shell or there would not be such a difference in shell thickness with θ with our large β ISM. Though we should not expect to find a strongly cooled, fully thermally supported shell in the ISM, it is not unreasonable to expect a shell supported largely by thermal pressure. This differs from the result found by Ferriere et al. (1991), again largely due to the differences in how a strongly cooled shell is defined. If we considered the shell strongly cooled when they do, we find much the same results.

This brings up the point that different definitions of strong cooling can produce very different evolutions. First there are different cooling curves, with differing regions of temperatures for maximal radiation losses. It is assumed, using the curve produced by Dalgarno & McCray (1972) that the rate of energy loss is greatest for gas temperatures between 10^4K and 10^6K, though this is slightly different from Mac Low & McCray (1988) who have a somewhat higher cooling rate for temperatures larger than 10^6K. The temperature of the shell must be in this range for efficient cooling, but depending on the luminosity and how one defines efficient cooling, the shell may not be efficient at cooling as soon as the shell temperature enters this range. For a low luminosity superbubble ($L = 3.16x10$), the age of the superbubble is not larger than the cooling time until well after the superbubble shell has adiabatically cooled past 10^6K and is actually about $3.5x10^5K$. However, the cooling time at this point is still larger than the crossing time for the shell. This measure for efficient cooling will not be met until almost 16,000 years later in the superbubble lifetime than the age of the superbubble vs cooling time condition.

When using a onset for strong cooling temperature, the starting time for strong cooling can be overestimated when one assumes the temperature of the bubble can be determined from adiabatic cooling. Though the superbubble shell is not strongly cooled, it is still cooled to some degree and the temperature found from adiabatic expansion cooling will be larger than the actual shell temperature that the shell would have if allowed to cool from the start of the superbubble's evolution. The choice of what temperature signals the start of strong cooling is therefore important, but somewhat

arbitrary in that any one choice would not reflect the full physical picture. For our simulations instead of focusing on the onset of strong cooling temperature, we instead only ensure that strong cooling is underway well in advance of the time frames of the simulation that we will care about. This is discussed more in Chapter 5, the chapter on numerical modeling.

A shell supported by a combination of thermal and magnetic pressure should have a point of transition between thermal pressure dominance to magnetic support dominance. We are interested in where this change occurs since we expect to get maximal vertical field components at 45 deg from the plane from compression with a uniform shell thickness and ambient density. With a stratified atmosphere we expect the location of maximal polarization to occur at a smaller angle since the density of dust is decreasing with distance from the plane. With a changing shell thickness (from the change in pressure support) the problem becomes even more complex. A modified version of equation 49 in Ferriere et al. (1991) gives the angle at which thermal and magnetic pressures balance as:

$$\theta_{balance} = sin^{-1}\left(\frac{2}{3M}\frac{T_s}{T_0}\sqrt{\frac{22\beta}{\gamma}}\right). \tag{3.12}$$

Looking at this it is clear that $\theta_{balance}$ grows larger for larger β and/or smaller Mach number. This is due to the smaller influence of the magnetic field in each case. Looking at Figure 3.3 we can that $\theta_{balance}$ grows with lower luminosity and with superbubble age. A shell that is predominately thermally supported should be thinner than one predominately supported by the magnetic field, so superbubbles with larger $\theta_{balance}$ have an increased chance for a thin shell at the location of maximal polarization. However, such superbubbles, having a lower luminosity and greater age, would also have a smaller compression ratio. Without further investigation it is unclear how great the change in polarization could be. [2]

Given an initial field and ambient density we can find the field in the shell if we know the shock velocity. Additionally, knowing the shock velocity and ambient pressure and density will give us the shell density. With the field orientation and density known in

[2] We note that the $\theta_{balance}$ that we find here are much larger than those found by Ferriere et al. (1991) since they assumed the shell temperature would cool to $100K$ about 100 times smaller than the temperature of the shell we assume.

the shell, we can find the expected change in polarization for light that is emitted from or transverses the shell.

In addition to determining the shell properties, we also explore the properties of the interior of the superbubble relevant to our polarization observations. The evacuation of the interior of the superbubble depends on the net result between the rate of input of material and magnetic field from contributing supernovae and the rate of expansion of the superbubble contact discontinuity. The location of the contact discontinuity will depend on the location of the forward shock and the thickness of the shell, which as already discussed depends on the properties of the shell and ISM.

The material in the hot interior of the bubble will be only the mass lost by the contributing stellar winds and supernova inside the superbubble, assuming no conduction from the cool shell wall. However, it is likely that this assumption is violated and that the mass loss from the shell into the interior of the bubble dominates the mass Weaver et al. (1977), Mac Low et al. (1989). However, this contribution can simply be included into a single mass loss term $\dot{m}$ which distributed over the interior of the bubble should mean a density of:

$$\rho_{bubble} = \frac{3\dot{m}t}{4\pi r^3(t)}. \tag{3.13}$$

The mass loss term must provide enough mass to replace the material pushed out by the expansion for the superbubble to produce a cavity in the atomic gas. Ignoring the thickness of the shell, the mass evacuated from the interior of the bubble would be:

$$m = \frac{4\pi\rho_0 r(t)^3}{3}. \tag{3.14}$$

Where ρ_0 is the ambient mass density. For a superbubble $100pc$ in radius and an ambient density of $1gcm^{-3}$, the mass evacuated would be nearly $10,000M_\odot$, requiring a mass loss of more than $3,000M_\odot$ every million years for a superbubble luminosity of $3x10^{37}ergss^{-1}$. Since this would effectively require each supernova in the superbubble to produce $3,000M_\odot$ each, it is very likely that the superbubble wil create a cavity. For a luminosity 100 times higher than this, the mass required is larger than $10,000M_\odot$ every million years and would necessitate more than $100M_\odot$ from every supernova event. For ambient densities larger than $1gcm^{-3}$, it becomes more difficult to produce superbubbles

that would not create a cavity in density. Though regions of very high density are also smaller in extent, making the mass needed for larger bubbles smaller than if the high ambient density surrounding a young bubble was present during the entire development of the superbubble. Lower ambient densities make it more possible that a cavity in density would not exist, though it also means lower star formation rates and therefore lower chances for coincident supernova events. It should be noted that the effect of ambient density is not linear but goes as $n^{\frac{2}{5}}$ since the density will affect the size of the superbubble radius as well.

Since the magnitude of the magnetic field is irrelevant to the synthetic observations considered in this work we do not need to know if the magnetic field added is strong enough to replace the ambient magnetic energy density. In fact, we do not even need to determine the orientation of the interior field as long as the interior density is much lower than the ambient density since it is only the density of the dust grains that controls the magnitude of either polarized dust emission or the polarization of transmitted starlight. As we have shown that the superbubble should create a cavity in density, we can reasonably ignore the effect of added magnetic field.

3.3 Analytical Spherical Superbubble Effect on Polarization

Before we begin numerical work, we first would like to discern the plausibility of detecting the effects of superbubbles in polarization observations. To do this we create simple analytical models of a superbubble and then use these to create polarization maps.

As stated earlier, we first consider early periods of the superbubble's development before the superbubble 'feels' the pressure and density gradient of the galactic atmosphere. During this period the superbubble should remain spherical for a high-β system. Though the total ambient pressure (thermal and magnetic) in the ambient medium is increased, propagation speed in the direction perpendicular to the magnetic field is actually greater than in the direction of the field. The consequence of this is that in a magnetized medium, the superbubble would be larger in the plane perpendicular to magnetic field lines. For our first analysis we ignore this feedback of the magnetic field on superbubble shape, and consider only a spherical shell with magnetic field strength

increases due to compression, this is equivalent to considering the case where the ram pressure of the shock is much larger than the magnetic energy density of the ISM.

In this very simple scenario we first investigate a single $2D$ quarter arc section of the spherical shell, with the arc starting from a direction parallel to the field and going to a direction perpendicular to the field in a plane perpendicular to the line of sight (for a line of sight that is perpendicular to the magnetic field). This quarter arc could be rotated about the axis parallel to the magnetic field and mirrored across the plane perpendicular to the field to get a complete shell. However, we will first try something even simpler, using the density and magnetic field in this $2D$ quarter arc for each entire path length through the shell. This will overestimate the line of sight contribution of the polarization components perpendicular to the plane of the galaxy. If this overly optimistic set-up doesn't make the effects of a superbubble on polarization detectable, then more complex models are not likely to do so.

Without feedback from field tension, the magnitude of the shock velocity will remain uniform along this arc. The density in the shell will also remain uniform assuming no mass transport perpendicular to the shell. The density in the shell can be found by equation 3.4 for an adiabatic shock and 3.5 for a shell cooled rapidly enough to be an isothermal shock assuming no perpendicular mass transport in the shell. Using the ratio of the shell density to the ambient density, we can easily find the magnitude of the components of the magnetic field in the directions normal and tangential to the shock front with equations 3.10 and 3.11. For this first analysis we ignore the effects of magnetic support. For our simple spherical superbubble the shock normal will be radial, therefore the normal component of the magnetic field will be the component of the field parallel to the radial direction. The tangential component will lie in the $2D$ plane of our quarter arc and be perpendicular to the radial component.

In $2D$ Cartesian coordinates, the magnetic field is set in the $\hat{x}$ direction as $\vec{B_0} = B_0\hat{x}$. The shock normal can be expressed as $\hat{n} = x/s\hat{x} + y/s\hat{y}$, where $s = \sqrt{x^2 + y^2}$. The component of the ambient magnetic field parallel to the shock normal is:

$$\vec{B_{0n}} = (\vec{B_0} \cdot \hat{n})\hat{n} \tag{3.15}$$

The component of the ambient field tangential to the shock surface is:

$$\vec{B_{0t}} = -(\hat{n} \times (\hat{n} \times \vec{B_0})) \tag{3.16}$$

As stated before the divergence-free condition of magnetic fields means that the component of the magnetic field normal to the shock is unchanged. In the limit of the ram pressure being much larger than the magnetic field energy density the post shock value of the tangential magnetic field component is simply the product of the compression ratio and the upwind components.

$$\vec{B_{1t}} = \frac{\rho 1}{\rho 0}\vec{B_{0t}} \tag{3.17}$$

For a rapidly cooling shock, such that it can be considered an isothermal shock, the compression ratio is simply the square of the Mach number. (See 3.5.) In this case, the tangential component of the magnetic field grows M^2, which leads to large amplifications for fast shock speeds. Depending on what location in the shell θ we consider, we could see a large increase in magnetic field directed orthogonal to the upwind field orientation ('vertical field'). As already discussed in the previous section we do not expect a strongly cooled superbubble without some pressure support from the magnetic field. However, it is prudent to first try the best case scenario to determine if more complex and realistic investigations are necessary.

Before using GE to create synthetic observations we create a very simple, 'best-case' argument for the detectability of superbubble shells in polarization. To do this we compare a line of sight that represents the longest path through the superbubble shell to a line of sight through the ambient medium (with an equivalent path length) to compare the change in polarization properties for a line of sight perpendicular to the magnetic field. The line of sight through the superbubble shell will traverse some foreground/background distance D with an ambient density of n_0, a distance through the shell of, $2\Delta x$ with density n_{shell} and through a distance $2(r-\Delta x)$ with density of n_0. The line of sight through the ambient medium will traverse a distance equal in length to the shell path, $D + 2r$ with density n_0. Where r is the radius of the superbubble, $\Delta x = \sqrt{\Delta r(2r - \Delta r)}$ and Δr is the shell thickness. In the ambient medium, the magnetic field is assumed to lie entirely in the $\hat{x1}$ direction. It is only in the shell that

the field deviates from this when the components of the magnetic field tangential to the shock are amplified through compression of the gas. For this simplified scenario we use the $2D$ post shock field components along the entire line of sight distance through the shell and ignore the field components that would be produced if we considered the shock in three dimensions. We also only consider parallel lines of sight. Depending on the angle θ, our line of sight will pass through a section of a shell that has some component of the field in the $\hat{x_2}$ direction, which would create regions of polarization orthogonal to the ambient polarization.

$$I = 2\Delta x n_{shell} + (2(r - \Delta x) + D)n_0 \tag{3.18}$$

$$Q = 2\Delta x n_{shell} cos(2\phi) + (2(r - \Delta x) + D)n_0 \tag{3.19}$$

$$U = 2\Delta x n_{shell} sin(2\phi) \tag{3.20}$$

Where $\phi = atan(\frac{\vec{B_{x_2}}}{\vec{B_{x_1}}})$. Using these equations we created 'maps' of the polarized "emission" in the shell. [3] These figures compare different lines of sight through the shell for three different luminosities, $3x10^{37}$, $3x10^{38}$ and $3x10^{39}$ at a simulated time of 10^6 and $5x10^6$ years. This is well before the bubble reaches a radius comparable to the effective scale height of the Dickey & Lockman (1990) HI galactic gas distribution for each luminosity. For the ambient medium there would only be horizontal polarization, any deviation from this is the result of the superbubble.

In figure 3.3 we compare the difference between a strongly cooled isothermal shock and an adiabatic one. It is clear that the increased compression ratio for the isothermal shock causes greater changes polarization than the adiabatic shock can produce, though the effect is lessened for older superbubbles. Looking at figure 3.4 we see that higher luminosities produce more change in the polarization than lower luminosities, and for longer times. This is likely due to the decreasing impact of the density on polarization

[3] Since both emission and transmission only rely on the number density of the dust and the orientation of the magnetic field along a line of sight, (assuming only background contributions to the unpolarized intensity) this analysis applies to both emission and polarized transmission. Though the orientation of the vectors would be rotated by half π for polarized transmission from the vectors for emission of polarized light from dust.

for lower luminosities as the compression ratio decreases. As the density becomes less important the change in orientation of the magnetic field becomes the dominate source of change in the polarization. We explore this more for the case that includes the effect of magnetic field on the shell thickness. Finally we explore the effect of foreground and background additions to the path. From figure 3.5 we see that adding this foreground and background greatly decreases the effect the superbubble has on the Stokes parameters.

From these figures it obvious that a superbubble produces polarization that can deviate largely from the ambient medium. Some important points to notice: younger and/or more luminous bubbles produce a greater effect, the cooled shell provides a much stronger effect than the adiabatic shell and adding any contribution from the ambient medium to the line of sight reduces the change in polarization. From this analysis we can suggest that large, luminous superbubbles that are placed in the galaxy such that there is little contribution from foreground or background with strongly cool shells should have a detectable polarization signature. However, we can not exclude the possibility that less luminous, more distant or even superbubbles without strong cooling could not produce a detectable signature. We must use a more sophisticated analysis to constrain these cases further.

We now wish to include the effects of magnetic pressure support. Using the compression ratio for either an isothermal or adiabatic shock, we can find the magnetic field in the shell just as before. However, since we expect an increase in the total field magnitude, pressure support from the field becomes increasingly important and the shell thickness should be determined by equation 3.9. For a large β or small θ this equation reduces to a shell thickness determined only by thermal pressure. We can use this to find the shell thickness for our $2D$ shell arc. We once again use the information from this arc for the entire path through the superbubble when determining the change to polarization. From the shell thickness we can find the density inside the shell using 3.2 and the magnetic field magnitude using 3.7 at each θ location.

We follow the same analysis as before, mapping the polarization in the shell, only now we define the shell thickness from equation 3.9. Figure 3.6 shows there is little change in the effect of a superbubble from a β of infinity to ~ 2. This is reassuring that for a range of β corresponding to expected ISM parameters, the polarization signature is

largely unchanged by the change in shell thickness from magnetic pressure. However, we have not included real three dimensional information which is important since the shell will change thickness along a line of sight when we include magnetic pressure support.

From these idealized and simple considerations, we can see that the basic components for increasing the observable polarization contribution along a line of sight are present. To get a true line of sight through the shell, we need the complete shell and must expand our analysis to use the appropriate information in the shell in three dimensions. To do this we use the orthogonal directions $\hat{x}$, $\hat{y}$ and $\hat{z}$. Since both $\hat{y}$ and $\hat{z}$ are perpendicular to the direction that lies parallel to the ambient magnetic field (formerly $\hat{x_1}$, now $\hat{x}$) nothing about the previous analysis is invalid. The only additional consideration we must now take into account is that a $2D$ plane for which we find the normal and tangential components will not lie parallel to any other $2D$ plane we use. In simpler terms, magnetic field components will have components in all three orthogonal directions. The shock propagation direction is assumed to lie parallel to the shock surface normal, which is purely radial ($\hat{n} = \frac{x}{r}\hat{x} + \frac{y}{r}\hat{y} + \frac{z}{r}\hat{z}$). The component of the ambient magnetic field that lies parallel to the shock normal is found using equation 3.15. The tangential upwind component is found using equation 3.16 and the post-shock tangential component is given by equation 3.17.

To understand how this full $3D$ shell contributes to the line of sight polarization, we use the derived shell properties to create synthetic polarization maps of a superbubble before the superbubble radius is greater than the effective scale height of the Dickey & Lockman (1990) galactic vertical HI profile. This analysis does not use a constant ambient density and magnetic field, nor a constant shell density. Instead the ambient density is defined by the galactic distribution described in §2.1.3 . The radial extent of the galaxy is set at $10kpc$. The density in the superbubble shell is found by using the appropriately located ambient density. Since the polarization is unaffected by magnetic field strength, the magnitude of the ambient field is unchanged with location, however, the magnetic field is modeled as a toroidal field to mimic a simple galactic field.

As before, we use our analytical determination of the field orientation and density in the shell to predict the detectability of the superbubble's effect on polarization. For our $3D$ shell we use GE 2.0 to create I, Q and U images. With these intensity images we create polarization maps for both emission from warm dust and the polarization

of starlight through transmission. In our previous analysis we ignored the true three dimensional nature of the shell properties, but it is not ignored in this analysis. We now also consider the effect of resolution on the detectability of superbubbles in dust polarization.

We know the shell thickness can be found with equation 3.9. Assuming the superbubble lies a distance D from us, the angular resolution needed to resolve the shell is then:

$$\Theta = sin^{-1}\left(\frac{\Delta r}{D}\right). \tag{3.21}$$

Substituting in equation 3.9 for the shell thickness Δr we find the angular size of the shell is dependent on angular location in the shell θ, the ratio of the temperature of shell to the ambient temperature, the Mach number, β, γ and the size of the superbubble. Both the Mach number and the size of the superbubble are dependent on the luminosity and age of the superbubble. The faster and younger the bubble, and the more thermal support in the shell the thinner the shell and the greater the resolution required to view it.

For a strongly cooled superbubble $1kpc$ away with a luminosity of $3x10^{39}\frac{ergs}{s}$ at an age of a 500,000 years expanding into an ISM with a field strength of $3\mu Gauss$ the resolution need to resolve the shell is $\sim 1.2arcmin$ in the galactic plane and $\sim 7.4arcmin$ at the top and bottom of the superbubble. We wish to create synthetic images of such a bubble located in a simulated galaxy with and without foreground and background contributions. We should be able to create images with the shell fully resolved near the galactic plane. The images we present here have a resolution of $\sim 1.5arcmin$, sufficient to resolve the shell for $\theta \geq 5\,\mathrm{deg}$. However, since the greatest expected change in the polarization was near $\theta \sim 15\,\mathrm{deg}$ from our $2D$ analysis, this resolution should be sufficient to rule out the possibility of detectable polarization changes from spherical superbubbles.

First we discuss the synthetic polarization maps from the transmission of starlight through dust grains. Here, we model unpolarized starlight from a wall of stars just behind the superbubble passing through the dust of the superbubble shell. The maps without foreground and background contribution only see extinction of light from the superbubble itself. The maps with foreground contributions model dust extinction from

the superbubble and dust in front of the superbubble along the light of sight. For this type of polarization the polarization vectors produced as light traverses the dust will lie parallel to the magnetic field lines.

Looking at Figures 3.7 and 3.9 we see that the polarization vectors nicely follow our expected field geometry, with significant vertical field and polarization components created from compression. This is particularly noticeable in Figure 3.7 where the shell below $\theta \lesssim 20\,\mathrm{deg}$ shows dramatically vertical polarization. It should be noted that though there are large components of vertical polarization, and so vertical components to the magnetic field, there are no regions of pure vertical polarization.

When foreground components are added, as can be seen in Figures 3.10 and 3.8 it seems that the effects of the superbubble disappear. Looking to Figure 3.8 we see that near the rim of the superbubble where the path length through the superbubble shell is greatest that the vertical polarization components produced by the superbubble are not detectable. Nor is any decrease in the net polarization there obviously detectable. To better determine whether the superbubble is affecting the polarization we create maps with the same unpolarized intensity wall of stars and foregrounds at the two galactic locations considered. These are seen in Figures 3.11 3.12. Comparing 3.12 to 3.10 we see that there is in fact some decrease in polarization near the center of the superbubble. However, comparing 3.12 to 3.10 it appears that the superbubble simply isn't detectable in polarization and that the large column depth in front of the superbubble prevents even the vertical polarization produced in the shell from noticeably decreasing the net polarization observed.

For the emission of polarized light from dust grains we produced maps of the superbubble with contributions only from the dust contained within the bubble itself and a map that included contribution from the foreground and background emission from the full path through the galaxy. Dust emission produces polarization perpendicular to the magnetic field, so polarization from the galaxy should lie perpendicular to the galactic plane. Figure 3.13 shows the polarized dust emission map expected from just the superbubble with our line of sight perpendicular to the ambient magnetic field. Near the shell the polarization shows a horizontal component, particularly for the region of the shell that would correspond to roughly $\theta \lesssim 70\,\mathrm{deg}$. Below $\theta \sim 20\,\mathrm{deg}$ we see near horizontal

polarization (meaning vertical field lines), but the polarization is very weak. It is possible that below 20 deg we would see greater change in polarization if we could resolve the shell better there. However, the reduction in percent polarization near $\theta \sim 0$ deg is likely representative of reality since we expect the field orientation to rotate rapidly from parallel to perpendicular to our line of sight along our line of sight in that region of the shell.

Figure 3.14 shows the polarized dust emission map expected from just the superbubble with our line of sight parallel to the ambient magnetic field. Without the presence of the superbubble a line of sight parallel to the magnetic field should produce no net polarization as the grains could orient themselves in any direction in the plane of the sky and so produce polarized light of any orientation. Therefore all the polarization visible in Figure 3.14 is produced by the superbubble. Most notable about this polarization map is the location of the greatest polarization vectors. For this orientation of the superbubble to our line of sight, the magnetic field orientation in the shell at the edges of our view of the bubble is parallel or nearly so to our line of sight. Regions which appear to us as the interior of the superbubble show much larger polarization. The polarization there is still being produced by the shell, not by the interior, however the shell here has large components of the magnetic field which are perpendicular to our line of sight. The percentage of net polarization is nearly what the polarization that would be produced by a field line lying perfectly perpendicular to our line of sight for locations that appear near the center of the superbubble. However, the strength of the polarization drops off away from this region and it is questionable that if there were contribution to this map from foreground dust oriented by a magnetic field line perpendicular to our line of sight, the polarization seen in Figure 3.14 would be detectable. On the other hand, it is possible though that a reduction in net polarization would be observed.

Adding foreground and background dust we see that the detectability of the polarization structure of the superbubble is very dependent on the line of sight. This dichotomy can be seen in Figures 3.15 and 3.16. For Figure 3.15 we modeled a superbubble located towards galactic center, where the ambient local field would lie perpendicular to our line of sight. As can be expected the tremendous column density through this path swamped the polarization produced by the superbubble and left it nearly undetectable

in polarization (though still visible in unpolarized intensity.) Some change in polarization structure is still visible along the rim brightened shell near $\theta \sim 45\,\mathrm{deg}$, but with any turbulent structure in the foreground or background magnetic field this small change in polarization is likely not detectable.

Figure 3.16 shows our model of a superbubble at approximately to $(l, b) = (80, 0)$. (This superbubble is located 1kpc distant at a location where the local magnetic field is perpendicular to our line of sight). The line of sight for this map has a much shorter path through the galaxy and therefore a much smaller column depth. There is also the advantage that this orientation of the superbubble with respect to our line of sight provides a larger area over which the superbubble produces a change in polarization since this occurs over nearly the whole area of the superbubble image and not just along the rim.

The effect of the superbubble on dust emission polarization is predictably reduced when the superbubble is placed at a larger distance from the observer. Figure 3.17 shows a superbubble located 3kpc from the observer at a galactic location of $(l, b) \sim (70, 0)$ (location where the local magnetic field is perpendicular to our line of sight). Using the same resolution as the previous images ($1.5 arcmin$) means that the shell is less resolved. However, there is still a detectable change in polarization. Though this durability in polarization signature with distance lends itself to plausibility of detecting superbubble polarization.

The effect of a still spherical superbubble on dust emission polarization and interstellar polarization is not terribly robust, though under some optimistic conditions it might be detectable. To further determine the effect superbubbles have on such observations we continue our study of superbubbles by modeling superbubbles that have grown larger than the effective scale height of the galaxy, breakthrough superbubbles, in Chapter 4.

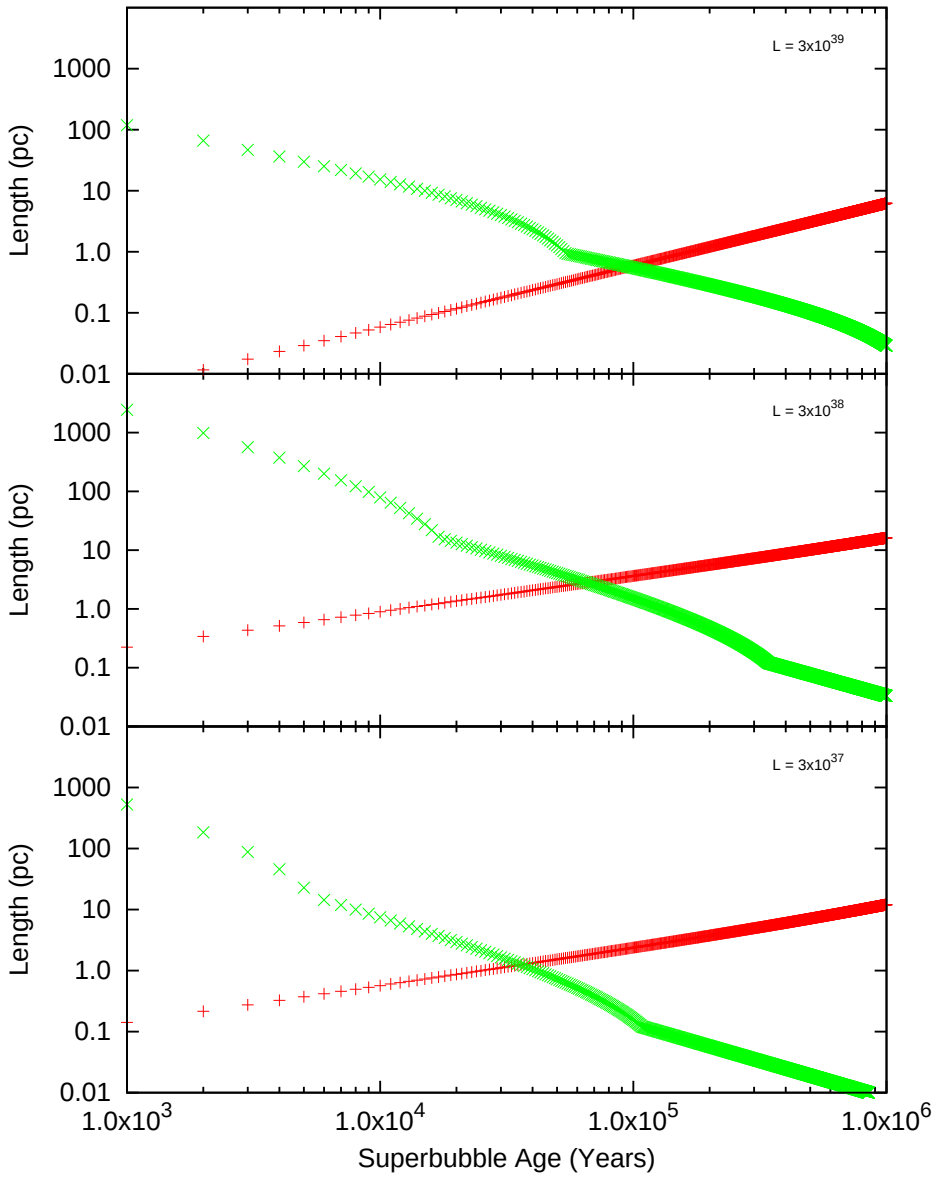

Figure 3.1 Comparison of the cooling length vs the age of the bubble and the shell width vs the age of the bubble. The cooling length is shown by 'x' marks, and the shell width by the crosses.

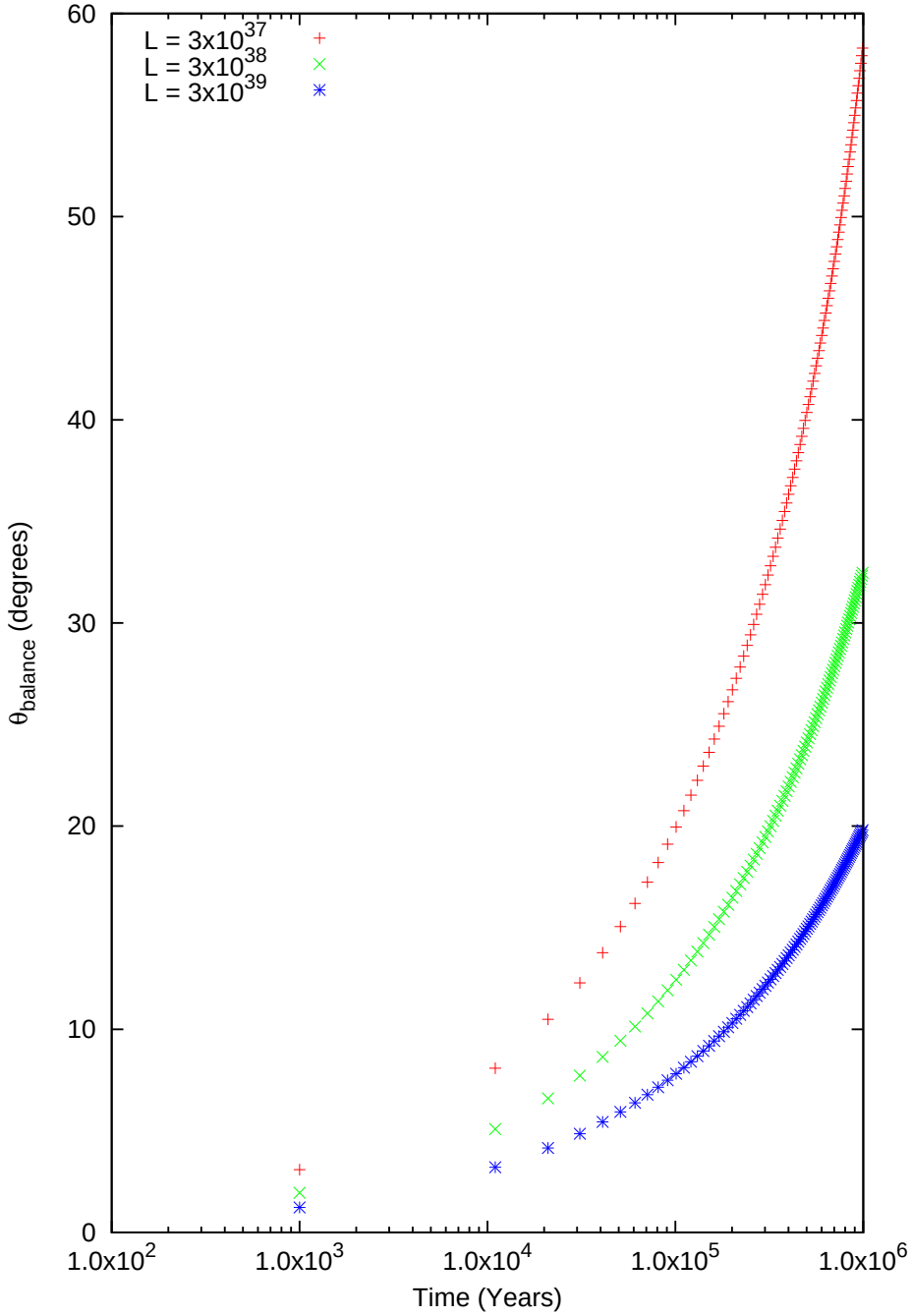

Figure 3.2 The change in $\theta_{balance}$, the location in the shell at which magnetic and thermal pressure support should balance, with superbubble luminosity and age.

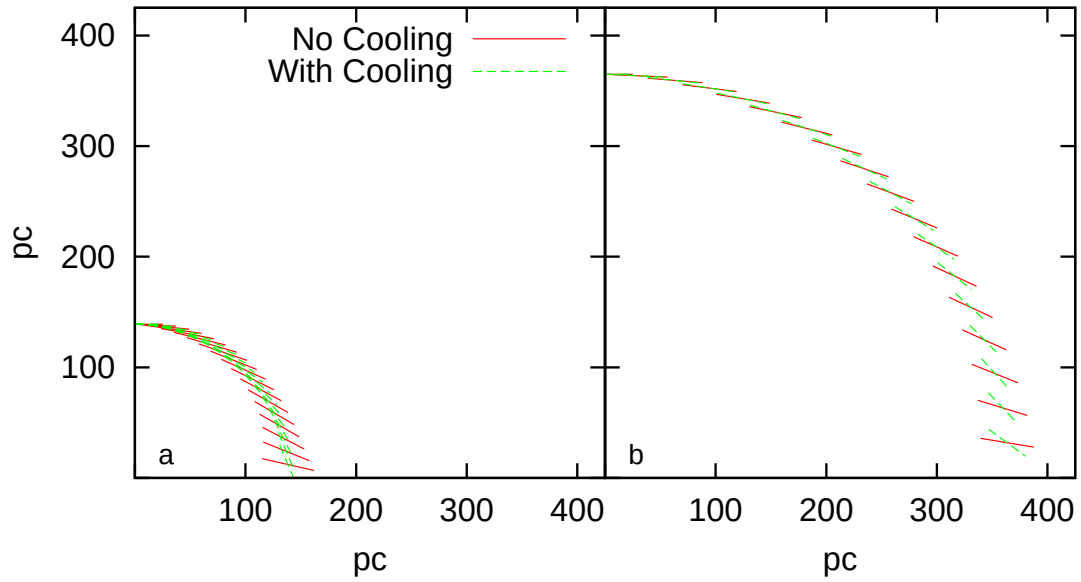

Figure 3.3 Comparison of adiabatic (no cooling) and isothermal (strong cooling) shocks for a superbubble with a luminosity of $3x10^{39} ergss^{-1}$ at a time of (a) 10^6 years and (b) $5x10^6$ years with no foreground or background.

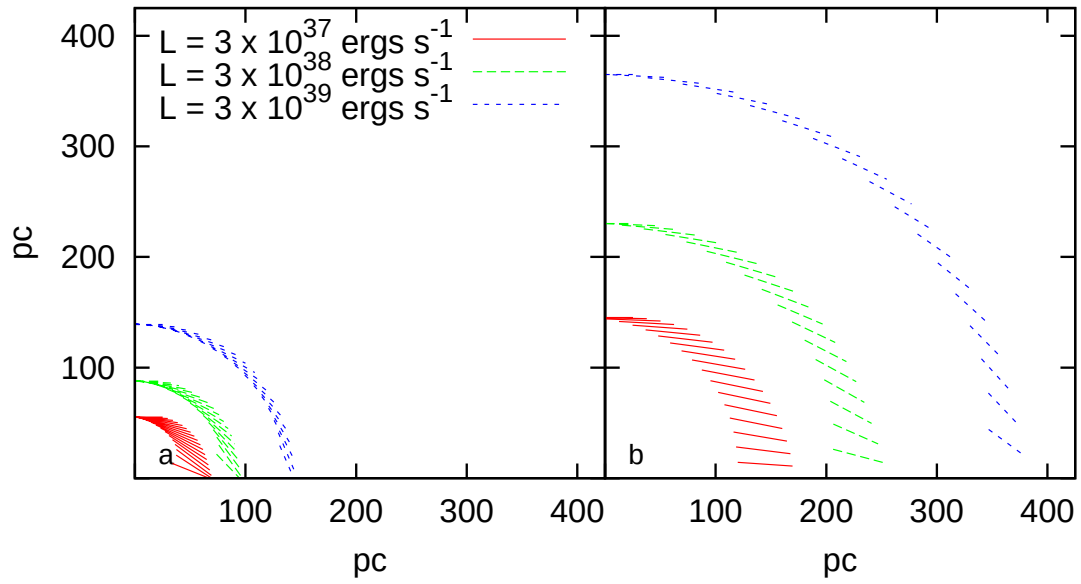

Figure 3.4 Comparison of three luminosities $3x10^{37}, 3x10^{38}$, and $3x10^{39} ergss^{-1}$ at a time of (a) 10^6 years and (b) $5x10^6$ years with no foreground or background.

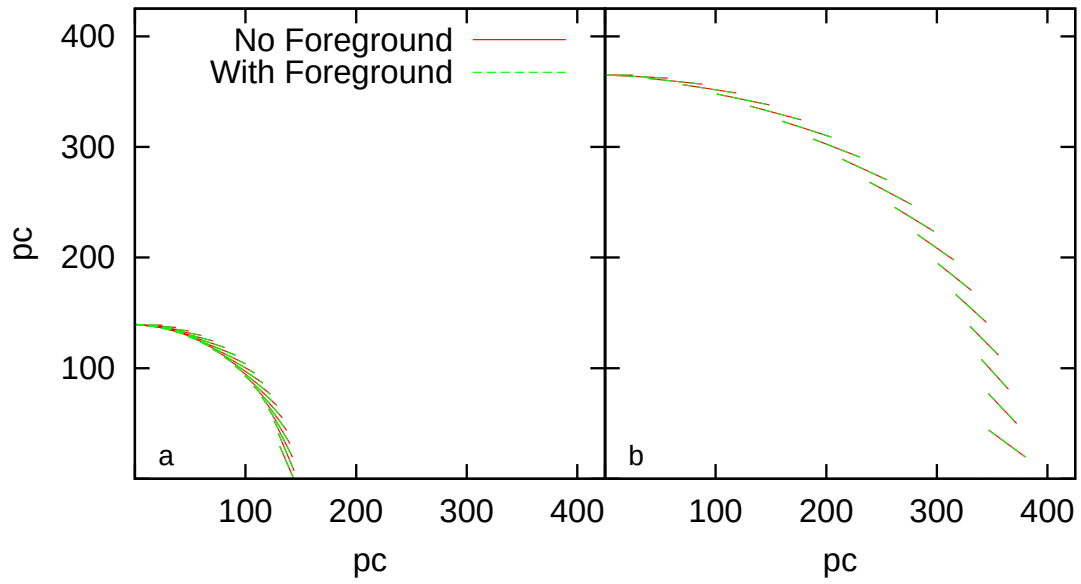

Figure 3.5 Comparison of a superbubble with a luminosity of $3x10^{39} ergs s^{-1}$ at a time of (a) 10^6 years and (b) $5x10^6$ years with foreground and background to one without either.

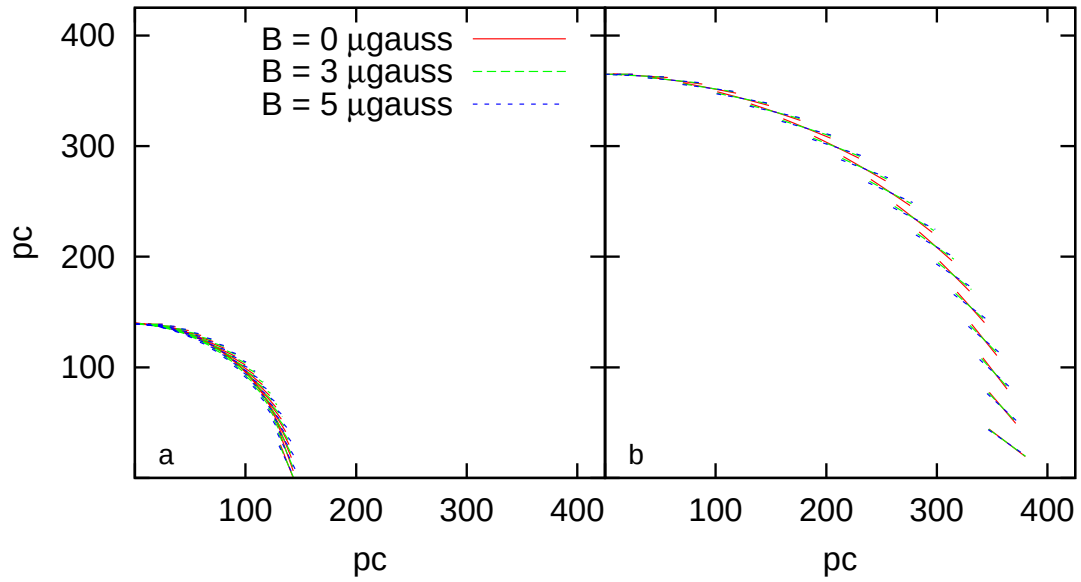

Figure 3.6 Comparison of a superbubble with a luminosity of $3x10^{39} ergs s^{-1}$ at a time of (a) 10^6 years and (b) $5x10^6$ years with an isothermal shock in three environments, no magnetic field, a field of 3 microGauss and a field of 5 microGauss.

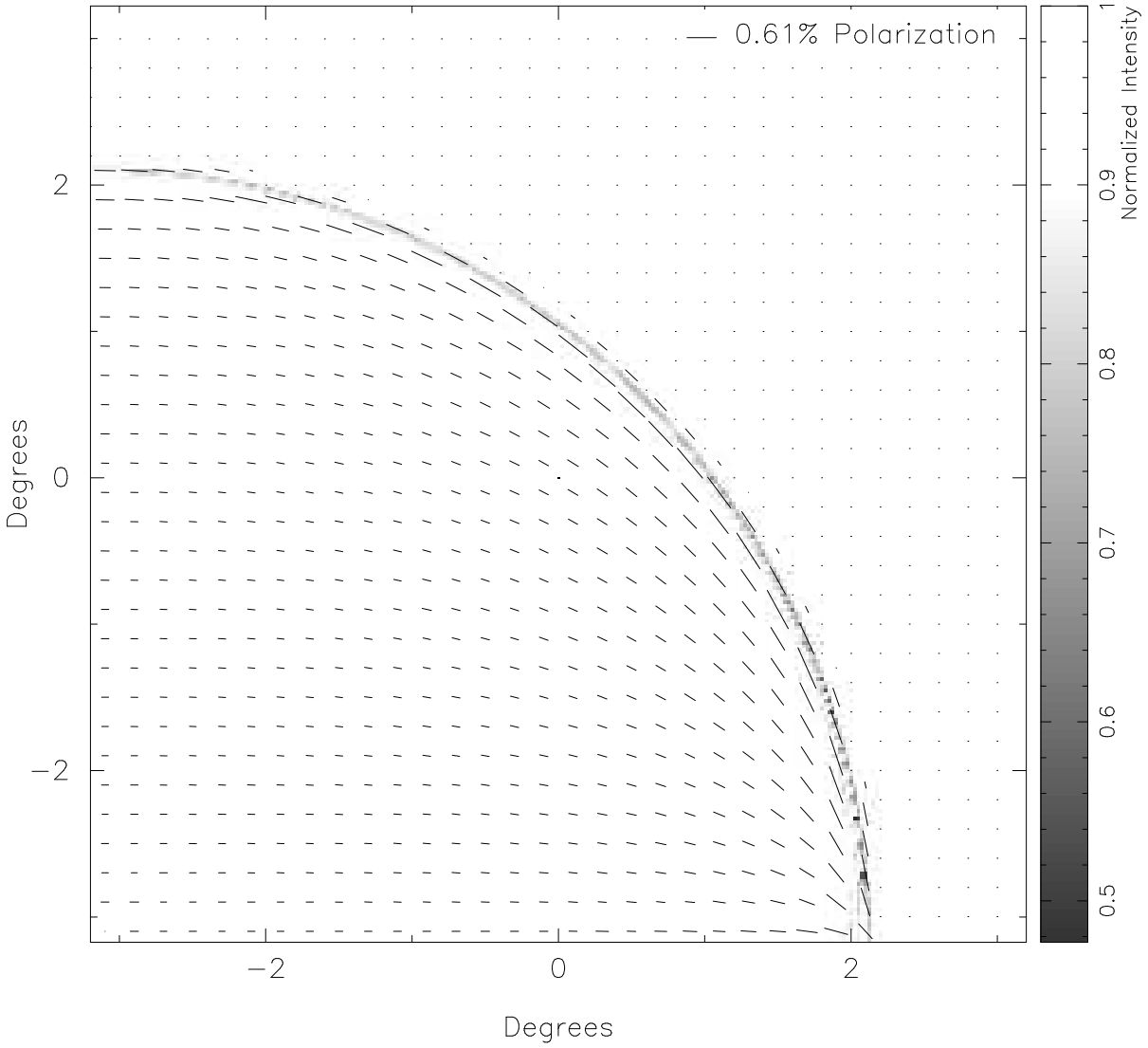

Figure 3.7 Polarization map from 2.2 micron unpolarized starlight passing through a superbubble with a line of sight perpendicular to undisturbed magnetic field $(l, b) = (0, 0)$ at 1kpc distance from observers. Foreground neglected. Resolution 1.5 arcmin for intensity, polarization vectors have a resolution of 6 arcmin.

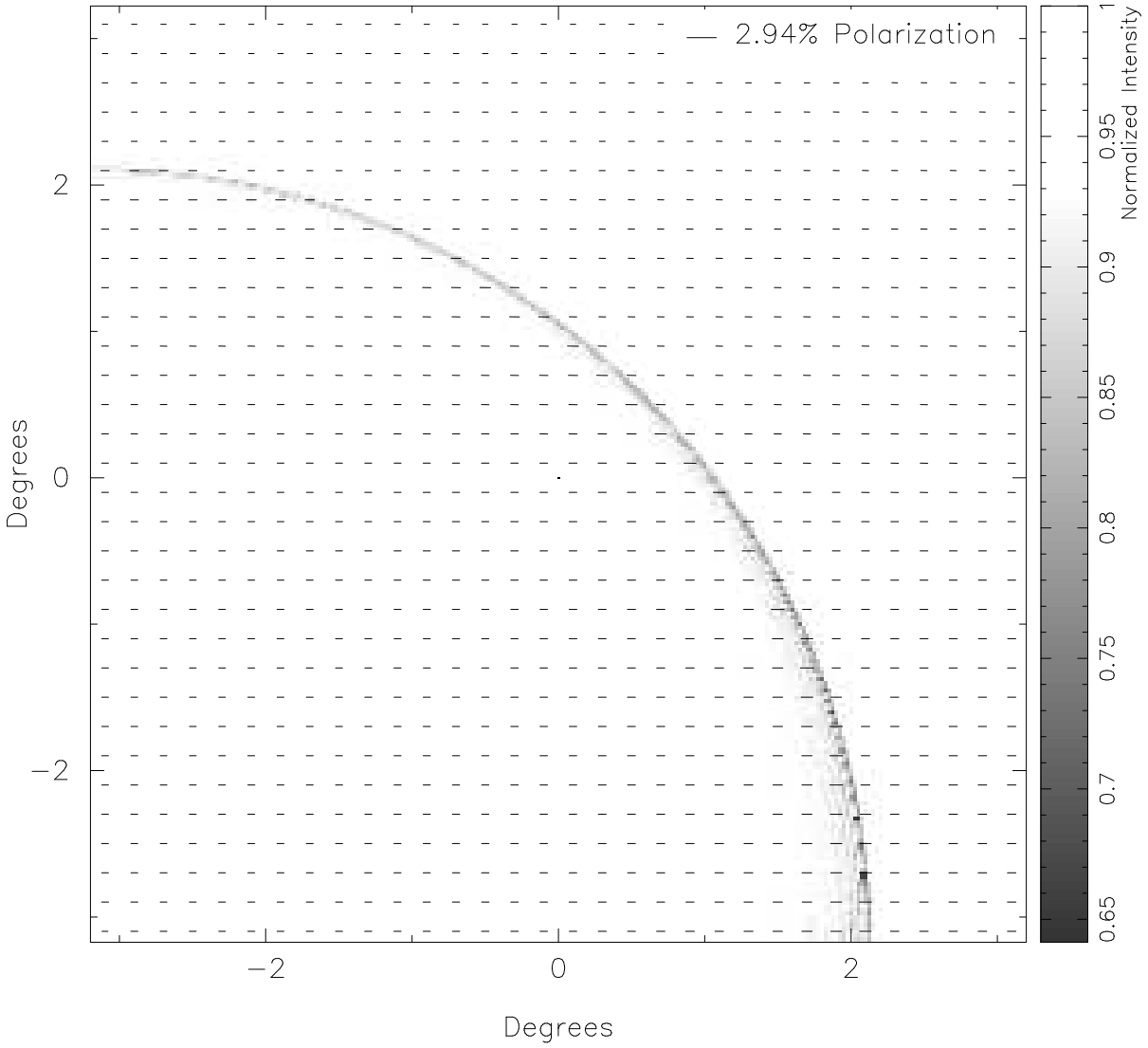

Figure 3.8 Polarization map from 2.2 micron unpolarized starlight passing through a superbubble with a line of sight perpendicular to undisturbed magnetic field $(l, b) = (0, 0)$ at 1kpc distance from observers. Foreground components included. Resolution 1.5 arcmin for intensity, polarization vectors have a resolution of 6 arcmin.

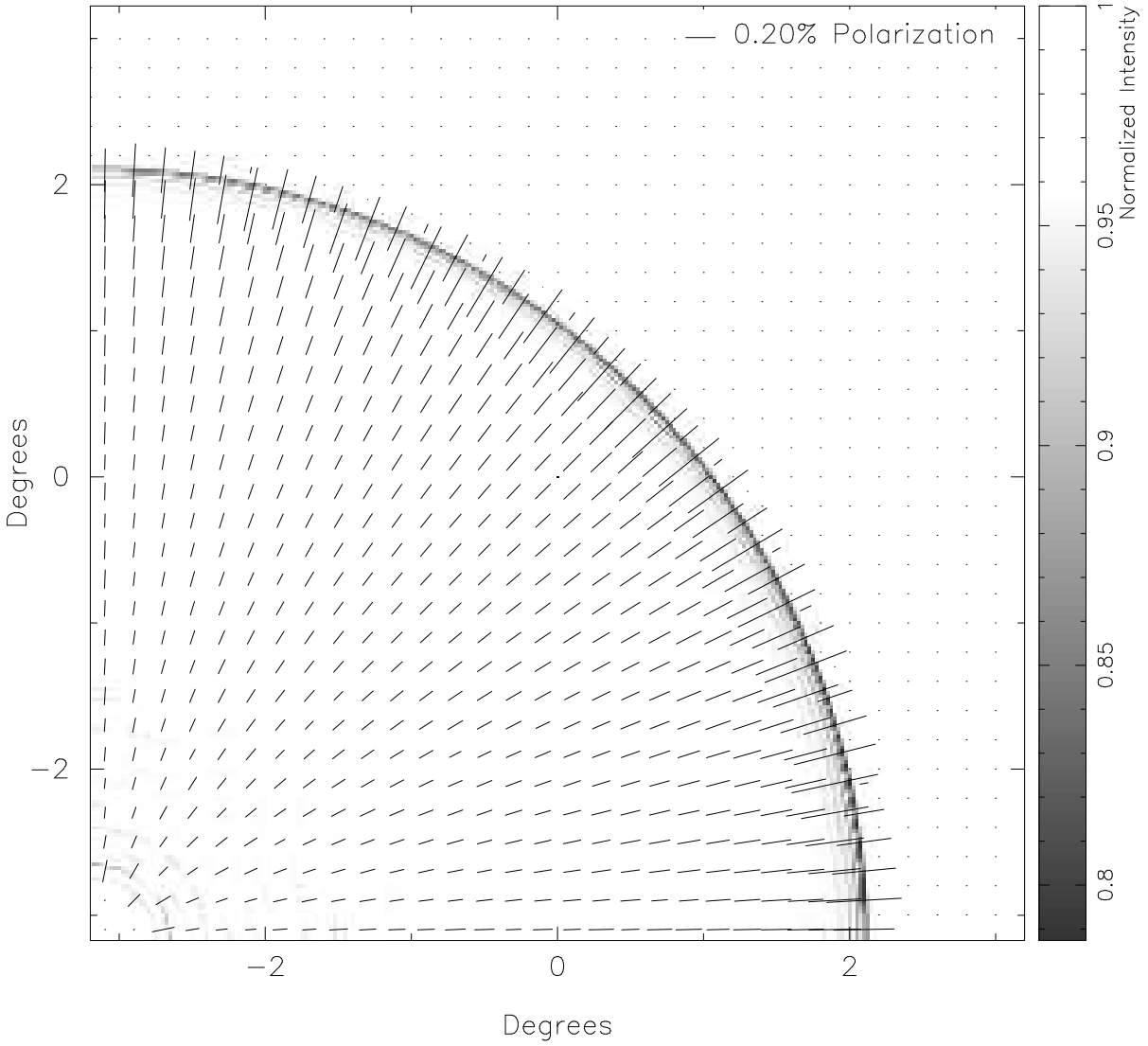

Figure 3.9 Polarization map from 2.2 micron unpolarized starlight passing through a superbubble with a line of sight parallel to undisturbed magnetic field $(l, b) \sim (80, 0)$ at 1kpc distance from observers. Foreground neglected. Resolution 1.5 arcmin for intensity, polarization vectors have a resolution of 6 arcmin.

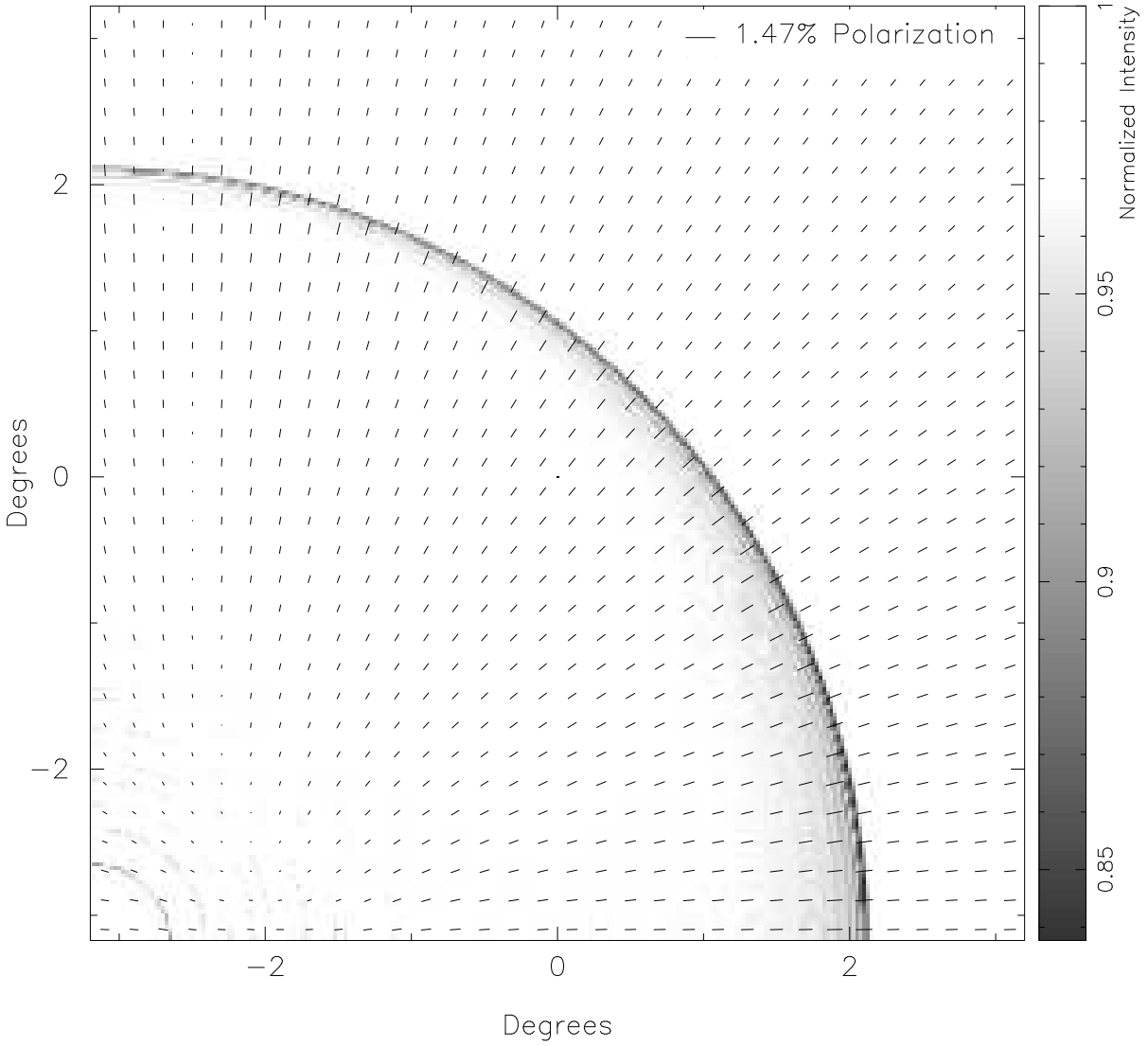

Figure 3.10 Polarization map from 2.2 micron unpolarized starlight passing through a superbubble with a line of sight parallel to undisturbed magnetic field $(l, b) \sim (80, 0)$ at 1kpc distance from observers, foreground components included. Resolution 1.5 arcmin for intensity, polarization vectors have a resolution of 6 arcmin.

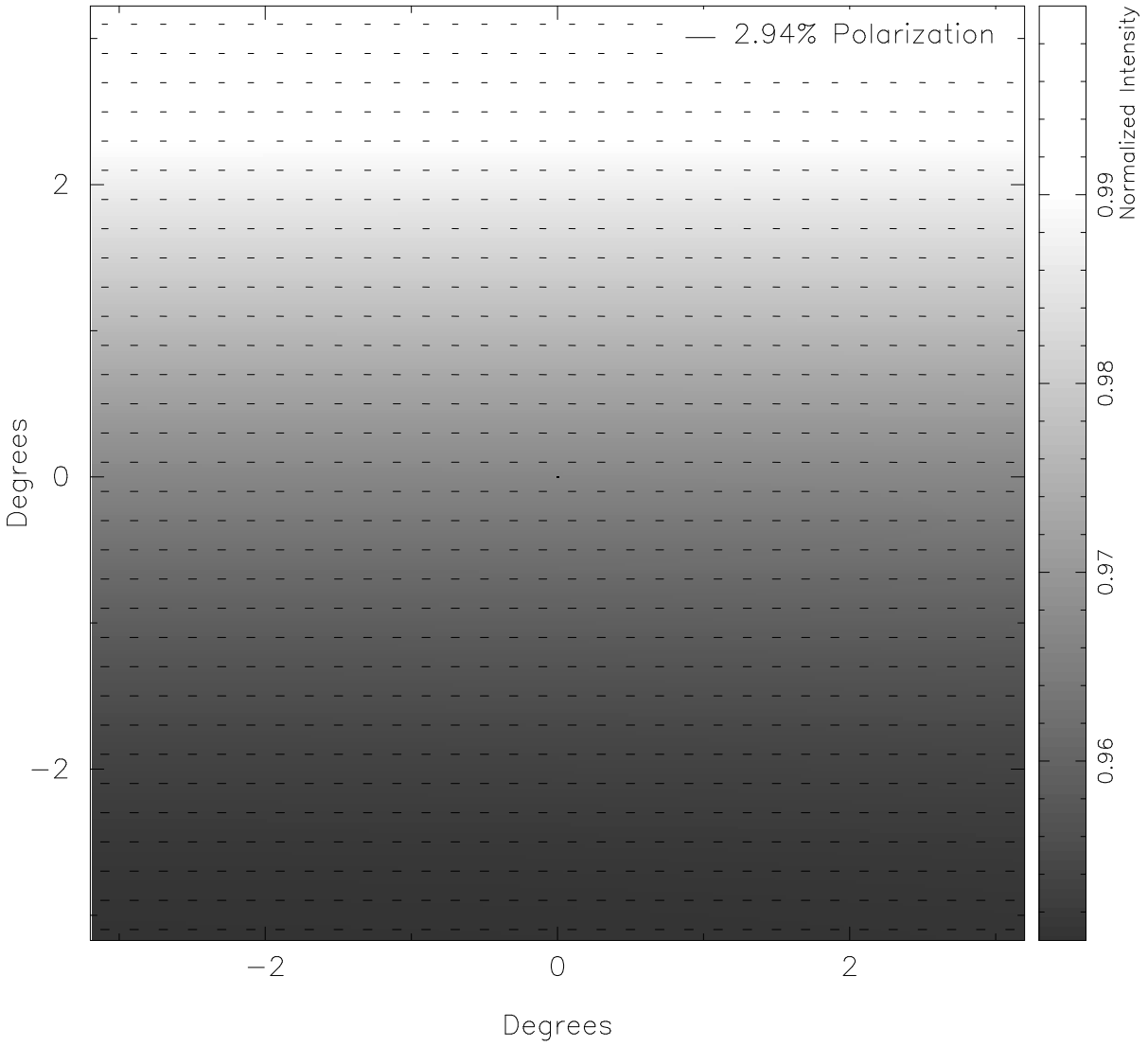

Figure 3.11 Polarization map from 2.2 micron unpolarized starlight passing through a galactic dust foreground with a line of sight perpendicular to the local undisturbed magnetic field $(l, b) = (0, 0)$ at 1kpc distance from observers. Resolution 1.5 arcmin for intensity, polarization vectors have a resolution of 6 arcmin.

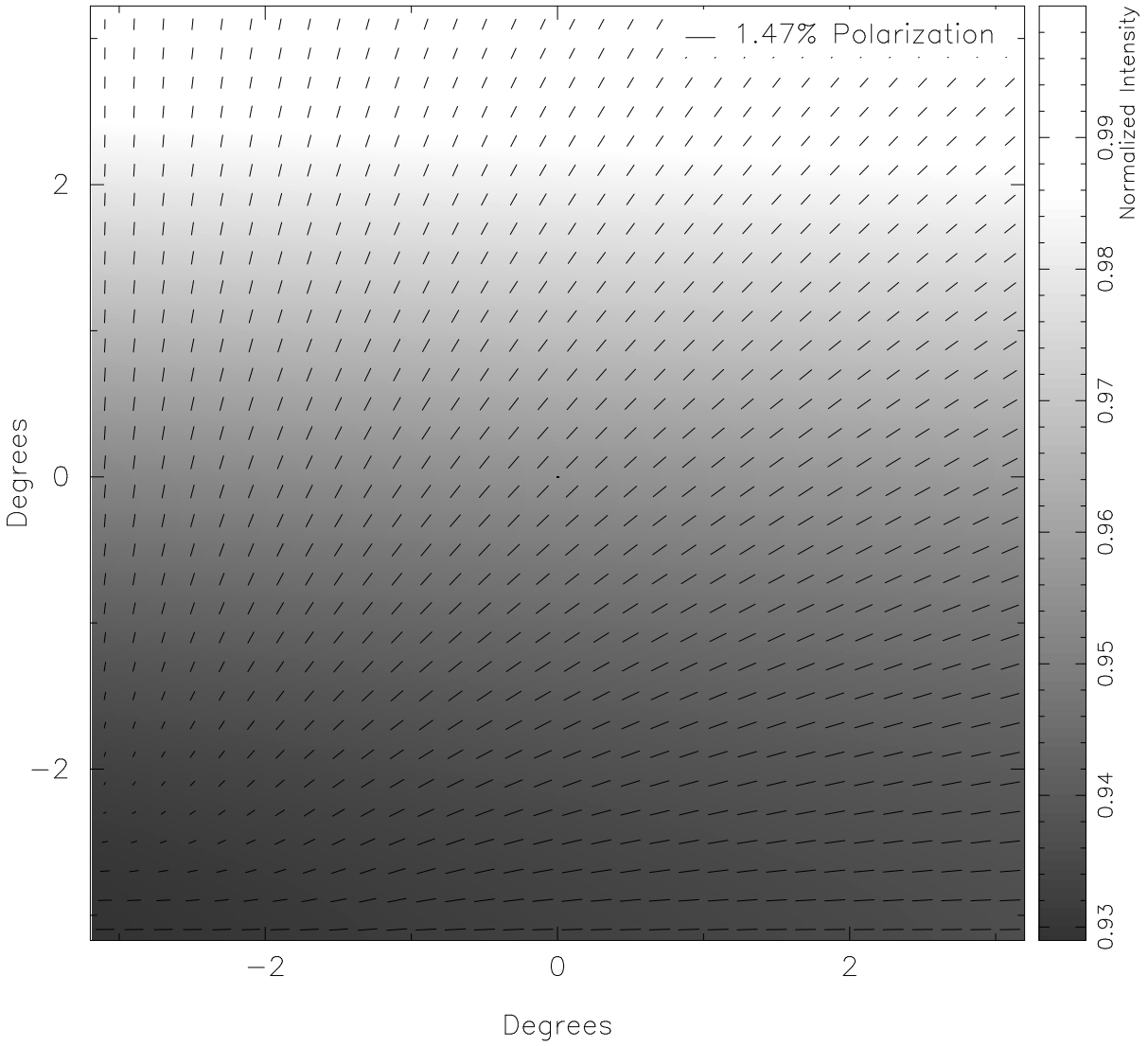

Figure 3.12 Polarization map from 2.2 micron unpolarized starlight passing through a galactic dust foreground with a line of sight parallel to the local undisturbed magnetic field $(l, b) \sim (80, 0)$ at 1kpc distance from observers. Resolution 1.5 arcmin for intensity, polarization vectors have a resolution of 6 arcmin.

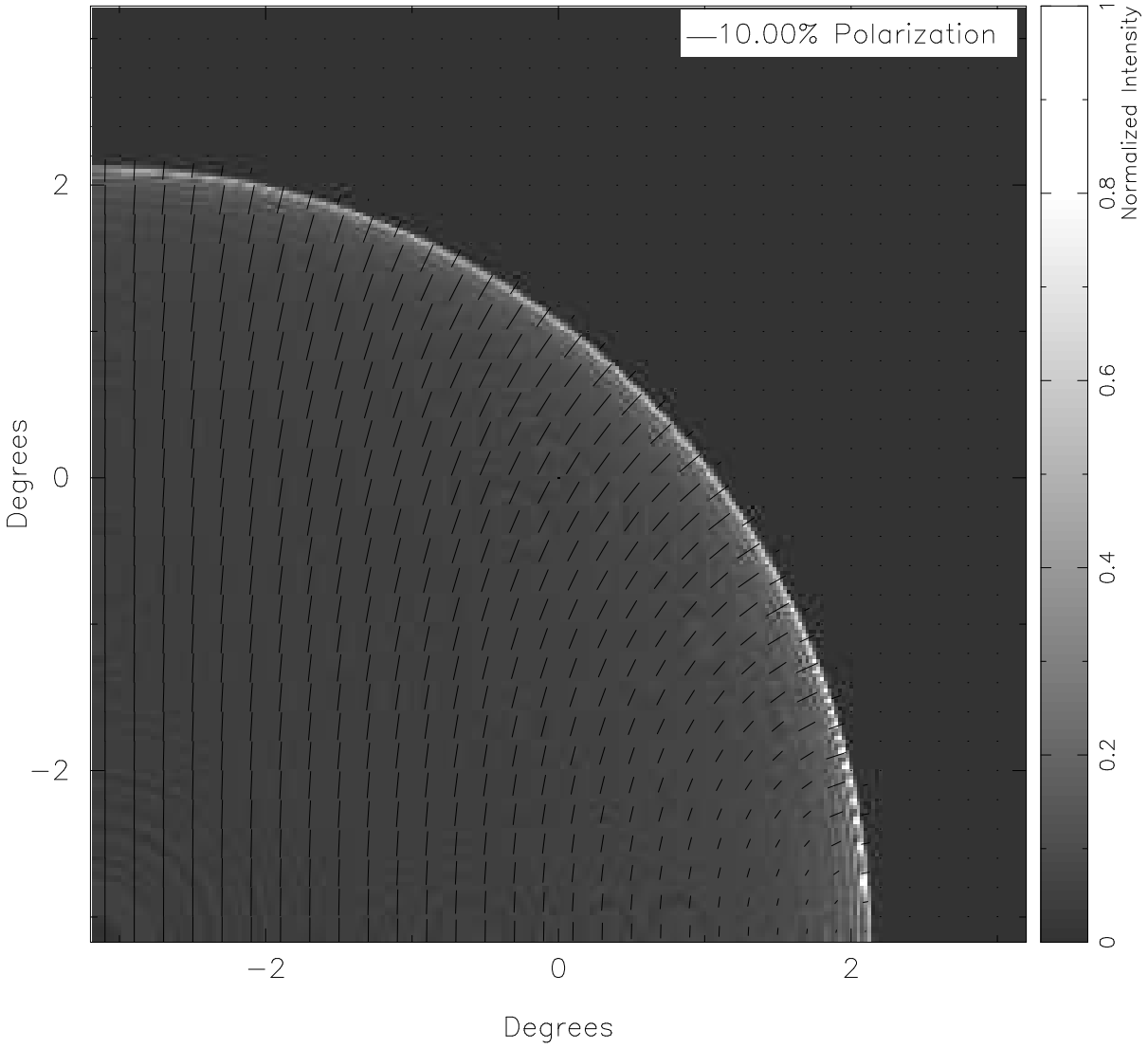

Figure 3.13 Polarization map from 100 micron dust emission from a superbubble with a line of sight parallel to undisturbed magnetic field at 1kpc distance from observers ($(l, b) \sim (80, 0)$). Foreground and background neglected. Resolution 1.5 arcmin for intensity, polarization vectors have a resolution of 6 arcmin.

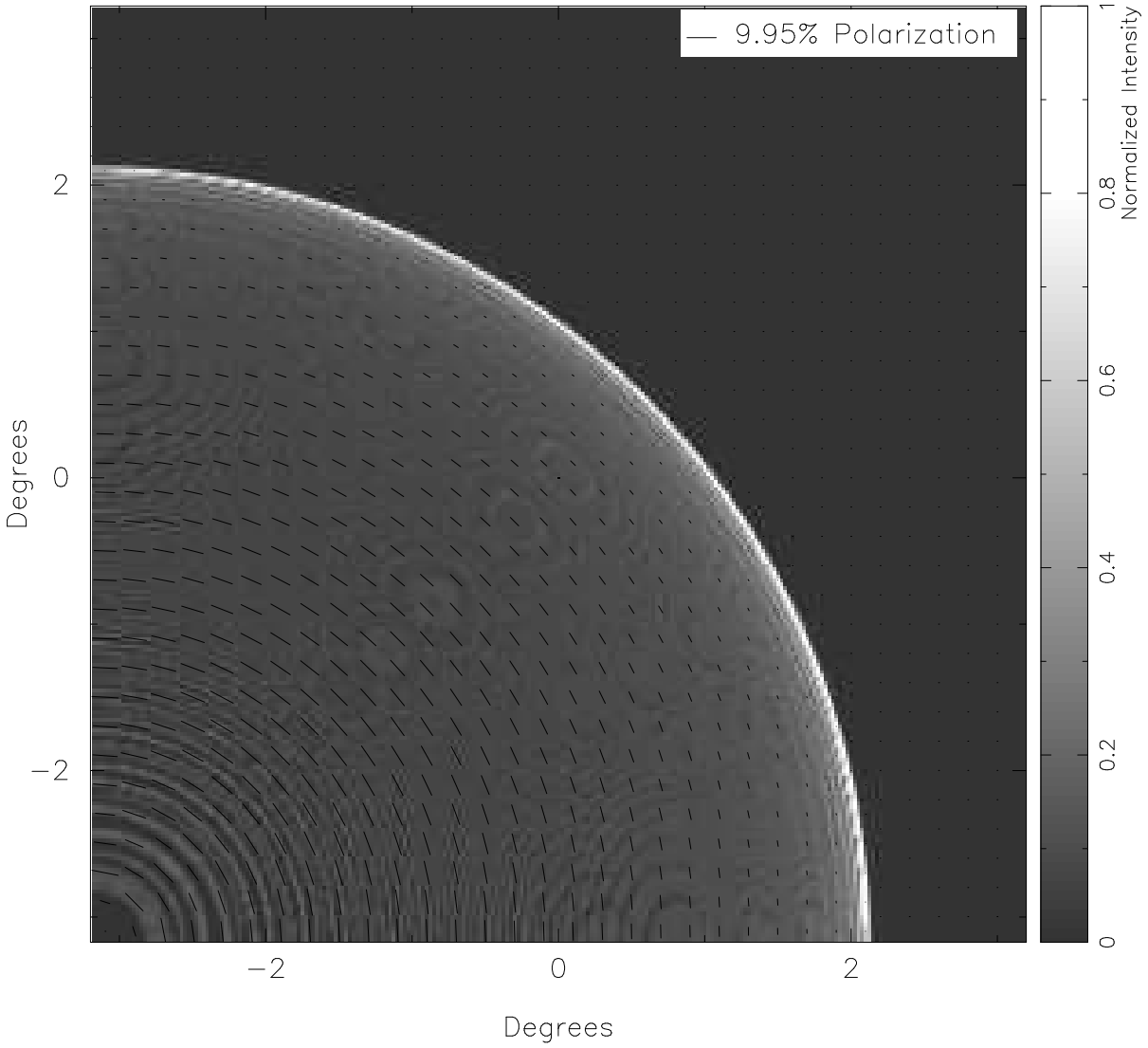

Figure 3.14 Polarization map from 100 micron dust emission from a superbubble with a line of sight perpendicular to undisturbed magnetic field at 1kpc distance from observers ($(l, b) = (0, 0)$). Foreground and background neglected. Resolution 1.5 arcmin for intensity, polarization vectors have a resolution of 6 arcmin.

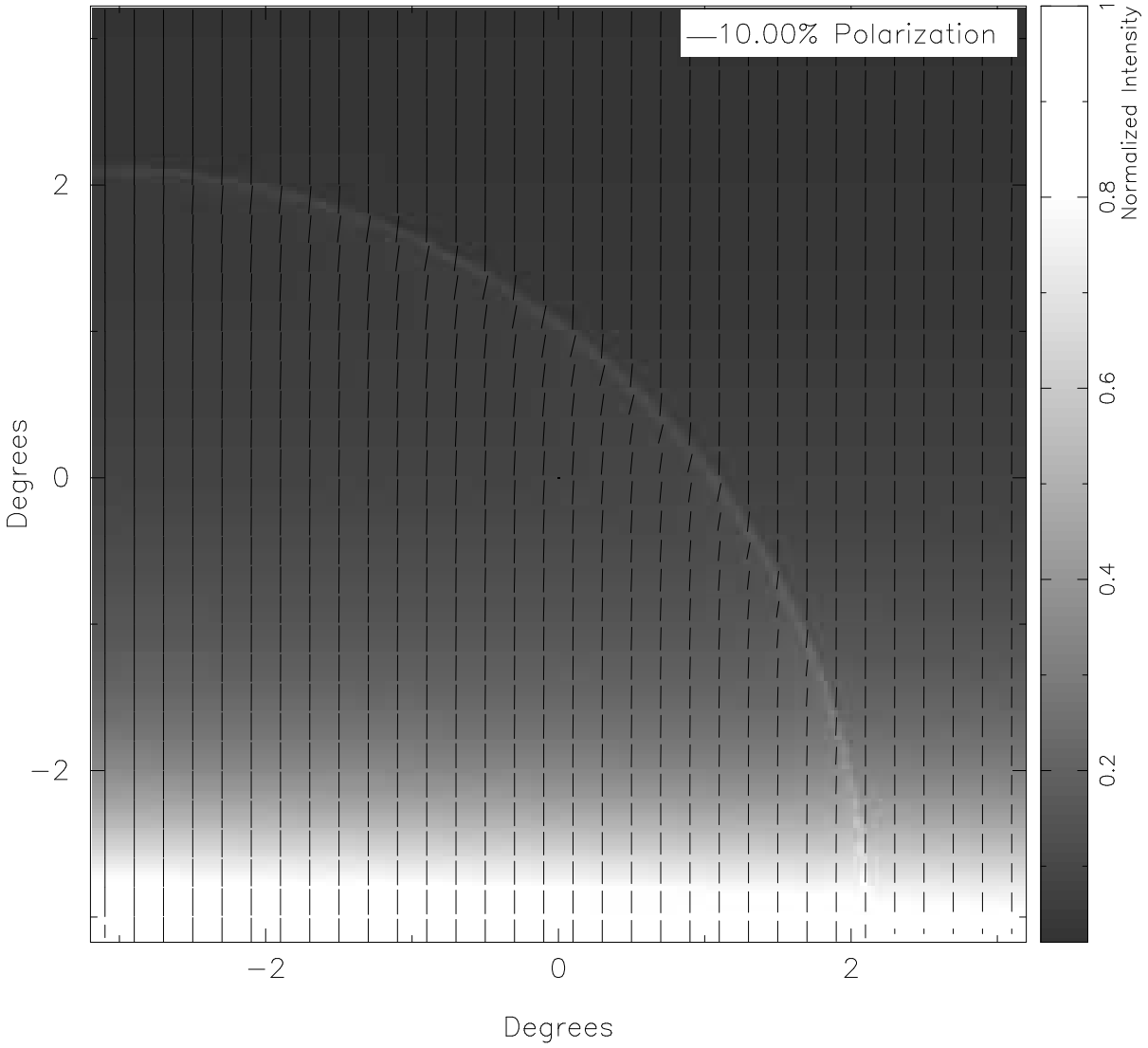

Figure 3.15 Polarization map from 100 micron dust emission from a superbubble at galactic coordinates $(l, b) = (0, 0)$ 1kpc distance from observers, foreground and background components included. Resolution 1.5 arcmin for intensity, polarization vectors have a resolution of 6 arcmin.

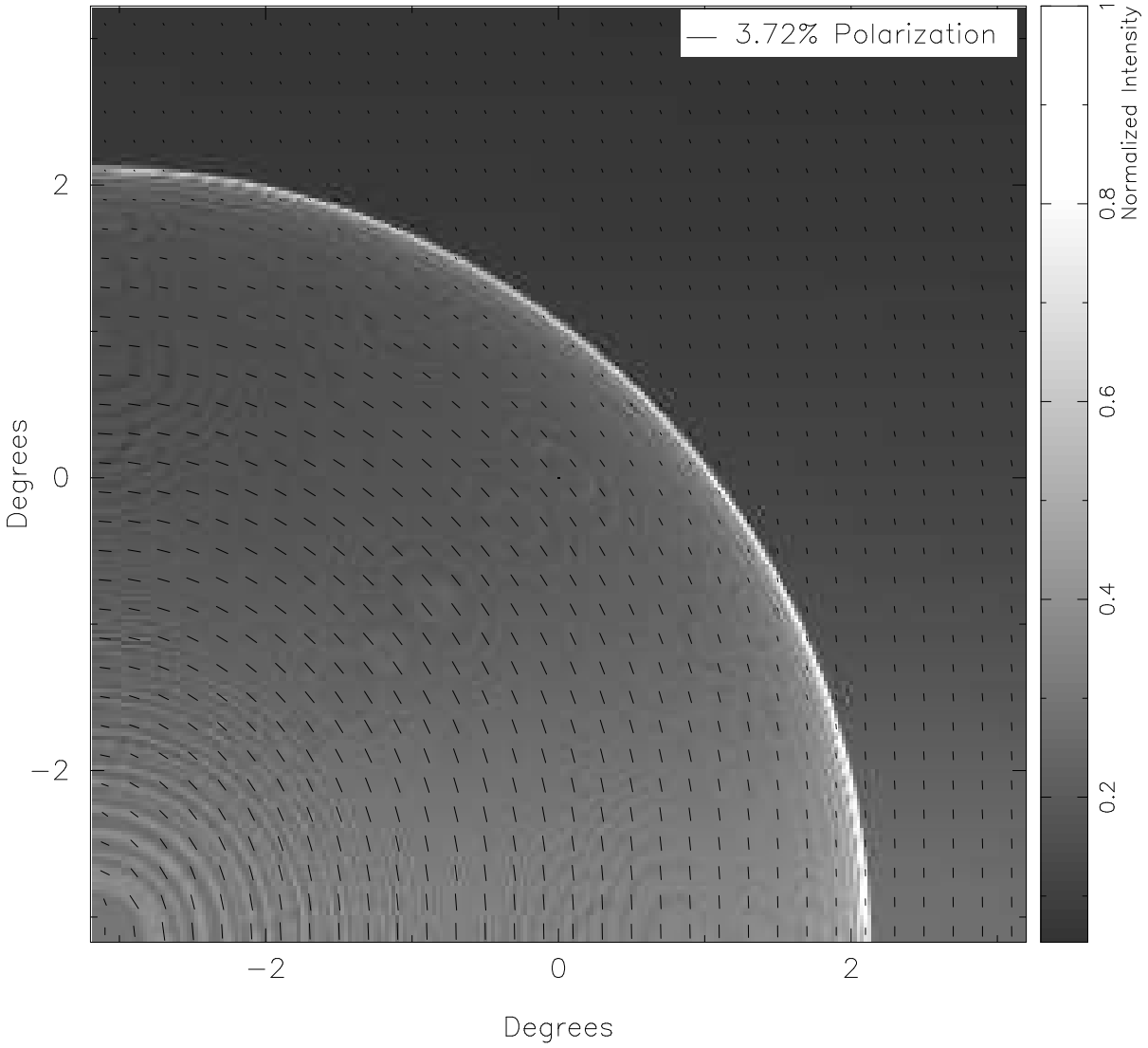

Figure 3.16 Polarization map from 100 micron dust emission from a superbubble at galactic coordinates $(l, b) \sim (80, 0)$ 1kpc distance from observers, foreground and background components included. Resolution 1.5 arcmin for intensity, polarization vectors have a resolution of 6 arcmin.

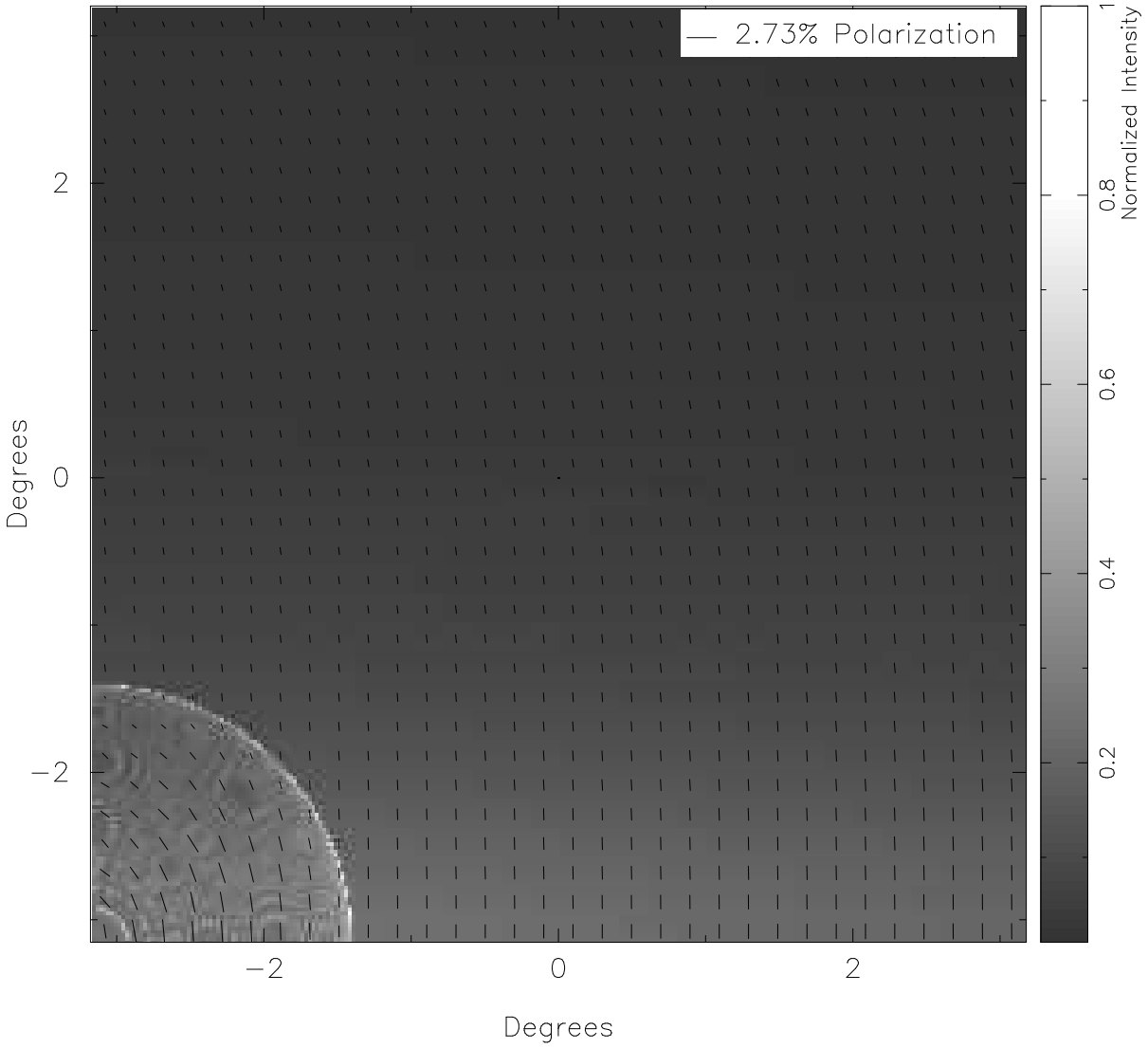

Figure 3.17 Polarization map from 100 micron dust emission from a superbubble at galactic coordinates $(l, b) \sim (70, 0)$ 3kpc distance from observers, foreground and background components included. Resolution 1.5 arcmin for intensity, polarization vectors have a resolution of 4 arcmin.

Chapter 4

Superbubbles After Breakthrough

We create a semi-analytical description of a constant luminosity superbubble in an exponential atmosphere. Most of the work in this section to solve the hydrodynamical case follows the modification to Kompaneets (1960) by Basu et al. (1999). While in a uniform atmosphere, the forward shock would follow a self-similar condition whose dependency on time would be controlled by the nature of the energy injection, point source energy deposition into a stratified atmosphere would be affected by the gradient in pressure and density. The Kompaneet's approximation describes a one-time energy injection [1] of sufficient energy to create a shock wave that remains a strong shock even when the blast radius is larger than the scale height of the gas. Such an explosion would 'see' the gradient in the atmosphere and diverge from a spherical self similar solution to one elongated as the superbubble preferentially expanded perpendicular to the plane of the atmosphere. The 'top' and 'bottom'[2] of the bubble in the Kompaneet's approximation accelerate to an infinite height in a finite time, while the external pressure of the atmosphere eventually reaches an equilibrium with the internal pressure and the expansion in the plane stalls. The result is a long tube-like structure perpendicular to the plane of the atmosphere. Applying this reasoning to superbubbles in disk galaxies

[1] We follow Basu et al. (1999) and modify the energy input to reflect a constant luminosity instead of a blast.

[2] If the injection location is centered in the plane then the top and bottom of the superbubble behave identically, this is not the case for a superbubble that is not centered on the plane.

and assuming the field remains 'frozen-in' to the gas, this has the potential to create magnetic field components also perpendicular to the plane.

4.1 Semi-analytical Superbubble Development in a Stratified Atmosphere: Kompaneet's Approximation

The Kompaneet's approximation assumes a strong shock velocity with direction parallel to the shock normal and uniform pressure in the bubble. Like Basu et al. (1999) we maintain these assumptions. The most important difference from the Kompaneet's approximation is the input of energy, where instead of a one time input of energy, the superbubble is driven by a constant luminosity. The first Law of Thermodynamics gives us the change in thermal energy if we assume that the only energy lost from the constant luminosity put into the bubble is in work done to evacuate the interior gas to the shell of the bubble.

$$\frac{dE_{them}}{dt} = L_0 - P\frac{d\Omega}{dt} \tag{4.1}$$

Where Ω is the volume of the superbubble, given by:

$$\Omega = \pi \int_{z_1}^{z_2} r(z,t)^2 dz \tag{4.2}$$

Where z_1 and z_2 are the bottom and top of the bubble. By assuming elements of the shock front always propagate perpendicular to the shock surface the equation describing the shock front is given by Kompaneets (1960) as:

$$\left(\frac{\partial r}{\partial t}\right) - v^2\left[1 - \left(\frac{\partial z}{\partial z}\right)\right] = 0 \tag{4.3}$$

To solve this equation, Kompaneet's substituted in the variable y and solved the resulting equation with separation of variables. The variable y is defined as:

$$y = \int_0^t \sqrt{(\frac{\gamma^2+1}{2})}\sqrt{(\frac{E_{thm}}{\rho_0 \Omega})}dt. \tag{4.4}$$

Where E_{thm} is the thermal energy interior to the forward shock and Ω is the volume of the region interior to the forward shock. This equation relates y, which is a variable

with a unit of length, to the time in a not necessarily linear way. The solution to equation 4.3 after this substitution is:

$$r(z,y) = 2Harccos(\frac{exp(\frac{z}{2H})}{2}\left(1 - \frac{y^2}{4H} + exp(\frac{-z}{H})\right)) \tag{4.5}$$

Where H is the scale height of the gas. As pointed out by Basu et al. (1999), the entire development of the Kompaneet's bubble form can be found by plotting r and z for any y between 0 and $2H$. [3] However, we are not only interested in the shape of the superbubble shock front, but the density of the shell and geometry of the magnetic field, which requires information about the evolution with time.

We wish to find the superbubble age at any given y. As suggested by Basu et al. (1999) all of our numerical work was done in dimensionless form, with the scales for time, energy, pressure and so on set by the three parameters H, L_0 and ρ_0. Dimensionless forms are noted by an asterisk (e.g. $y* = \frac{y}{H}$).

Basu et al. (1999) claim that they numerically integrate equations 4.4 and 4.1 to obtain $E(t)$ and $y(t)$. Since it is not possible to obtain the derivative of the volume with respect to t without knowing r(z,t) (which we do not have and cannot have without knowing how t relates to y) we came up with an alternative solution method. In dimensionless form, equation 4.4 can be written as:

$$\frac{dt*}{dy*} = \sqrt{(}\frac{2}{\gamma^2+1})\sqrt{(}\frac{\Omega*}{E_{thm}*}). \tag{4.6}$$

Which can be multiplied through the dimensionless form of equation 4.1 to obtain:

$$\frac{dE_{thm}*}{dy*} = \sqrt{(}\frac{2}{\gamma^2-1})\sqrt{(}\frac{\Omega*}{E_{thm}*}) - (\gamma-1)\frac{E_{thm}*}{\Omega*}\frac{d\Omega*}{dy*} \tag{4.7}$$

This equation can be numerically integrated to give the thermal energy as a function of $y*$ by first numerically solving for the volume (with the radius, $r*$, as a function of $z*$ and $y*$.) Once we have found the thermal energy and volume at this $y*$, we can use equation 4.6 to solve for the dimensionless time, $t*$ given a $y*$.

To find the density in the shell using the jump-shock conditions, it is necessary

[3] We evaluated our Kompaneet's like superbubble with it centered at the mid-plane of the galaxy. This requires modifying equation 4.5 to use the absolute value of z. The absolute value of z is used in finding the density of the ambient gas as well.

to find the Mach number. Since the Kompaneet's approximation assumes a uniform internal pressure it is possible to solve for the velocity using:

$$v = \sqrt{(}\frac{\gamma+1}{2}\frac{P(t)}{\rho(z)}). \tag{4.8}$$

The pressure can be found simply as:

$$P = (\gamma - 1)\frac{E_{thm}}{\Omega} \tag{4.9}$$

and the density is found using the already assumed exponential atmosphere:

$$\rho = \rho_0 exp(\frac{-z}{H}). \tag{4.10}$$

As already mentioned, to create synthetic polarization observations we will need the shell thickness (where we define the shell as the region between the forward shock and the contact discontinuity), shell average density and the shell average field orientation. All three of these parameters are expected to change under conditions of strong cooling. The strength of the magnetic field will also play a key role in determining the properties of the shell as the field can provide pressure support under the right conditions. First we will consider the weak field case with the field contributing a negligible degree to the dynamics of the gas.

4.1.1 Streamlines

In the spherical blast case the expansion was always assumed to be radial, with the trajectories of the shock surface following straight lines. This information was vital to finding the shell thickness in both the hydro and magnetically supported limits. However, for expansion into a non-uniform atmosphere, it is not necessarily the case that the expansion will follow straight lines. Basu et al. (1999) term the trajectory of shock front elements as 'streamlines', we keep with this nomenclature.

Since streamlines are necessary to provide information for our analytical determination of shell properties it is useful discuss how they are found. The assumption in the Kompaneet's approximation of shock propagation always being directed perpendicular to the current shock front surface can be used to trace the trajectory of the shock front.

Newman et al. (1999) analytically solved for these streamlines as a function of time using the initial propagation angle θ. Given a location on the forward shock in cylindrical coordinates, r and z (r can be found using z at any given y using equation 4.5) Newman et al. (1999) found that the initial angle of propagation for that streamline from the zenith is:

$$\Theta(r,z) = arctan\frac{sin(\frac{r}{2H})}{e^{\frac{z}{2H}} - co(\frac{r}{2H})}. \tag{4.11}$$

The z location of the shock associated with this angle, Θ is:

$$z(r,\Theta) = 2H(Ln\frac{sin\frac{r}{2H} + \Theta}{sin\Theta}). \tag{4.12}$$

One can then trace the entire history of a streamline. First use the current shock location to find the propagation angle, then for any r from $r = 0$ to the current r location, the z location for that r can be determined by equation 4.5. A plot of a superbubble streamlines and the superbubble's shock front at multiple epochs can be seen in Figure 4.2.1.

4.1.2 Hydro-Limit Shell Thickness

Since we have assumed the superbubble's shock remains a strong one, we can use the jump shock conditions to find the density of the shell if we know the magnitude of the velocity at the shock and the upwind density. To find the shell thickness Basu et al. (1999) find the expected shell surface density and divide this by the shell volume density.

To find the local surface density, N, of the shell we find the mass inside a volume bound by two adjacent (in z) streamlines and the forward shock and divide this by the surface area of the forward bounded by the same streamlines. Since streamlines do not cross, we do not assume for this analysis that the post-shock gas does not cross streamlines either (requires no external velocities.) Mass between two streamlines is then conserved such that any mass swept up by the shock within the described volume must be contained in the portion of the shell also between the two streamlines. This

allows us to find the shell thickness by using the known shell density.

$$\delta r = \frac{N}{\rho_{shell}} \tag{4.13}$$

This method for finding the surface density gives same result as Basu et al. (1999) (see Figure 4 in their paper and compare with Figure 4.2.1).

Considering the spherical expansion into a uniform medium, equation 4.13 would give a uniform shell thickness for every location, and the streamlines would follow radial paths. The stratified distribution of the ISM not only changes the density profile through which a streamline would traverse, but the path of the streamlines themselves are affected by the gas distribution. This difference makes the later stages of evolution well beyond something that could be approximated with spherical expansion necessary to understand. Additionally, if the shell is strongly cooled, then we should expect to see a much thinner shell in the hydro limit, depending on the Mach number of the shock, just as with the spherical case.

Figure 4.2.1 shows a two-dimensional cut of the location of the forward shock and contact discontinuity for a high luminosity superbubble at three different epochs. Due to the slowing of the expansion speed, the shell thickness in the mid-plane expands with age. However, because of the decrease in density in the z direction, the expansion speed in this direction is increasing as the superbubble ages (this is beginning of 'blowout' or the escape of the top, and bottom for a superbubble centered in the mid-plane of the galaxy.) The increase in expansion speed results in a higher compression ratio and thinner shell near the top and bottom of the bubble.

4.1.3 Evolution

4.1.4 Comparison with Spherical Expansion

For young superbubbles the Kompaneet's approximation should match the properties of a superbubble expanding into a uniform atmosphere. To verify the results of our semi-analytical description we compare our results to the 'spherical' case for shell location, density and shell thickness.

Figure 4.2.1 shows a comparison of the analytical development of a spherical wind blown bubble with the Kompaneet's approximation superbubble in the plane (z = 0).

One can see the good agreement for the location of shock front for the spherical (Weaver et al. (1977)) case and for the Kompaneet's approximation in the plane through almost 5 million years. Shell thickness in the large beta limit can be seen in plot b) of the same figure. As the superbubble ages we see greater disparity between the two cases, particularly after 2 to 3 million years. As streamlines should be expected to converge towards the plane, unlike in the spherical case, as the superbubble ages an increase in shell thickness over the spherical case is possible. Shell density is also shown in the same figure in plot c). In both cases the shell density is found from the jump shock conditions for an isothermal shock. Near the plane the density gradient is not effective in producing a large change in the shock velocity, so it should not be expected to vary much from the spherical expansion case. Plot c demonstrates this in that there is little to no difference in the shocked gas (shell) density between the two cases.

4.1.5 Expected Deviation from Kompaneet's Approximation

First, we verify that we can reproduce the solution to a Kompaneet's superbubble analytically. Basu et al. (1999) show log plots (see Fig. 10 in Basu et al. (1999)) of dimensionless variables versus time to demonstrate the deviation from the solution for a uniform atmosphere made by their modified solution to the Kompaneet's approximation. Plots for y, E_{thm}, and P versus time are reproduced in Figure 4.2.1 to show agreement.

Galactic gas distribution in the Milky Way is not an exponential profile. As already discussed in section 2.2.2 Dickey & Lockman (1990) show that atomic gas distribution in the Milky Way is the result of two Gaussians and an exponential. Though the Kompaneet's approximation for a exponential distribution of gas is a reasonable starting point for understanding how a superbubble might evolve as it grows larger than the scale height of the gas, it will not fully describe the evolution of a superbubble in a more realistic gas distribution. We consider how the atmospheric setup of our simulations might affect the forward shock locations, and how this might differ from the solution to Kompaneet's approximation. For this exercise we center the superbubble in the plane.

The atmosphere in our simulations is more concentrated in the plane than an exponential distribution with a scale height equivalent to the effective scale height of the DL90 gas profile. The gas distribution used in our simulations has more gas at altitudes less than a scale height but less gas at higher altitudes than the exponential atmosphere.

What might this mean for evolution? Olano (2009) found the evolution of a point-source explosion using the assumptions of Kompaneet's approximation for a gas distribution of $sech^2(z/H)$. This distribution is very similar to the DL90 distribution for altitudes below a little more than a scale height, but less dense than DL90 above this. [4] Olano found that the $sech^2(z/H)$ atmosphere produced a less 'pinched' bubble than the exponential atmosphere, with the cylindrical radius shrinking or at most remaining constant with altitude z. This is certainly different than the exponential gas distribution which showed an increase in cylindrical radius with altitude once the bubble had grown beyond a scale height in size. The increased density at low altitudes therefore prevents the superbubble from developing a 'peanut' shape. Olano also finds that the hyperbolic secant atmosphere "blows out" for smaller y than the exponential atmosphere. Even without modeling blowout this is a useful aspect of our gas distribution since it will mean the superbubble grows perpendicularly to the plane (after it is larger than a scale height in size) more quickly than for an exponential atmosphere.

We also wish to understand how the shell thickness and shell density might deviate from Kompaneet's approximation for our simulations. The shell thickness is a direct result of the conservation of mass in the shell, all mass swept up by the shock remains in the shell. If the gas density in the shell is very high, the shell thickness is very small. The strength of the shock determines the shell density. For strong shocks with large Mach numbers we expect the shell to remain thin, particularly if there is cooling. In an exponential atmosphere the temperature does not change with altitude, however the temperature in our atmosphere increases with altitude. The increase in temperature means an increase in the sound speed of the gas and therefore a smaller Mach number as the superbubble shell rises, even if the shell velocity didn't decrease with time. We expect the shell to be thicker than predicted in §4.1.2 and the shell density to be lower. Though we simulate a warm plasma, where the sound speed is larger than the Alfvén speed, this result should also hold for cold plasmas with negligible thermal pressure since the density decrease with altitude results in an increasing Alfvén speed.

[4] With slightly different values for H, the hyperbolic secant and exponential atmospheres can be made to have the same values for density at the location of the exponential atmosphere's scale height. With this change the DL90 and hyperbolic secant atmospheres show nearly identical behavior for values for altitudes less than an exponential atmosphere's scale height.

Another very important difference for our simulations from the Kompaneet's approximation is the inclusion of the magnetic field. As seen in §3.2 when cooling is strong enough the magnetic pressure may grow larger than the thermal pressure for select locations in the shell. In these locations (regions where the ambient field had a large enough component tangential to the shock) the shell thickness is larger than predicted by the unmagnetized case. At the 'top' and 'bottom' of the bubble, where the ambient field lies most tangentially to the shock front the increase in shell thickness can be quite large. Since the Kompaneet's approximation predicts a very thin shell here the difference between it and our simulations should be very noticeable.

4.1.6 Evolution of the Magnetic Field

We need to know the geometry of the magnetic field in the shell for our synthetic polarization observations. However, including the dynamical effects of the field in our analysis would greatly complicate things. For our analysis we ignore the dynamical feedback of the field and consider the case where the magnetic field represents a small portion of the energy density in the gas. Under these conditions (and the frozen-in field condition) the magnetic field will follow the gas. Ferriere et al. (1991) showed that the field in the shell of a constant luminosity bubble could be found from the jump shock conditions. This was used in the previous section to describe a superbubble with a radius still less than the scale height of the gas.

Using the jump shock conditions to find the average field in the shell will not work for the case of a superbubble following the Kompaneet's approximation. The problem is seen in the difference in 'streamline' evolution between the spherical and Kompaneet's cases. As already mentioned, the spherical case maintains velocity vectors that do not change direction throughout the development of the bubble, so the 'streamlines' are straight lines. In the Kompaneet's case, the velocity vectors change direction in time, and so the 'streamlines' are not straight lines. In terms of the evolution of the magnetic field in the shell, this means that for the shock front in the spherical case each element of the shock front will always produce the same post-shock tangential and perpendicular components through the bubbles development. However, the same can not be said for the Kompaneet's case, and so it cannot be assumed that average post-shock field lines will be described by any one moment's jump shock conditions since this could ignore

past field evolution.

Fundamentally this is an issue with using the Rankine-Hugoniot jump shock conditions when the assumptions used in determining these conditions have been violated. The jump shock conditions assume a steady state with a constant shock velocity and direction. If the Mach number remains large and the direction of the shock propagation doesn't change then the steady state approximation works well. As the shock speed slows or the direction of the shock propagation changes then the steady state assumption breaks down. This makes the jump shock conditions unsuitable for determining the post-shock behavior of the gas in the superbubble shell.

Without an analytical method of determining the shell field orientation we are left to rely on numerical methods to solve the full ideal MHD equations to determine shell properties. However, we would like to first investigate a naive model for the superbubble's magnetic field orientation in the shell.

4.2 Toy Model Breakthrough Superbubble Effect on Polarization

As in section 3.3, we first try something very simple to determine the plausibility of detecting a change in polarization. Assuming we know the geometry of the magnetic field in the $\hat{x}$- $\hat{z}$ plane we can extend this field geometry (and the density) through the entirety of the path that intersects the shell. Similar to what we did in section 3.3, we can define a Δx that is the longest path through the shell at a given z and a D, the length of the total foreground and background included. Using r from equation 4.5 we can once again find Δx using $\Delta x = \sqrt{\Delta r(2r - \Delta r)}$. We can also find an I, Q and U through the shell for parallel lines of sight through any given z using the same equations already given in that section. (See equations 3.18, 3.19 and 3.20.)

This method is an optimistic oversimplification. In reality the field in the $\hat{x}$- $\hat{z}$ plane would not be oriented identically to the field in front and behind this plane in the shell. We expect that the magnetic field lines should rotate towards and away from us outside of this plane and reduce the contribution to the measurement of polarized intensity of the dust grains there compared to the grains in the plane. However, since our oversimplification increases the likelihood of detecting the change a superbubble

could have on polarization measurements, if a change is not detectable in this test, it is very unlikely to be so in a more realistic model.

To produce the field geometry in the $\hat{x}$- $\hat{z}$ plane we assume a toy model for the post-shock magnetic field. We know that the geometry of the field predicted from the jump-shock conditions is not a good representation of the field orientation in the shell. Also, we know that the magnetic field components tangential to the shock are amplified, while the normal components are left unchanged. The most extreme limit from this is that the average field geometry in the shell would lie entirely tangential to the shock. [5] The purpose of this toy model is to qualitatively match the idea that vertical components of the magnetic field are created by breakthrough superbubbles, not to propose a rigorous theory of post-shock evolution of the magnetic field.

Once again we created 'maps' of the polarized "emission" in the shell. These figures compare different lines of sight through the shell of a superbubble with a luminosity of $3x10^{39} ergss^{-1}$ at a simulated time of $5x10^6$, $11x10^6$ and $19x10^6$ years. These times correspond to just after the bubble reaches a radius comparable to the effective scale height of the gas through to just before 'blowout' (where blowout is expected to occur when $y = 2H$). For the ambient medium there would only be horizontal polarization, any deviation from this is the result of the superbubble.

In figure 4.2.1 we compare the difference in polarization between a strongly cooled isothermal shock and an adiabatic one in the shell of a Kompaneet's like superbubble. [6] In §3.3 we found that the effect of strong cooling (isothermal shock) on polarization was lessened as the superbubble aged, likely due to the decrease in Mach number and hence compression factor and shell density. This trend is continued as the superbubbles grows beyond the spherical case. In 4.2.1 it is clear that even with a very large luminosity

[5] Or put another way that the tangential components are much larger than the normal components of the magnetic field such that the normal components are negligible as would be the case for a steady shock with strong cooling and a high Mach number. However, this is not identical to what we are assuming here since locations in the shell with a shock normal parallel to the ambient field are still given a shell field orientation tangential to the shock in our toy model. It is assumed that this fluid element would have created large tangential components earlier in the superbubble's evolution and that these components do not change orientation in the time between when they were produced by the shock and the present time of the model.

[6] This analysis glosses over an aspect of cooling the shell of the superbubble that is important. By cooling the superbubble shell, energy is removed from the system. This was not accounted for in our energy budget used to determine the shock speed (see equation 4.8.) A cooled superbubble should be smaller than what we predict here.

($L = 3x10^{39} ergss^{-1}$) the superbubble shell is not producing significant differences in polarization for a cooled shell as it ages. However, the polarization produced by a superbubble that extends out of the plane, differs greatly from the polarization that would exist in the ambient ISM, strongly cooled or not.

How might foreground and background additions to the path affect this? From Figure 4.2.1 we see that adding this foreground and background greatly decreases the effect the superbubble has on the observed polarization in the shell. As might be expected, the superbubble's vertical polarization signature is reduced by the foreground and background components. Interestingly, for the oldest superbubble time plotted (plot (c)), the polarization produced by the superbubble is not as affected by the foreground and background contributions. Though non-parallel lines of sight are necessary to define the problem more accurately, it seems that the superbubble has grown beyond the height for which foreground and background components have a significant effect on the observed polarization. Clearly, the superbubble is affecting observed polarization for the very optimistic and simplistic method of determining polarization used.

As with the spherical case we extend our toy model of a breakthrough superbubble to three dimensions. Though the location of the shell, its thickness and density are simply azimuthal rotations of the 2D case about the z-axis. Without an analytical description of the evolution of the post-shock gas, we are left to guess about the orientation of the field there. In the 2D case we assumed that the field would be tangential to the shock surface, this being the most favorable orientation for our synthetic observations. To extend this toy model to three dimensions we need some way of defining the field beyond the $\hat{x}$- $\hat{z}$ plane. The simplest arrangement that would reduce to the spherical case (under the constraint that the shock is sufficiently cooled and strong enough that the post shock field lies predominately tangential to the shock) is to project a magnetic field fully tangential to a spherical superbubble shock onto the Kompaneet's shock front.

This toy field configuration is found in the following way. The spherical shock normal is given in Cartesian coordinates by the x, y and z locations normalized by the radius of the sphere ($r = \sqrt{x^2 + y^2 + z^2}$) $\hat{n_{spherical}} = \frac{x}{r}\hat{x} + \frac{y}{r}\hat{y} + \frac{z}{r}\hat{z}$. This vector is then used to find the component of the ambient magnetic field that lies tangential to the spherical shock surface ($B0t_{sphere}$) using equation 3.16. To find what component of $B0t_{sphere}$ is tangential to the Kompaneet's shock surface we once again use equation 3.16 but with

a normalized $B0t_{sphere}$ as the full magnetic field vector $B0$ and with the shock normal, $\hat{n}$ defined as the Kompaneet's shock surface normal.

The plausibility of this toy model for the post-shock magnetic field configuration is explored in Chapter 5 when we discuss our numerical simulations of superbubbles.

4.2.1 3D Semi-Analytical Superbubble Polarization

Using GRIZZLYEYE we create synthetic images of our Kompaneet's-like superbubble with our toy model magnetic field orientation in the shell. We create images of superbubbles using two types of environments, an exponential atmosphere and an atmosphere with a DL90 gas distribution. [7] Before discussing how a breakthrough superbubble might produce detectable polarization changes we first examine how a different atmosphere might affect our semi-analytical synthetic observations. This is potentially useful since we would like to compare our maps of simulations using a DL90 atmosphere to the maps we create here using our semi-analytical superbubble.

We compare maps of polarized dust emission made of a superbubble 1kpc distant in an exponential atmosphere and compare this to a superbubble also 1kpc distant in a DL90 atmosphere. We orient the superbubbles such that our line of sight lies perpendicular to the ambient magnetic field. To resolve the shell for a superbubble aged 2.8 million[8] years located 1 kpc from us should require a resolution of about $10arcmin$. Since our polarization vectors will have a poorer resolution than our intensity images, we use a resolution of $4arcmin$. These two maps are found in Figures 4.8 and 4.11. Comparing these maps we see that the shell is much thicker for the DL90 atmosphere (Fig. 4.9) than for the exponential distribution. Since both models and images used the same assumptions to construct a magnetic field orientation we do not expect, nor see, any difference in the orientation of the polarization. The effect of using the DL90 atmosphere for the analytical models instead of an exponential one is that

[7] For clarification a few things should be mentioned. First, even for images of just the superbubble, the environment plays a key role in determining shell properties since it is the upwind properties that are used in the RK jump-shock conditions. Secondly, though the Kompaneet's approximation assumes an exponential atmosphere, we model a Kompaneet's-like superbubble in an atmosphere that is not an exponential distribution of gas. We do not solve for a new evolution using the same method as the Kompaneet's approximation for the DL90 atmosphere, we only use its density profile for the upwind parameters.

[8] This age is chosen in order to compare to our numerical results from Chapter 5.

our models create larger areas (across the shell) of polarization differently oriented from the polarization created by the surrounding material.

We create synthetic images of a strongly cooled superbubble aged 2.8 Myr [9] in a DL90 atmosphere for dust emission polarization at $100\mu m$ and $2.2\mu m$ starlight transmitted through dust. First, maps of only polarization created by the superbubble were produced for lines of sight parallel to the unperturbed magnetic field and perpendicular to it. Then we created synthetic maps of superbubbles embedded in our galaxy and included galactic contributions to the polarization.

Figures 4.9 and 4.10 show the superbubble in polarized dust emission without galactic contributions. From these figures we can see that the superbubble clearly creates horizontal polarization vectors (therefore vertical magnetic field), though like in the spherical case, the most dramatic region for this change is near the apparent center of the superbubble when the line of sight is parallel to the magnetic field (Fig. 4.10).

Also, very interesting is that when looking perpendicular to the magnetic field lines we do not see purely horizontal polarization in the shell, though the polarization there is significantly horizontal. The path through the shell does not include purely vertical magnetic field, since we modeled it like the spherical case field configuration. However, we do not have a true analytical description of the magnetic field lines in the shell so this result will require numerical modeling to compare to.

Adding dust emission foregrounds and backgrounds to our simulated superbubble does not reduce detectability of superbubble polarization as much as in the spherical case, which can be seen from Figures 4.11 and 4.12. There are three likely reasons for why the superbubble polarization is still evident even with galactic contributions, none of them mutually exclusive. First, the magnetic field orientation in the shell may be an optimistic configuration, numerical modeling will help to determine if a breakthrough superbubble can produce magnetic fields with such strong vertical components. Second and third, the superbubble, because of its larger size than the earlier spherical case, has swept up more mass into its shell and extended that shell beyond the scale height of the disk. In short, a breakthrough superbubble produces detectable polarization change

[9] This is enough time for a superbubble to grow larger than the ~ 350 pc effective scale height of the gas assuming a Kompaneet's-like evolution from a constant luminosity of $\sim 3 \times 10^{39} ergs s^{-1}$. However, as mentioned in an earlier footnote, cooling of the shell should reduce the total available energy of the system and produce smaller superbubble than expected from the adiabatic case.

because locations with vertical field components have more dust in the shell and this dust is located along a line of sight that passes out of the plane of the galaxy.

We also created synthetic images of our breakthrough semi-analytical superbubble in polarized transmitted starlight. As already mentioned, we model unpolarized starlight from a wall of stars just behind the superbubble passing through the dust of the superbubble shell. Figures 4.13 and 4.14 show the superbubble in polarized transmitted starlight without galactic contributions to the polarization. From these maps we see that, just as with polarized dust emission, vertical magnetic fields are created by the bubble (polarization vectors lie parallel to the magnetic field). Also mirroring the dust emission case is that there are no purely vertical polarization vectors.

Figures 4.15 and 4.16 show galactic foreground added to these maps of a breakthrough superbubble. Like with the spherical case, it is not immediately obvious that the polarization produced by the superbubble has changed the net polarization observation. To investigate this we produce images of the same two regions of the sky but without the superbubble (see Figs. 4.17 and 4.18). Comparing Figures 4.18 and 4.16 we see that the superbubble increased the net polarization in this region of sky near the center of the superbubble .(This line of sight, lying largely parallel to the magnetic field does not produce much polarization.) However, for the superbubble at galactic coordinates (0,0) (where the magnetic field is perpendicular to the line of sight) shows no affect on net polarization from the superbubble.

The synthetic images in this chapter are encouraging for the plausibility of detecting a breakthrough superbubble. Numerical work is still necessary to determine the likelihood of our assumed and analytical configurations for the superbubble shape, shell thickness and density and most importantly magnetic field orientation. Chapter 5 will discuss our numerical results.

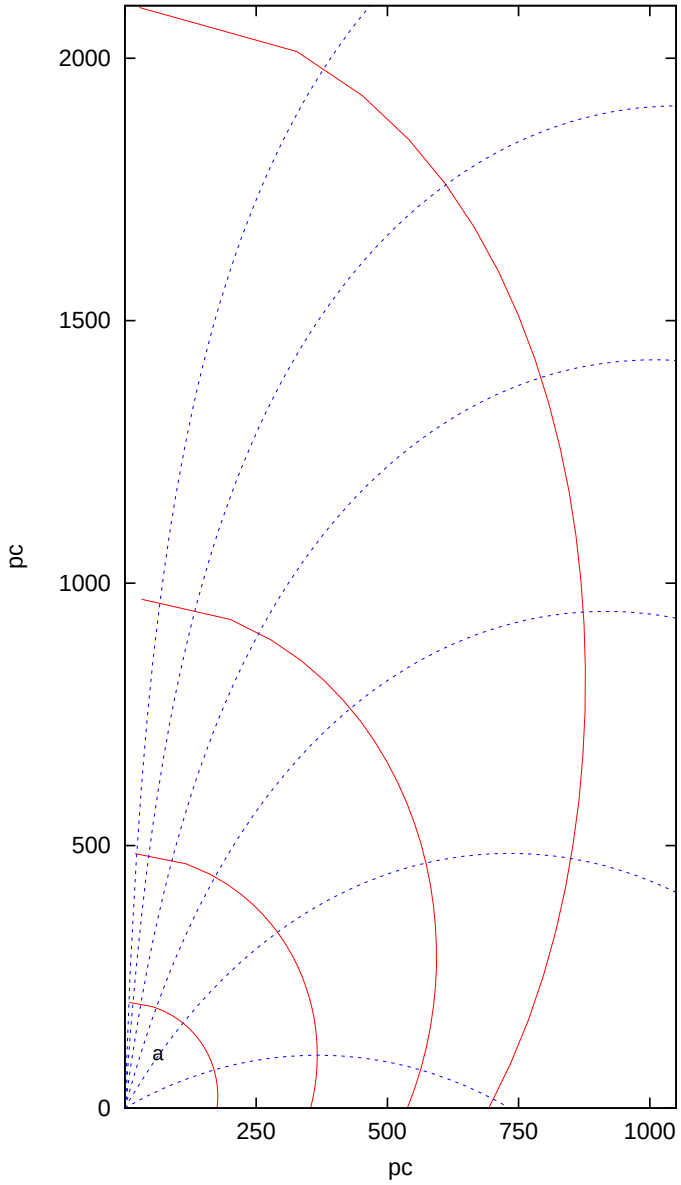

Figure 4.1 Evolution of a superbubble with a luminosity of $3x10^{39} ergs s^{-1}$ with the forward shock front shown at a time of 10^6 years, $5x10^6$ years, $11x10^6$ years and $19x10^6$ years in red (solid). Sample streamlines are shown in blue (dashed).

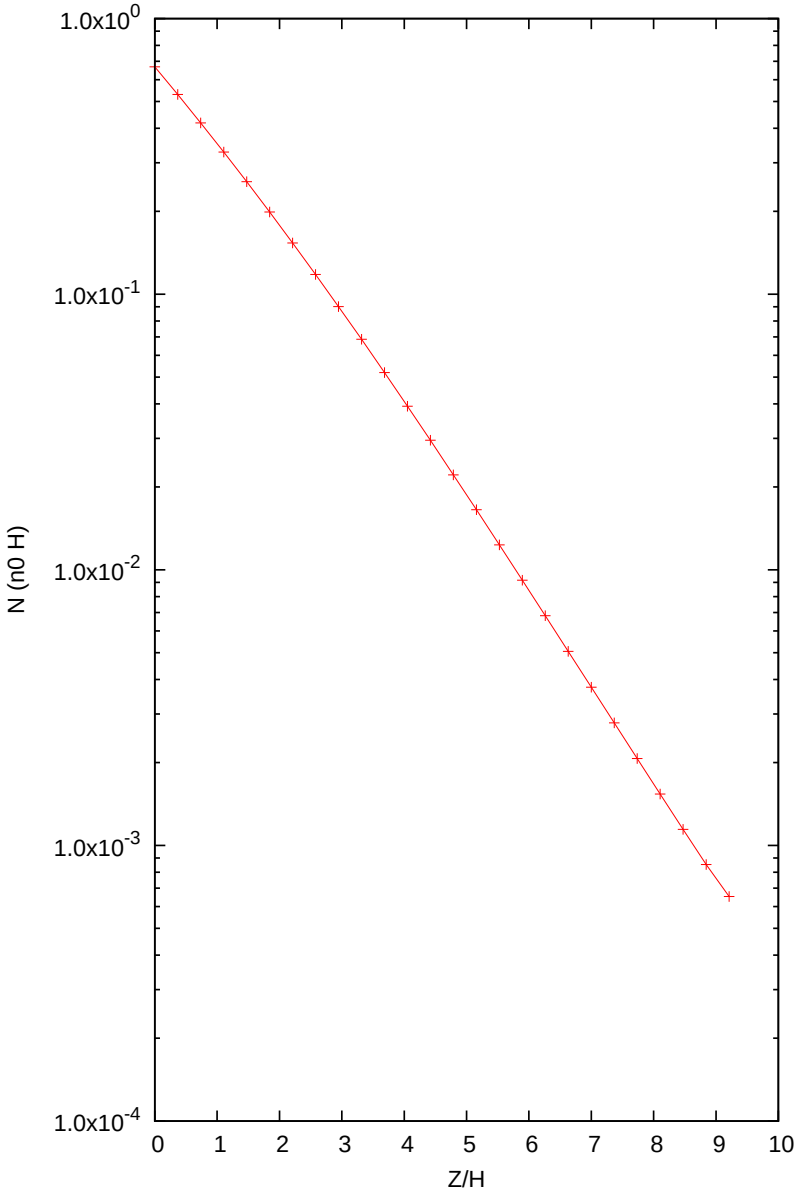

Figure 4.2 Surface density for a superbubble at $y* = 1.98$.

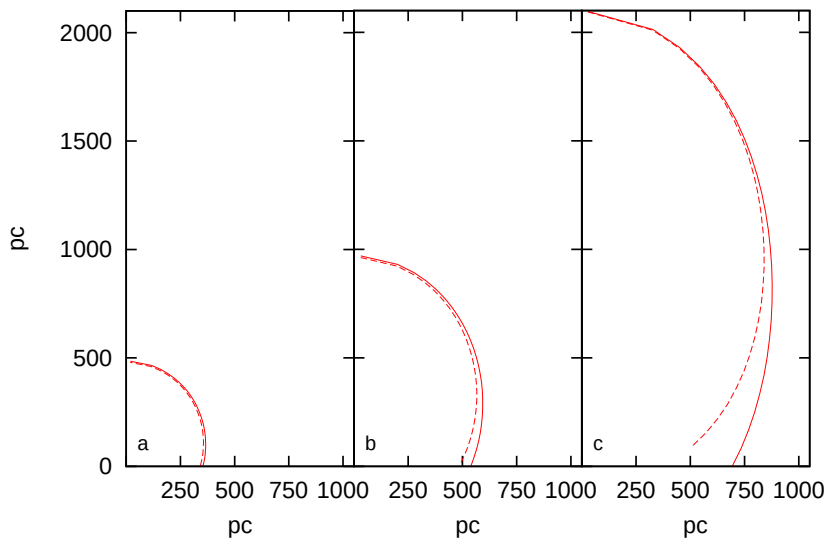

Figure 4.3 Evolution of a superbubble with a luminosity of $3x10^{39} ergs s^{-1}$ at a time of (a) $5x10^6$ years, (b) $11x10^6$ years and (c) $19x10^6$ years. The location of the contact discontinuity is shown in dashed lines.

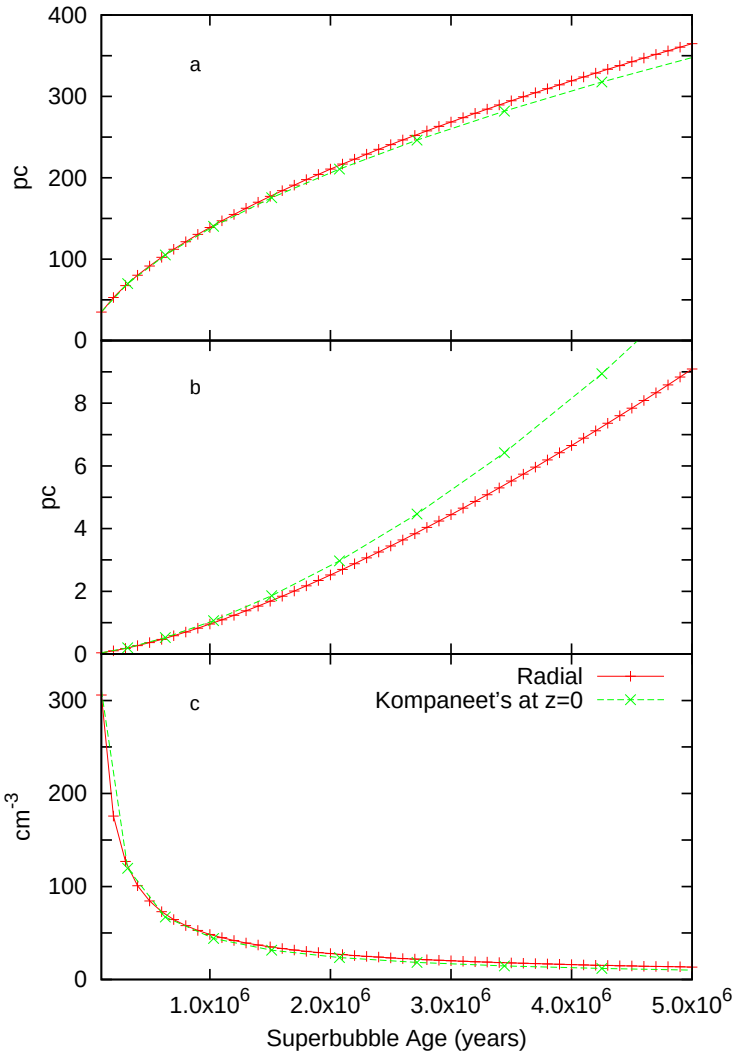

Figure 4.4 Comparison of a superbubble with strong cooling and luminosity of $3x10^{39} ergs s^{-1}$ with spherical expansion and with a Kompaneet's approximation like expansion over a period of $5x10^6$ years. Plot (a) shows the location of the forward shock, (b) the shell thickness at z = 0, (c) shell density.

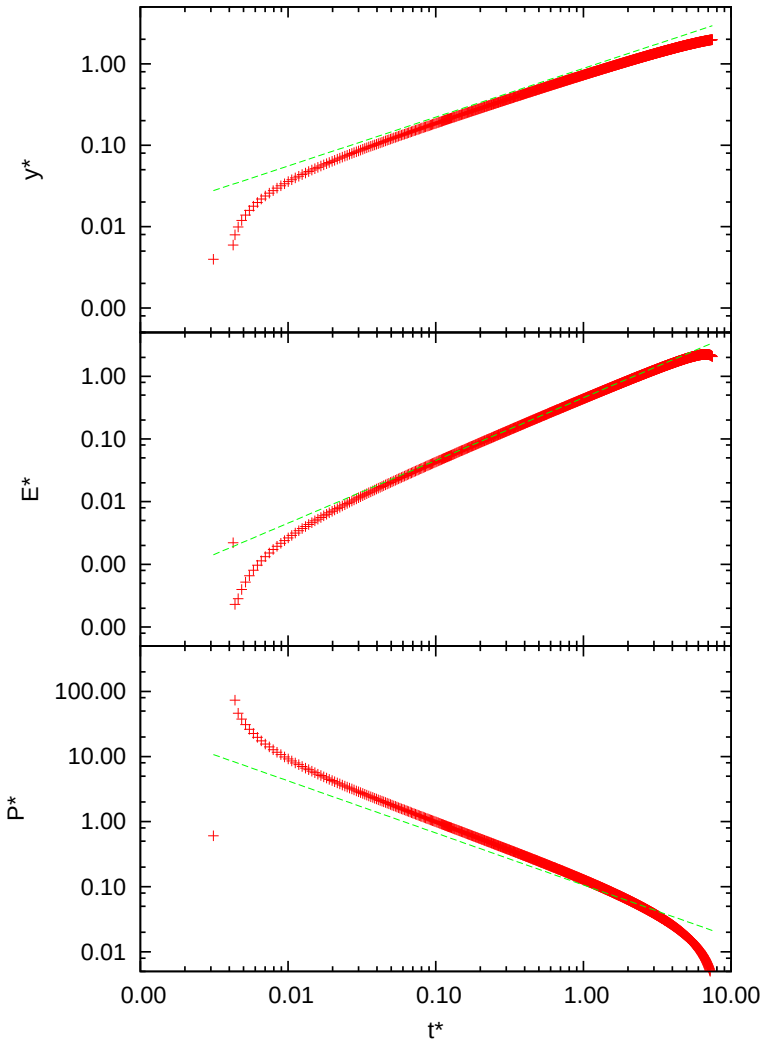

Figure 4.5 Evolution of dimensionless superbubble parameters with dimensionless time. The spherical case (dashed line) is shown for comparison. Early evolution deviates from the spherical case due to finite resolution in both space and time. The evolution of Kompaneet's-like superbubble is identical to the evolution demonstrated in Fig. 10 in Basu et al. (1999).

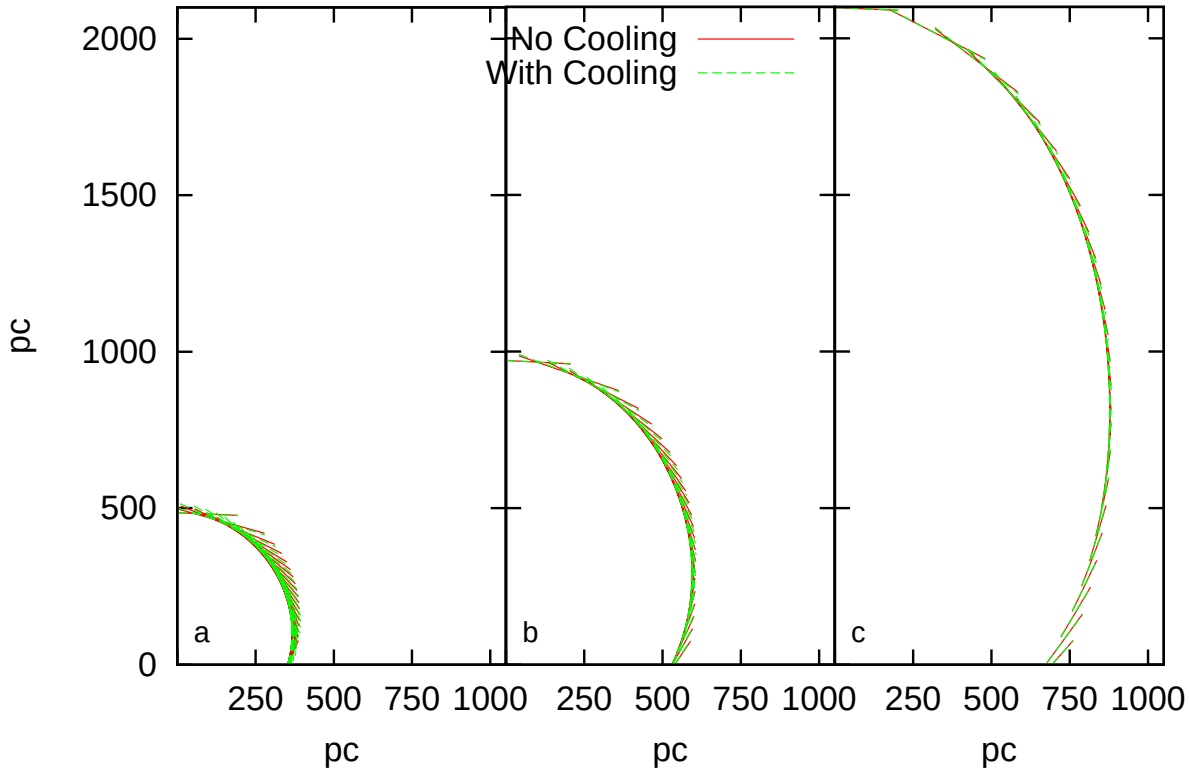

Figure 4.6 Comparison of adiabatic (no cooling) and isothermal (strong cooling) shocks for a superbubble with a luminosity of $3x10^{39} ergss^{-1}$ at a time of (a) $5x10^6$ years, (b) $11x10^6$ years and (c) $19x10^6$ years with no foreground or background.

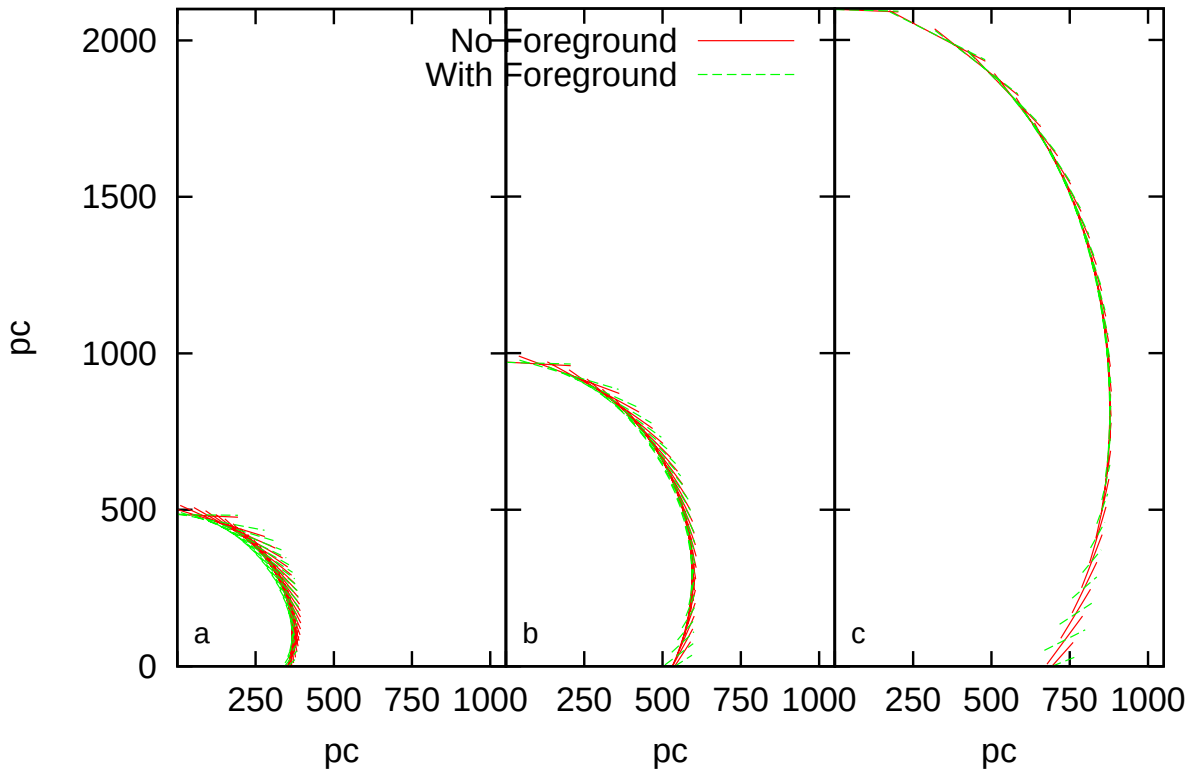

Figure 4.7 Comparison of a superbubble with a luminosity of $3x10^{39} ergss^{-1}$ at a time of (a) $5x10^6$ years, (b) $11x10^6$ years and (c) $19x10^6$ years with foreground and background to one without either.

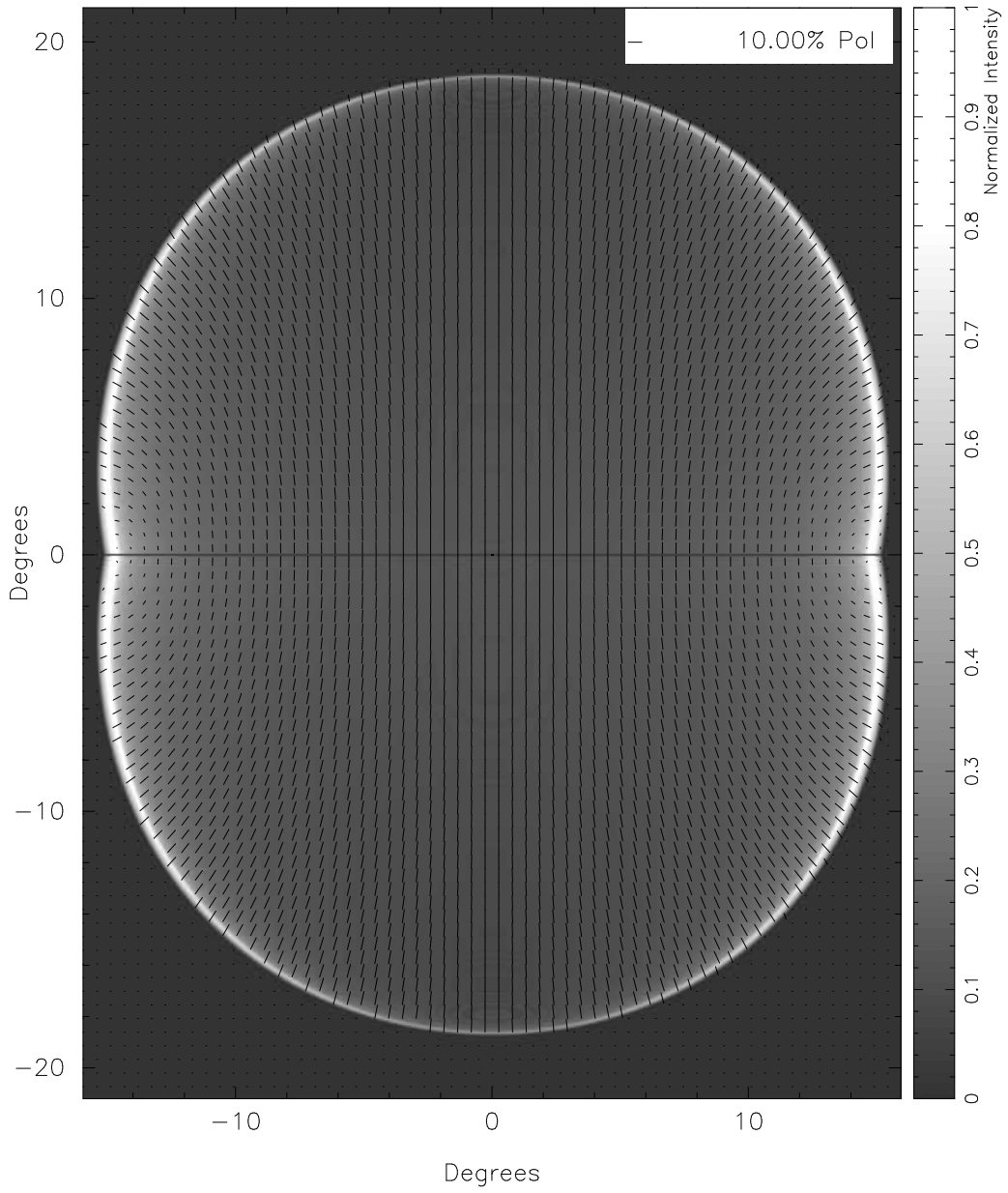

Figure 4.8 Polarization map from 100 micron dust emission from a Kompaneet's -like superbubble in an exponential atmosphere with a line of sight perpendicular to undisturbed magnetic field at 1kpc distance from observers ($(b, l) = (0, 0)$). Foreground and background neglected. Superbubble aged 2.8 Myrs with a luminosity of $3x10^{39} ergs s^{-1}$. Resolution 4 arcmin for intensity, polarization vectors have a resolution of 32 arcmin.

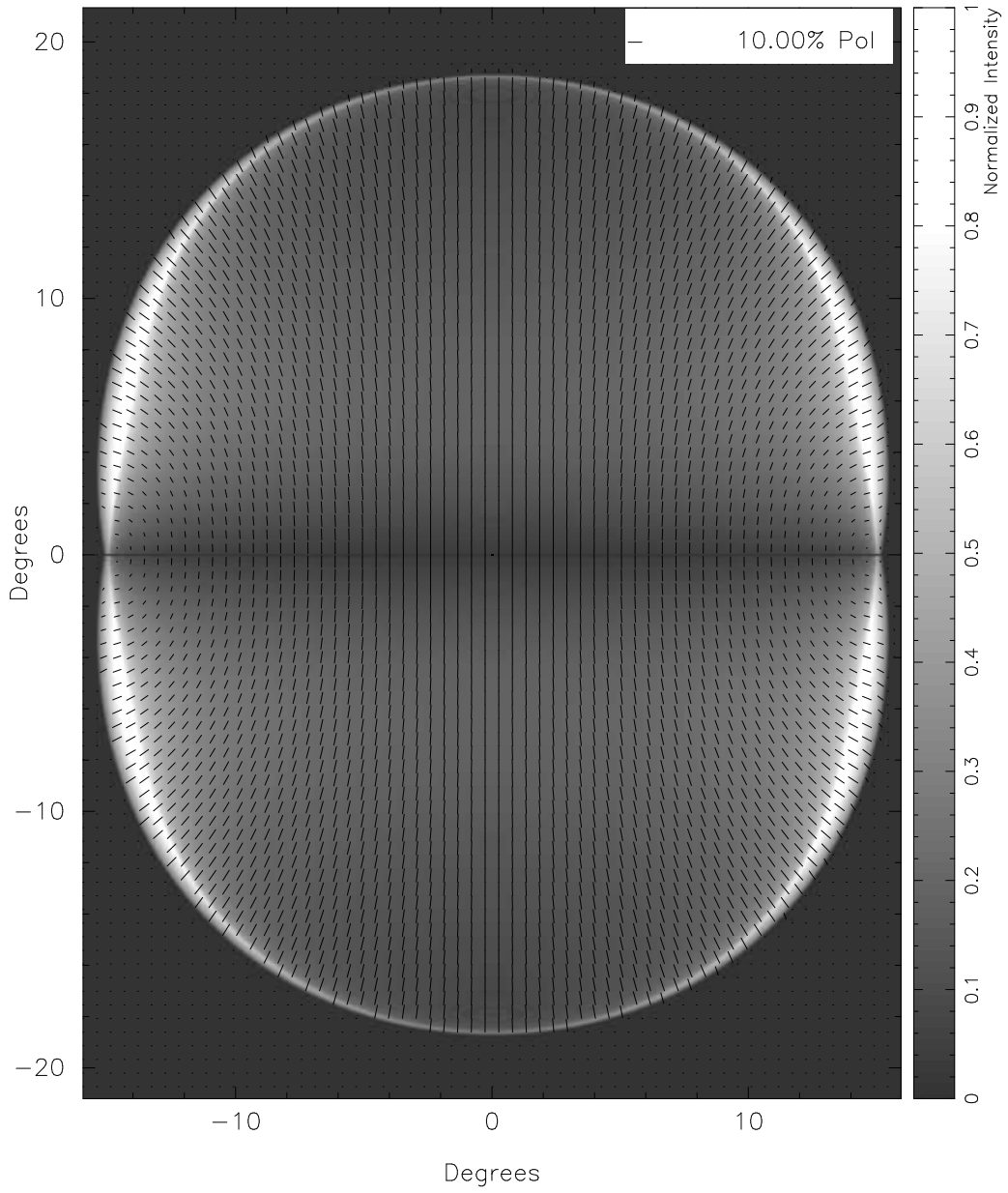

Figure 4.9 Polarization map from 100 micron dust emission from a Kompaneet's -like superbubble in a DL90 atmosphere with a line of sight perpendicular to undisturbed magnetic field at 1kpc distance from observers ($(b, l) = (0, 0)$). Foreground and background neglected. Superbubble aged 2.8 Myrs with a luminosity of $3x10^{39} ergss^{-1}$. Resolution 4 arcmin for intensity, polarization vectors have a resolution of 32 arcmin.

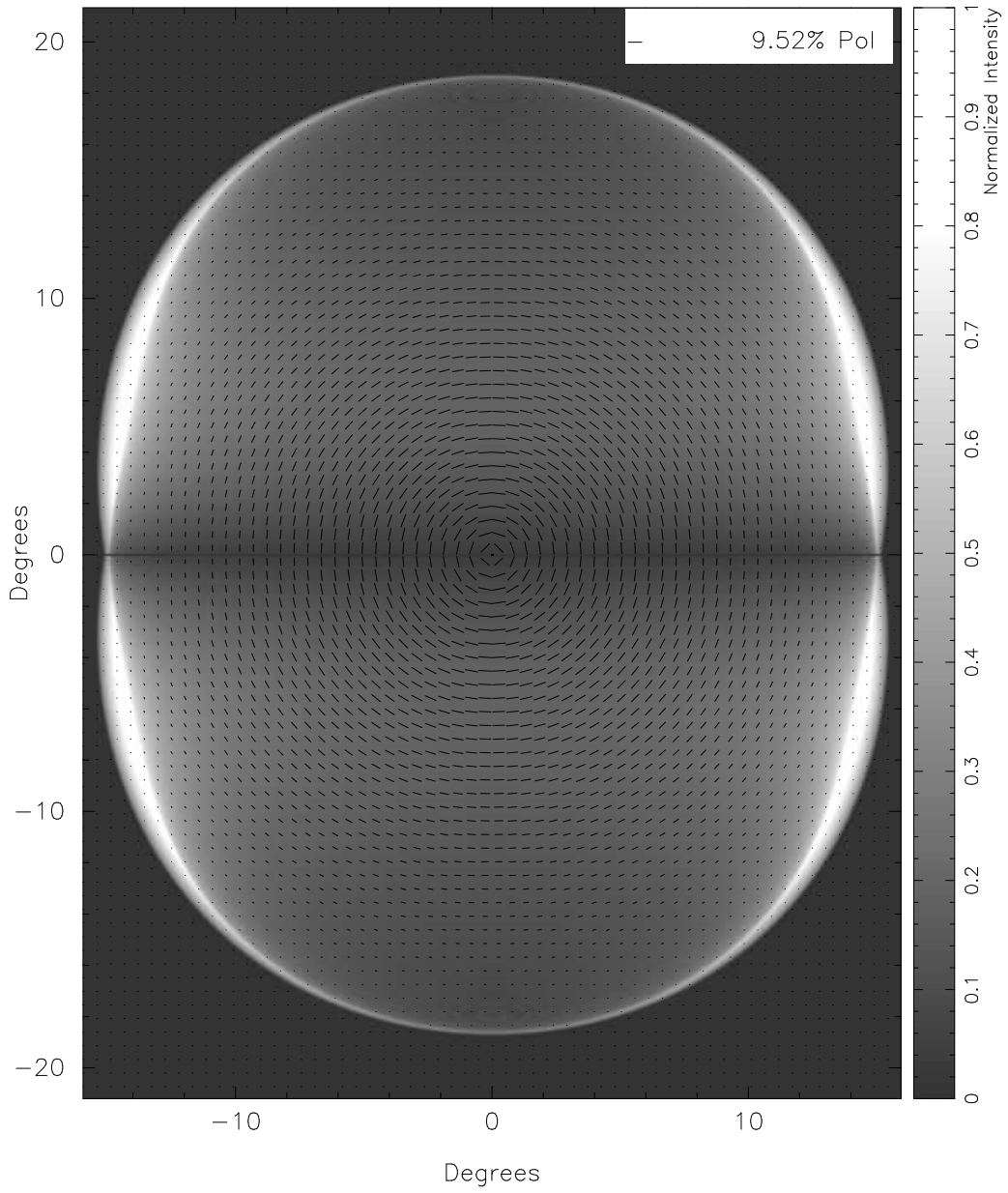

Figure 4.10 Polarization map from 100 micron dust emission from a Kompaneet's -like superbubble in a DL90 atmosphere with a line of sight parallel to undisturbed magnetic field at 1kpc distance from observers ($(b, l) \sim (80, 0)$). Foreground and background neglected. Superbubble aged 2.8 Myrs with a luminosity of $3x10^{39} ergss^{-1}$. Resolution 4 arcmin for intensity, polarization vectors have a resolution of 32 arcmin.

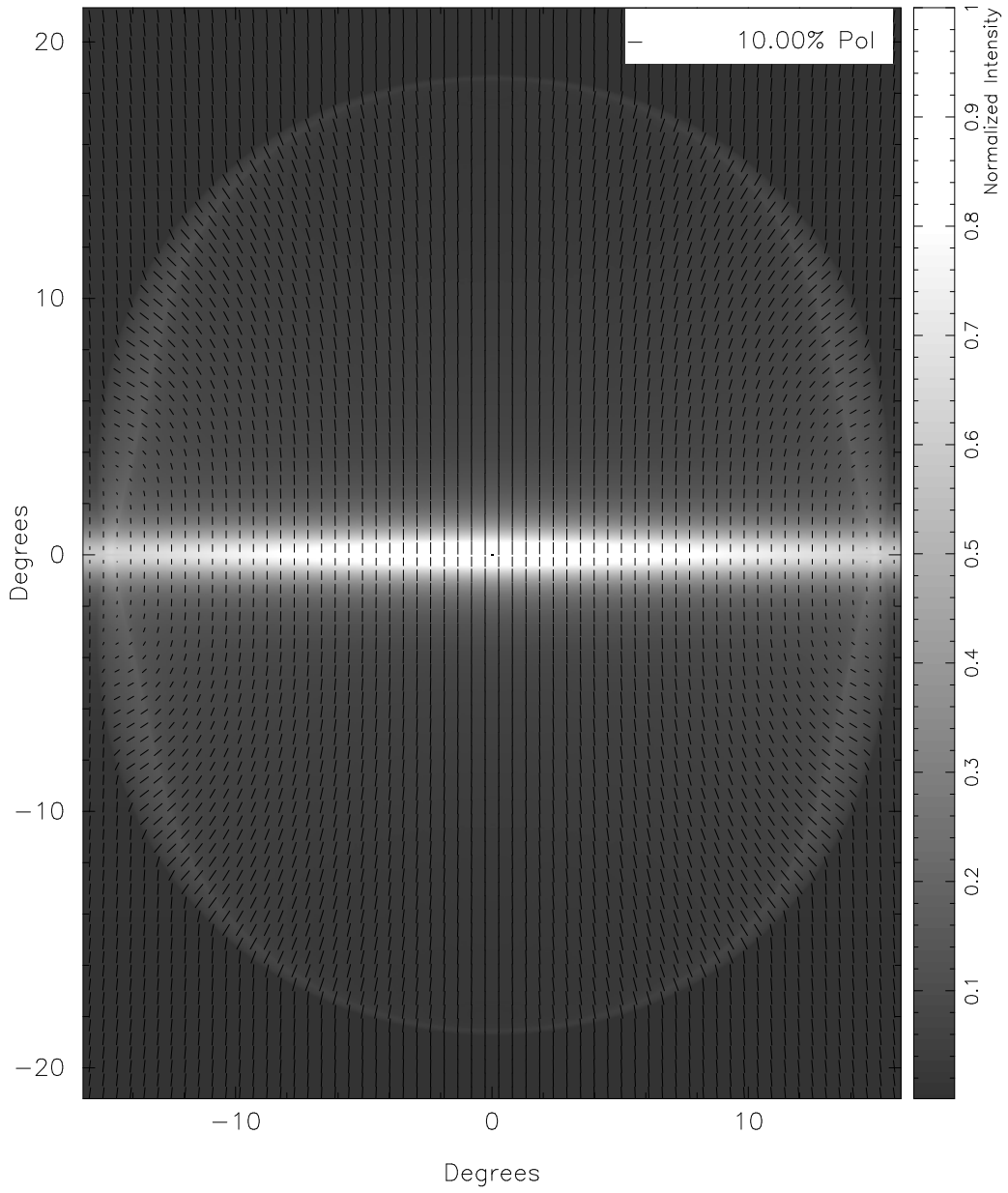

Figure 4.11 Polarization map from 100 micron dust emission from a Kompaneet's -like superbubble in a DL90 atmosphere with a line of sight perpendicular to undisturbed magnetic field at 1kpc distance from observers ($(b, l) = (0, 0)$). Foreground and background included. Superbubble aged 2.8 Myrs with a luminosity of $3x10^{39} ergss^{-1}$. Resolution 4 arcmin for intensity, polarization vectors have a resolution of 32 arcmin.

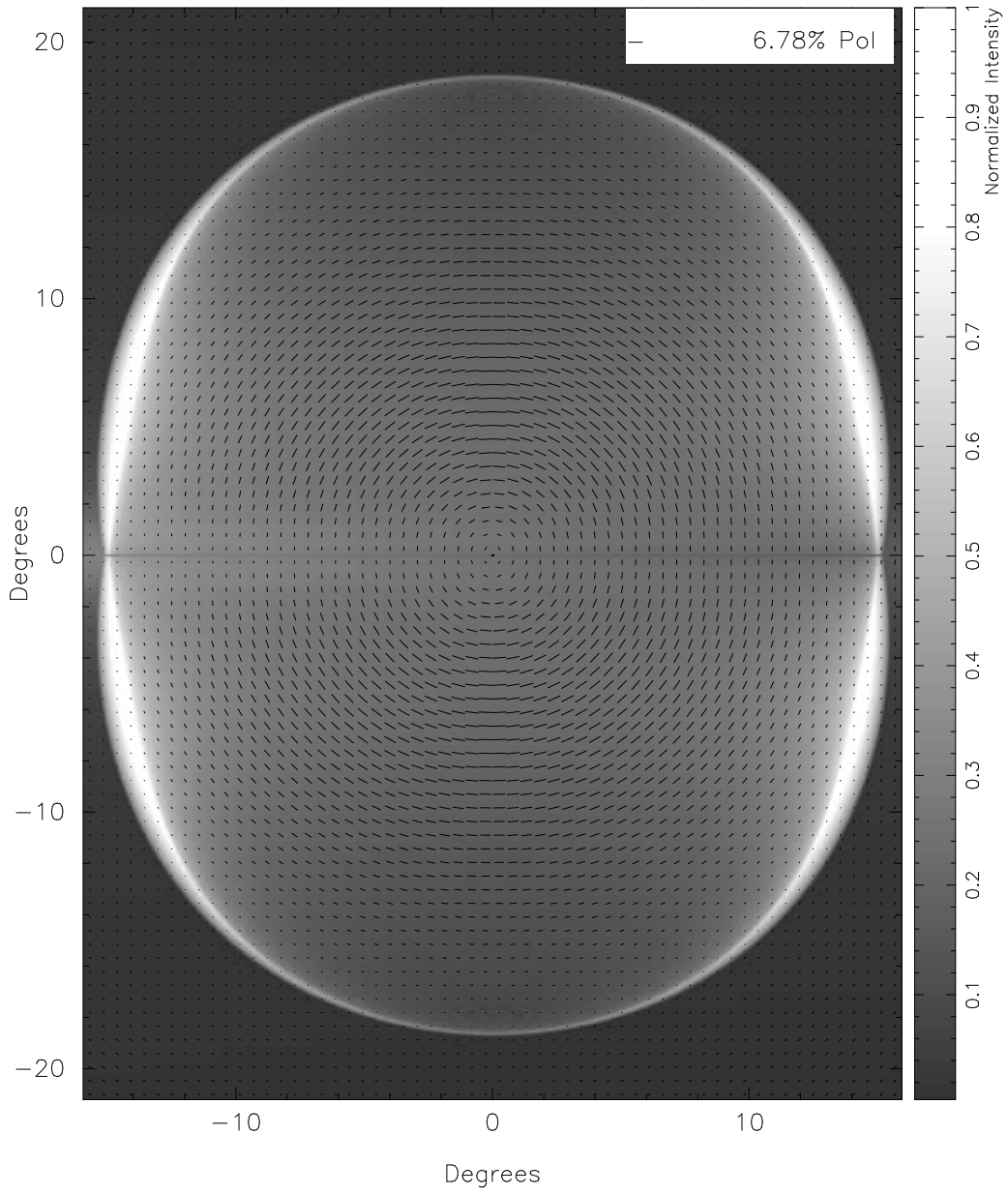

Figure 4.12 Polarization map from 100 micron dust emission from a Kompaneet's -like superbubble in a DL90 atmosphere with a line of sight parallel to undisturbed magnetic field at 1kpc distance from observers ($(b, l) \sim (80, 0)$). Foreground and background included. Superbubble aged 2.8 Myrs with a luminosity of $3x10^{39} ergss^{-1}$. Resolution 4 arcmin for intensity, polarization vectors have a resolution of 32 arcmin.

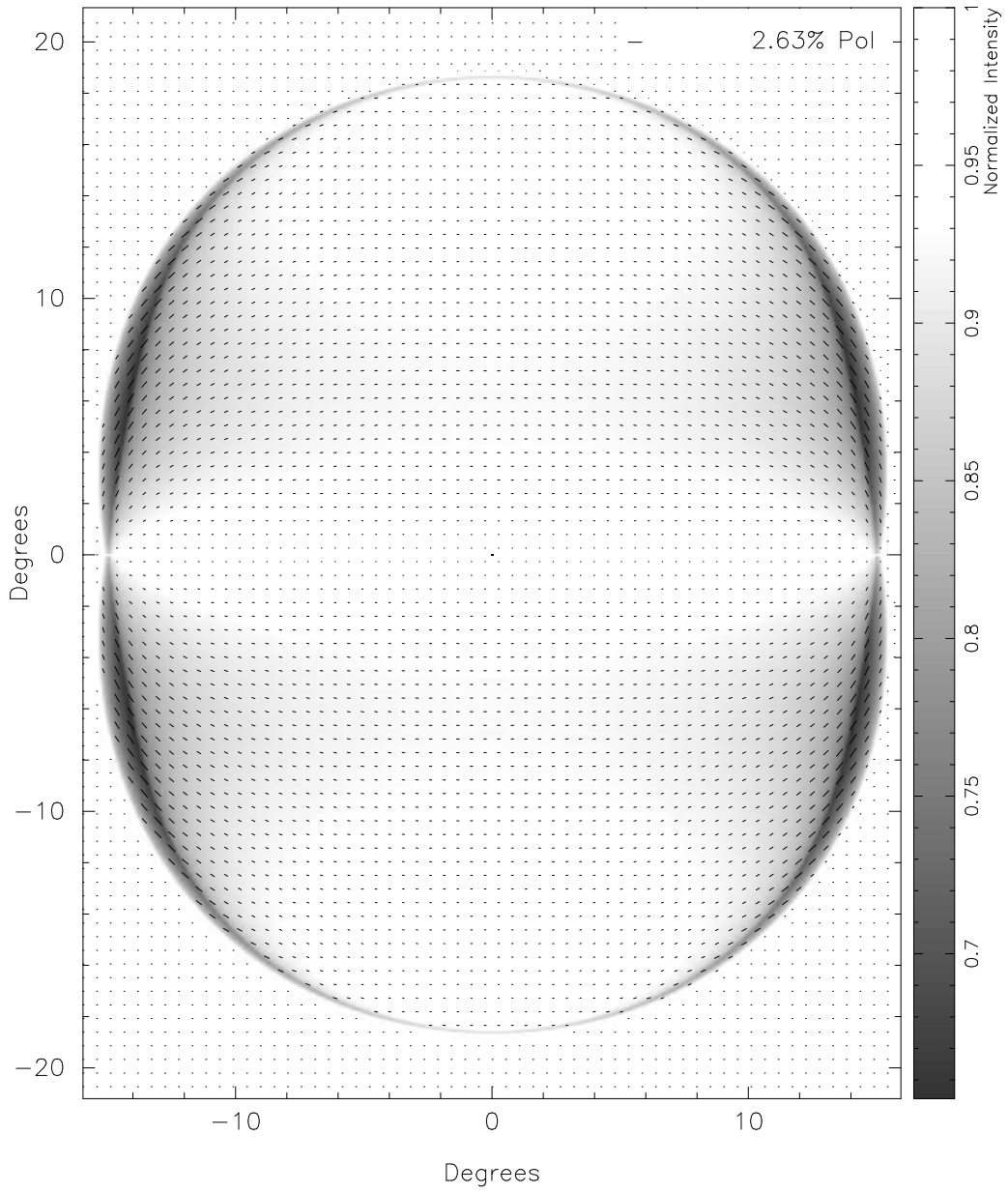

Figure 4.13 Polarization map from 2.2 micron unpolarized starlight passing through a Kompaneet's -like superbubble in a DL90 atmosphere with a line of sight perpendicular to undisturbed magnetic field at 1kpc distance from observers ($(b, l) = (0, 0)$). Foreground neglected. Superbubble aged 2.8 Myrs with a luminosity of $3x10^{39} ergss^{-1}$. Resolution 4 arcmin for intensity, polarization vectors have a resolution of 32 arcmin.

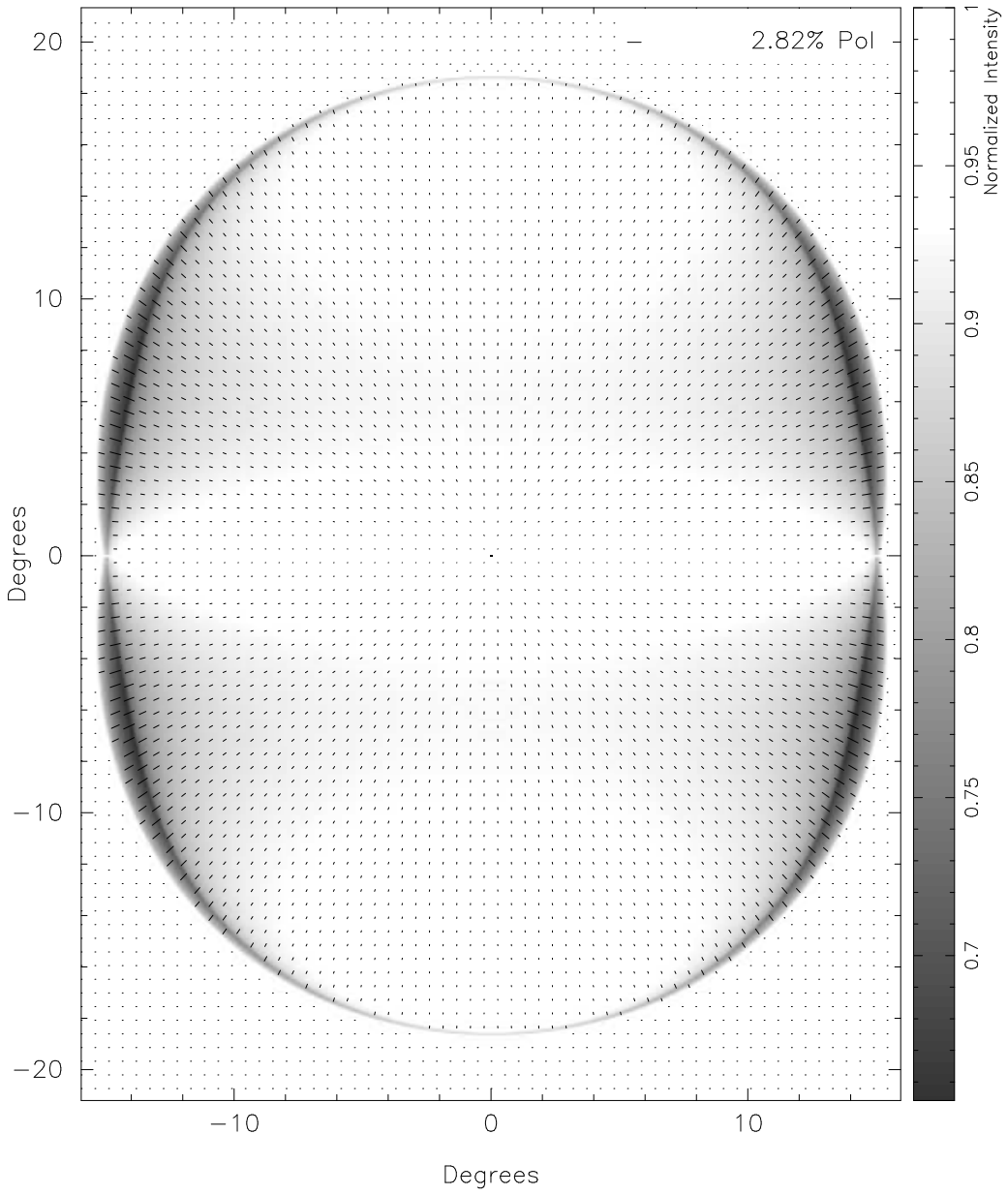

Figure 4.14 Polarization map from 2.2 micron unpolarized starlight passing through a Kompaneet's -like superbubble in a DL90 atmosphere with a line of sight parallel to undisturbed magnetic field at 1kpc distance from observers ($(b, l) \sim (80, 0)$.) Foreground neglected. Superbubble aged 2.8 Myrs with a luminosity of $3x10^{39} ergss^{-1}$. Resolution 4 arcmin for intensity, polarization vectors have a resolution of 32 arcmin.

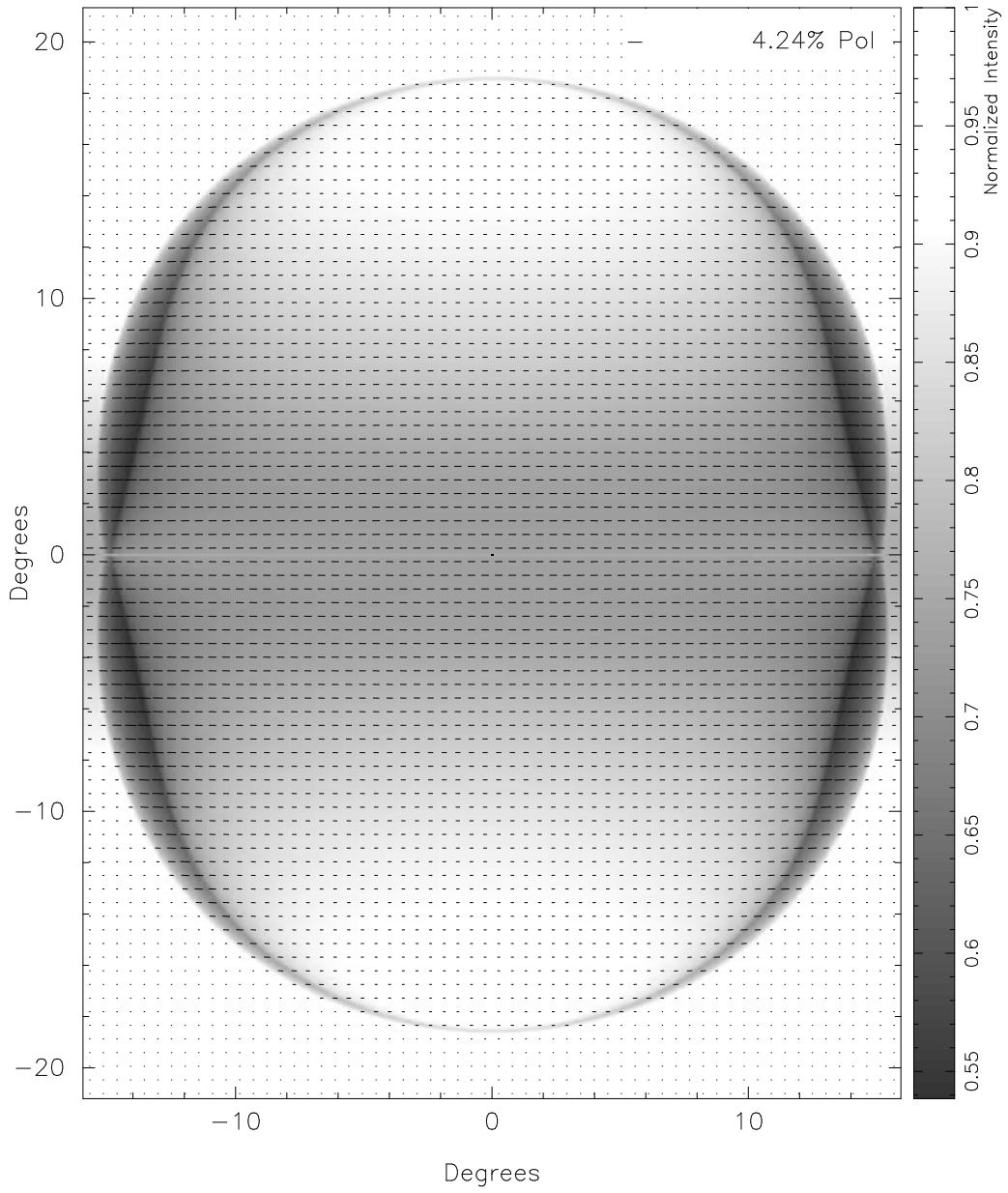

Figure 4.15 Polarization map from 2.2 micron unpolarized starlight passing through a Kompaneet's -like superbubble in a DL90 atmosphere with a line of sight perpendicular to undisturbed magnetic field at 1kpc distance from observers ($(b, l) = (0, 0)$). Foreground included. Superbubble aged 2.8 Myrs with a luminosity of $3x10^{39} ergss^{-1}$. Resolution 4 arcmin for intensity, polarization vectors have a resolution of 32 arcmin.

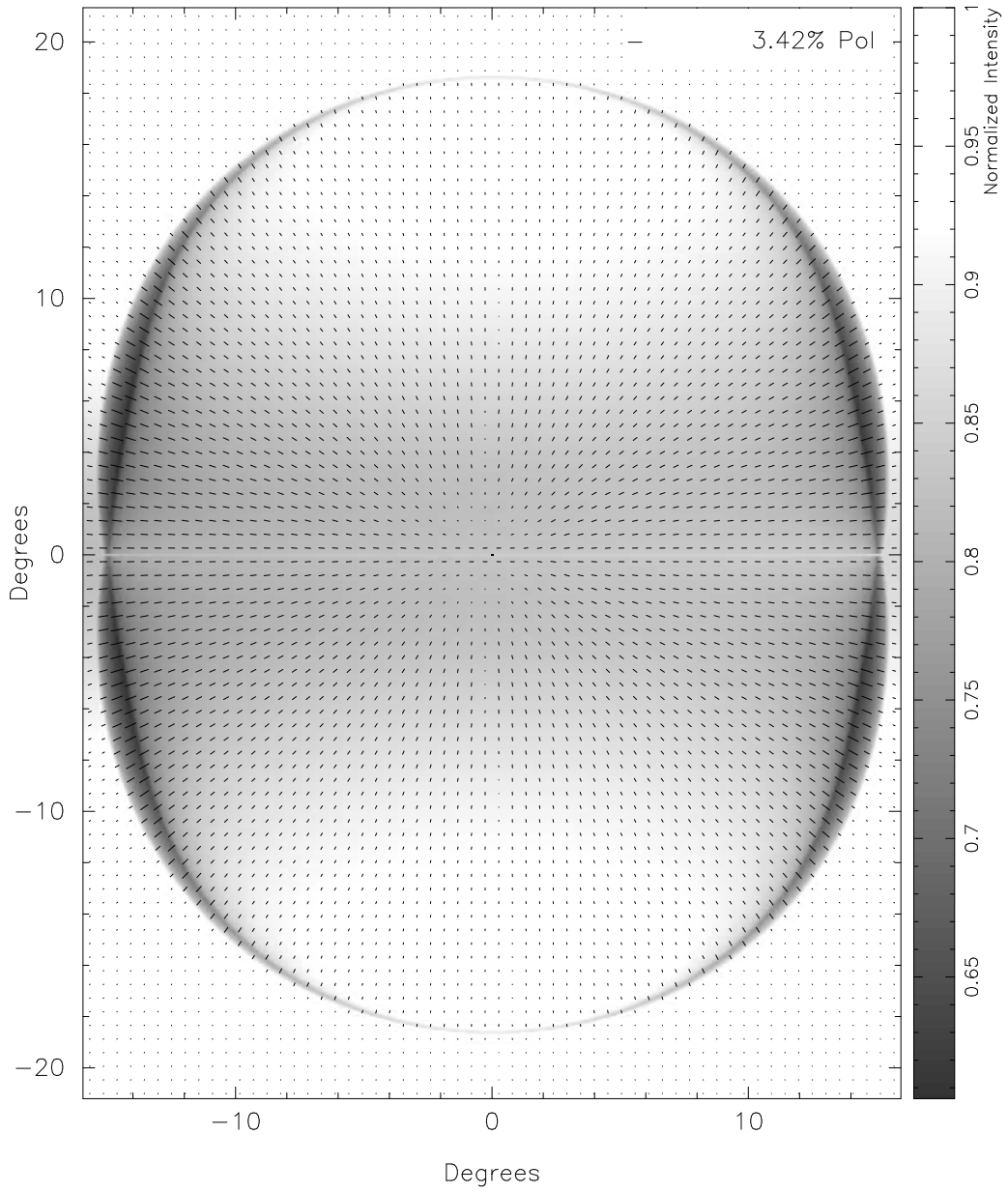

Figure 4.16 Polarization map from 2.2 micron unpolarized starlight passing through a Kompaneet's -like superbubble in a DL90 atmosphere with a line of sight parallel to undisturbed magnetic field at 1kpc distance from observers ($(b, l) \sim (80, 0)$.) Foreground included. Superbubble aged 2.8 Myrs with a luminosity of $3x10^{39} ergss^{-1}$. Resolution 4 arcmin for intensity, polarization vectors have a resolution of 32 arcmin.

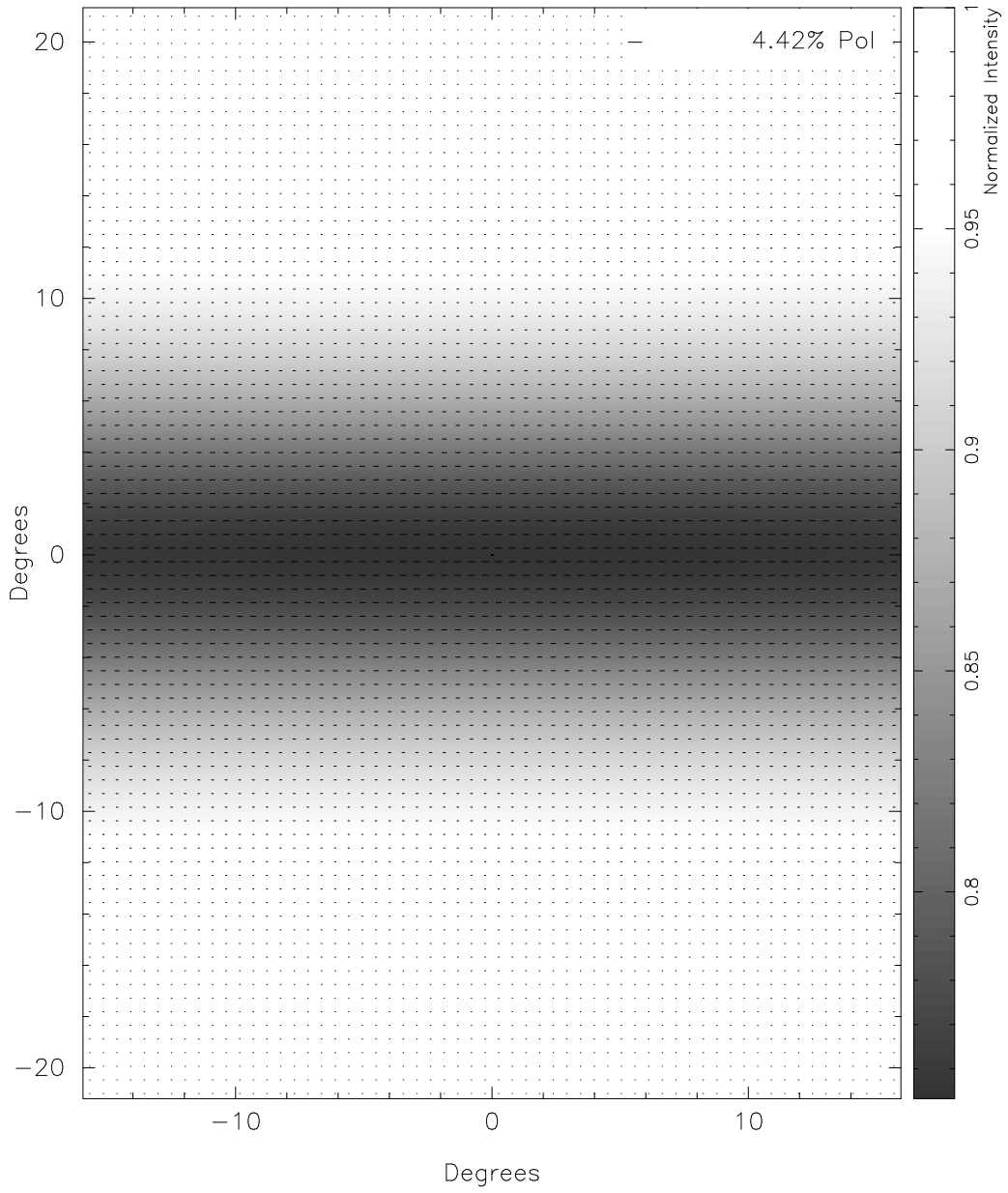

Figure 4.17 Polarization map from 2.2 micron unpolarized starlight passing through a DL90 atmosphere with a line of sight perpendicular to undisturbed magnetic field at 1kpc distance from observers ($(b, l) = (0, 0)$). Superbubble aged 2.8 Myrs with a luminosity of $3x10^{39} ergss^{-1}$. Resolution 4 arcmin for intensity, polarization vectors have a resolution of 32 arcmin.

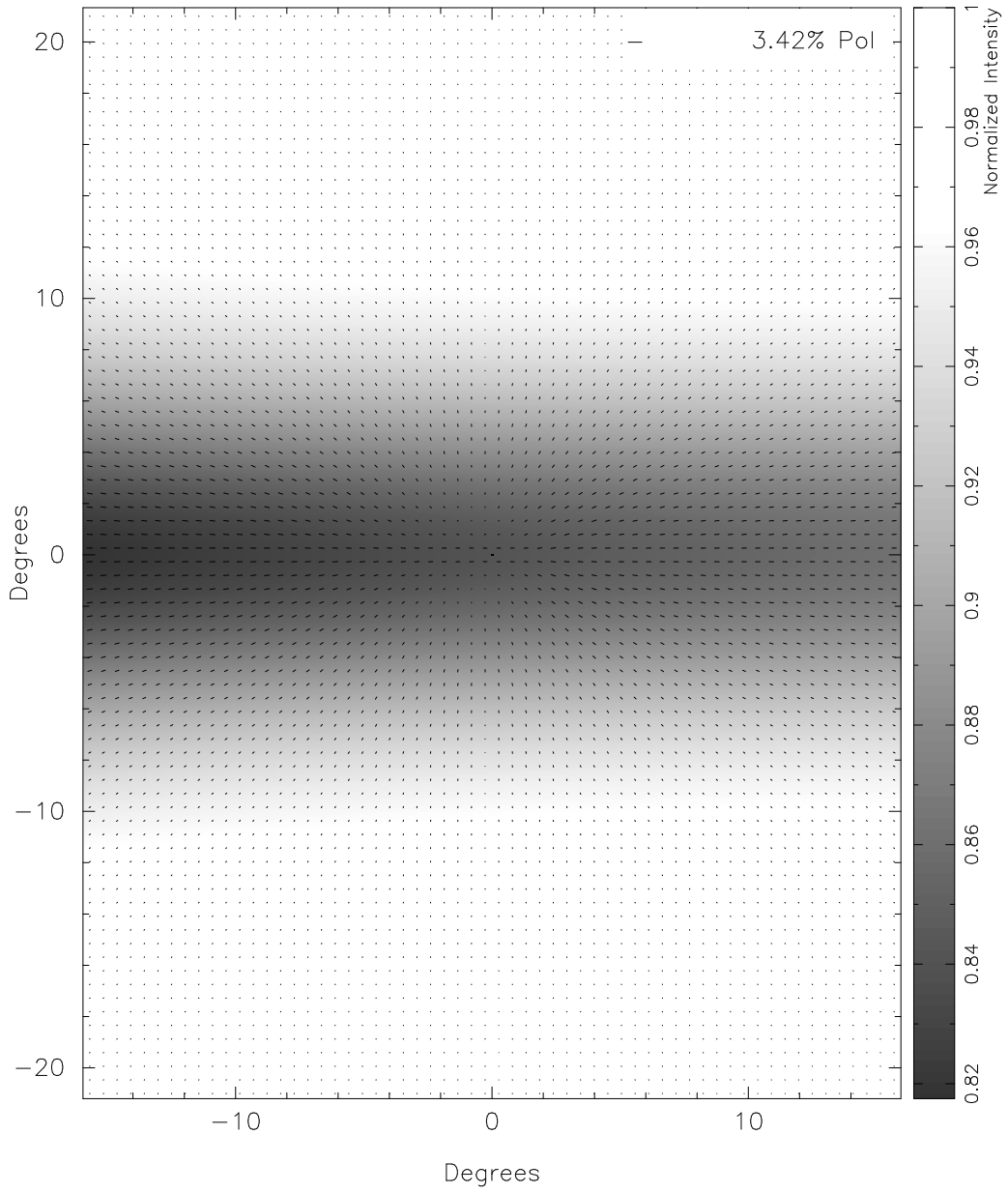

Figure 4.18 Polarization map from 2.2 micron unpolarized starlight passing through a DL90 atmosphere with a line of sight parallel to undisturbed magnetic field at 1kpc distance from observers ($(b, l) \sim (80, 0)$). Superbubble aged 2.8 Myrs with a luminosity of $3x10^{39} ergss^{-1}$. Resolution 4 arcmin for intensity, polarization vectors have a resolution of 32 arcmin.

Chapter 5

Numerical Simulations and Synthetic Observations

Though we can determine much about the density and magnetic field orientation changes produced by an evolving superbubble analytically such analysis often relies on assuming very limited conditions. As the superbubble evolves past the spherical stage numerical solutions become necessary as no analytical solution to the post-shock magnetic field is known. This stage is particularly of interest to us since we would like to determine the efficacy of a superbubble to produce vertical field components. Additionally, numerical simulations of superbubble growth can provide insights into the development of superbubbles under more realistic conditions that with what is possible analytically. Some of the preliminary ground work for the numerical modeling of superbubbles is covered in §5.1. From the simulations described in §5.2 we will create synthetic polarization maps (§5.3) and discuss the likelihood of observing changes in polarization created by superbubbles.

5.1 Numerical Modeling Setup

Numerical modeling is an incredible tool for understanding complex astrophysical phenomenon. However, like with all tools, improper use can lead to undesired results. In order to maximize the usefulness of our numerical modeling of superbubbles we first discuss what physical results we hope to achieve and then determine how well our given

computational resources can match these results. We also explore what new physical insights we can gain into the problem given our limitations in modeling.

5.1.1 Effects of Simulation Resolution

To effectively create synthetic polarization maps of an evolving superbubble we must capture the relevant conditions in the superbubble shell. If the shell becomes very small this can be difficult computationally since breakthrough superbubbles have a large vertical extent. In order to determine how well we are able to model the properties of a superbubble shell we use the analytical predictions to determine what resolution would be required and then preform various resolution tests.

From Chapter 3 we know that while the superbubble is still smaller in extent than the effective scale height of the gas that we can expect the shell to be $1/12^{th}$ of the superbubble radius. The radius grows with time, however, so at very early times the size of the shell will be very small. In fact at $t = 0$ the radius of the superbubble would also be zero. Though the analytical predictions assume energy is injected from a point source, this is not possible to replicate with numerical work (nor is it replicated in nature, each SN will have its own location.) To account for this, we can pick some starting time for the superbubble beyond $t = 0$ such that the radius of the energy injection corresponds to the expected superbubble radius. The energy and mass injection region is set at 20 voxels in radius (see §2.2.4). Naively we could assume that if the radius of the superbubble at the chosen starting time is r_0 the resolution is then $r_0/20$. However, discontinuities are difficult to maintain numerically, and generally require four or five voxels to resolve at all. Therefore the shell, which is the volume between the contact discontinuity and the forward shock, needs at least 8-10 voxels to exist numerically. With the superbubble radius only covering 20 voxels this clearly means the shell will be much larger than predicted from analytical considerations. If we decrease the resolution then either the same problem develops (because the resolution is still tied to the superbubble radius) or the injection radius must no longer represent the bubble radius at the chosen simulated starting time. In either case, the simulation will not be able to match the analytical predictions initially.

Though it is not possible to properly resolve the superbubble's development from some simulated starting time, it is possible that the resolution is sufficient to capture the

relevant shell properties at some later simulated time. In fact, expecting the simulation to match analytical predictions from the start is unreasonable, as the code needs more than one update to develop both shocks and the contact discontinuity. Depending on the proximity of these features their development may take quite a few updates. To this end we ran multiple simulations of a still spherical superbubble without cooling in an attempt to determine what resolution would be necessary to properly resolve the shell at some simulated time before the superbubble breaks through the disk. The simulations were allowed to run until the superbubble's forward shock reached the edge of the grid.

Three quantities were compared, the location of the forward shock, the shell thickness and the average shell density. The results of this can be seen in Figure 5.1. The forward shock location has an error on the order of the number of voxels required to maintain the shock (about 5 voxels), meaning the physical size of the error grows with decreasing resolution. The shell thickness measurement has twice this error (error 10 voxels) since both the contact discontinuity and the forward shock locations are spread over about 5 voxels. From plot (a), which shows the location of the forward shock, we can see that even down to a resolution of 2.5 parsecs per voxel, the plotted parameters are decently resolved after an initial adjustment period. However, the shell thickness, plot (b), is not well resolved at all even for a resolution of 0.25 parsecs per voxel. This is expected since we know at least ten zones are required to resolve the shell. The effect of this very poor resolution is reflected in plot (c), the shell density, which for every resolution is below the expected value of $4cm^{-3}$. It is likely that a resolution at least another order of magnitude greater, if not more, is required to bring the simulated shell thickness and density closer to the analytically predicted values.

Despite our inability to resolve the shell to a degree such that our simulations agree with analytical predictions, Figure 5.1 shows that the shell density peak is largely unchanged by resolution after the initial start up time has passed. The simulation with a resolution of 2.5 parsecs per voxel reaches a shell density greater than $3cm^{-3}$ after about half a million years, whereas the 0.25 parsecs per voxel simulation is already at this density by a time of ten thousand years. As long as one considers time periods after the half a million year mark, the simulation is as resolved as it is at 0.25 parsecs per voxel with only 2.5 parsecs per voxel. If we wish to investigate earlier periods the superbubble's evolution, a greater resolution than the 2.5 parsecs per voxel is necessary.

In fact, we can investigate the first million year history of the superbubble's evolution if we make sure to use the appropriate simulation.

5.1.2 Cooling

We know that strong cooling in the shell can produce much thinner and denser shells. With a thin shell, the contact discontinuity and forward shock are very close to one another, increasing the difficulty in resolving either structure. Strongly cooled shells are very thin and therefore difficult to resolve. As an example consider a shell thickness of ~ 0.05 parsecs. This is the thickness of a strongly cooled shell at $1x10^5 years$ when a superbubble with a luminosity of 10^{39} is about 50 parsecs in size. It would require at least $1x10^4$ voxels in one direction to model from the center of the bubble to the forward shock with a resolution of $0.05pc$ per voxel. As noted before, more than one voxel is necessary to resolve discontinuities, meaning a resolution at least 10 times greater than this is necessary.

Such resolution simply isn't possible with a fixed grid. To accurately solve for the development of a cooled superbubble, adaptive mesh refinement is necessary. Stil et al. (2009) seek to resolve cooling in their simulation by decreasing their timestep size to a tenth of the cooling time. However, without changing the physical resolution, this can lead to numerical errors as it effectively shrinks the CFL condition and increases the total round-off error. Particularly troubling is that the numerical diffusion this produces can smear out the numerical thickness of shocks, exactly the opposite effect we wish to produce when cooling is included.

Since we cannot come close to resolving the shell, the simulation will not reliably reproduce the properties predicted by our analytical model. To understand the effect resolution will play in determining how well we can reproduce expected cooled superbubble shell properties we ran simulations of early (before breakthrough) superbubble development at different resolutions. Figure 5.2 shows the results of such tests. [1]

[1] Our initial cooling runs found the shell cooling before the times predicted by any measure of when strong cooling should begin. This is likely due to the in-term temperature in the bubble shell as the shock is developing. Since a few updates are needed to numerically establish the forward and reverse shocks, the temperature in these features must grow from the ambient temperature and go through the temperature required for efficient cooling before the physical shock would adiabatically cool to this temperature. To avoid this we artificially prevent cooling until the simulation demonstrates a well developed adiabatic shock.

Though the location of the forward shock is well solved for, as in the uncooled runs, the shell density and thickness are significantly worse than even the poor results of the simulations without cooling.

As before in the simulations without cooling, we know a better resolution is necessary to reproduce the expected analytical shell thickness and density. From Figure 5.2 we see that the shell density is as resolved at 0.5 parsecs per voxel as it is at 1.0 parsecs per voxel after the latter has a simulated age of at least 0.3 million years. [2]

Without being able to resolve the shell the shell produced numerically is not as dense as expected. What can we hope to learn from our numerical simulations? To answer this we consider the two regimes of superbubble development and how we might expect to observe polarization from such a superbubble. For a superbubble that has not reached breakthrough, the density of dust in the plane is very large and will provide a large foreground and background component to the total observed flux. If computational effort were not a limiting factor, then the large density of a strongly cooled superbubble shell in its very early stages of development could possibly provide enough flux to produce an observable difference from the background. Knowing that the density we would produce with simulations is not nearly what is predicted by a strongly cooled shock, is it useful to run or study such a simulation?

5.1.3 Simulation Limitations

Knowing that the density in the shell is not as large as predicted only tells us that the flux from the shell would be smaller than the expected value. However, by ignoring the magnitude of this flux and only considering the polarization angle produced by elements of the shell, we can still qualitatively describe the expected change in polarization a superbubble would have in a quiescent galactic environment. So the usefulness of such simulations depends on the magnetic field behavior in the unresolved shock. In the case of a still spherical superbubble, the field is changed only through compression. Components of the field parallel to the shock normal are unchanged, while components of the magnetic field perpendicular to the shock normal see a magnitude increase equal

[2] It may be possible that this resolution reaches a peak shell density sooner than this, since cooling is artificially held off until an adiabatic shock is well established. From plot (c) in Figure 5.2 we can see there is a delay between the simulation reaching a peak density for a quasi-resolved adiabatic shock and the peak density for the isothermal shock that develops after cooling is activated.

to the compression ratio of the gas. Since the density of the gas is not properly solved for, it is reasonable to guess that the post-shock perpendicular components of the field will not be as large as predicted. This would mean our simulations would under-report the change in polarization as it is only the perpendicular components of the magnetic field which produce a polarization angle different than that of the ambient medium. [3] Since the observations that we would like to replicate do not need to accurately determine the strength of the magnetic field, but only its orientation, will this failure to reproduce the predicted compression ratio undermine our synthetic image production?

When the compression ratio is very large, as in the case of a young, luminous superbubble with a strongly cooled shell, then the downstream component of the magnetic field tangential to the shock will be much larger than the downstream component normal to the shock. In such a case the normal component of the field in the shell is negligible compared to the tangential component and the field can be assumed to lay tangential to the shock. As long as we can assume strong cooling (which also requires that the shock be a strong one) then we should be able to reasonably assume that field direction found by the code has the same orientation as what would be predicted analytically, if not the same magnitude. However, this is not quite the case near the plane! Near the plane, the superbubble's expansion will lie (or nearly do so) parallel to the magnetic field. Here the component of the field tangential to the shock is very small and any diffusion of the predicted compression will undermine the amplification necessary to make the tangential component of the magnetic field much larger than the normal component.

To further understand our limitations in accurately simulating the effect of a pre-breakthrough superbubble on a plane parallel magnetic field we compared the field produced by a simulation of a still spherical superbubble with the predicted post-shock magnetic field. The results of this are seen in Figure 5.3. Two epochs of superbubble development are shown, both at very early times (0.2 and 0.5 million years.) In both epochs at locations well above the plane the magnetic field found by the simulation is well matched to the analytical field orientation. Closer to the plane, the simulation finds a field orientation that is much less tangential to the bubble's forward shock and more parallel to the plane of the gas. Interestingly, the earlier epoch does a poorer job

[3] Obviously turbulence in the ISM, or any kind of fluctuation in the magnetic field orientation along the line of sight would cause the observed polarization to deviate from our simplified toroidal field. We are ignoring these complications.

of matching the expected field orientation than the later epoch. Note however, that it is not the simulation's field orientation which changes to bring a closer match between the simulation and the analytical field orientation. The analytical field orientation changes significantly between the two epochs. This change is best accounted for by the drop in the forward shock speed, and correspondingly the shell's compression. The large compression ratio predicted in the earlier epoch is simply not resolved, and so there is a large disparity near the plane where the magnetic field orientation would be most susceptible to this disparity. As the superbubble ages the shock slows, and the compression ratio drops enough that near the plane the field orientation in the simulation is not significantly different from the analytical prediction.

What the previous discussion means is that there is a window in which we can expect physically reasonable predictions for our spherical superbubble polarization maps, certainly when considering the change in polarization angle for light emitted from or transmitted through the superbubble itself.

5.1.4 Kompaneet's Approximation

What can be gained from simulating a post-breakthrough superbubble? Superbubbles that breakthrough are necessarily evolved superbubbles, with shock velocities smaller than for the same bubble during its spherical expansion phase. A smaller shock velocity means a thicker shell and smaller densities. Since we are unable to resolve the shell when the superbubble is very young, later evolution may be the only way to create a simulated superbubble that comes close to the expected results. [4] Though a superbubble that has broken through the disk is older, and therefore has a smaller compression ratio than a younger bubble, the large vertical extent of such a bubble would mean some lines of sight to the superbubble shell would rise above the galactic plane. Since lines of sight out of the plane would pass through less foreground and almost no background, the increased density of the shell could be more detectable. Our semi-analytical breakthrough superbubble models showed this result, particularly with dust emission.

[4] Smaller luminosity superbubbles would also have smaller shock velocities, but at earlier times than a larger luminosity superbubble. Reaching a weak shock velocity before the superbubble is about a scale height in size would prevent such a bubble from breakthrough.

Since our analytical work was based on a superbubble that developed following Kompaneet's approximation we would like to know how well our simulations are able to reproduce this theory. To determine this we compare a simulation of a superbubble expanding into an exponential atmosphere at a resolution of 2 parsec per voxel. We do not include strong cooling. For reference this simulation is called Kn2p0. We know that the limited resolution of our simulations can only minimally capture the analytical shell thickness and density for the spherical case and assume that it is similarly poor for the Kompaneet's approximation. [5] The largest difference from the spherical problem is the shape of the bubble's forward shock, so we compare the shape of our simulation of a Kompaneet's superbubble to the semi-analytical description of the shock given by equation 4.5 for three stages of the superbubble's life. This comparison can be seen in Figure 5.4.

Early in the superbubble evolution the shell is poorly resolved and the locations of the forward shocks and contact discontinuities do not match well though the shape of the superbubbles do, though the superbubble is still largely spherical in these cases. (see plots (a) and (b) in Fig. 5.4). Looking at plot (c) though we see that the shape of the simulated superbubble is not the same as predicted by the Kompaneet's approximation. The Kn2p0 simulated superbubble is not as elongated as the semi-analytical superbubble. Though this difference could be the effect of resolution, the simulation does not reproduce the assumptions of the Kompaneet's approximation. The pressure within the simulated superbubble is not uniform, decreasing with height above the plane. A smaller pressure than predicted would mean a smaller expansion velocity, which could explain why the shock surface near the top of the bubble is not as far along as the Kompaneet's approximation would predict.

In the absence of an analytical description for the magnetic field, we assumed a toy model to create synthetic polarization images for our semi-analytical Kompaneet's superbubbles. Using the Kn2p0 simulation of a superbubble we would like to explore the accuracy of this model. Figure 5.5 shows a slice of simulation Kn2p0 at 2.8 Myrs

[5] Part of the difficulty in resolving the spherical shell structures is in the geometry of the problem, since the Kompaneet's approximation is nearly a cylindrical expansion for late evolution times, it may be that we are better able to resolve the shell structures. However, at later evolution times the shell itself would be thicker and easier to resolve in that respect, but we do not simulate the superbubble at such a late age.

with density in color and the magnetic field lines shown in black. From this image we can see that the field lines do not lie parallel to the shock front as assumed. However, we did not include cooling, and cooling would significantly increase the compression ratio and therefore the post-shock tangential field components, a situation which would be much closer to our assumptions. One interesting aspect of the magnetic field seen in Fig. 5.5 is the persistence of down-wind vertical components. Though the post-shock field decreases in magnitude, there is not a significant change in orientation.

5.2 Simulations of a Superbubble in a DL90 Atmosphere

5.2.1 Description of Simulations

In this section we describe the large simulations preformed, not including the resolution tests. With the exception of the Kompaneet's run described in the previous section the runs preformed use an atmospheric setup described in section 2.2.2. Two simulations with this atmosphere were preformed, one with cooling and one without cooling. Table 5.3.2 shows a few parameters of the three simulations (including Kn2p0).

Ideally we could simulate a breakthrough superbubble at sub-parsec resolution through tens of millions of years. Realistically, computational resources are limited and we instead focus on trying to simulate a superbubble with moderate resolution long enough to see the superbubble breakthrough. Since a resolution of 1 parsec per voxel gave fair results for a superbubble age greater than a few hundred thousands of years, we chose this resolution for a large-scale simulation. To see the superbubble breakthrough we need to model the superbubble on domain with an extent larger than the superbubble's eventual dimensions. Since we are limited computationally we are therefore limited as to how long we can evolve the superbubble since the superbubble will grow larger with time.

Because of this we originally ran a very large simulation grid with the hopes of evolving the simulation out to an advanced superbubble age. However, the run with cooling experienced significant numerical issues just before it reached a simulated age of 3 million years. Since we significantly under-resolved the physics within the shell as it is cooled such difficulties are not entirely unexpected. For the simulation without cooling we ran a slightly smaller grid, though with the same resolution.

Both simulations used a superbubble with a luminosity of $3.15x10^{39}$ ergs s^{-1} equivalent to about 1000 supernovas in ten million years. This is incredibly luminous and unlikely to represent most superbubbles encountered, however such a large luminosity does provide the greatest chance for creating an ideal case to detect superbubble polarization.

Slices of dust density and magnetic field vectors for the simulations at 0.5 Myrs can be found in Figures 5.6 and 5.7 and at 2.8 Myrs in Figures 5.8 and 5.9. Only a quarter of the simulation cross-sectional area is shown, and the simulation is symmetric across each axis. There is not large difference in the orientation of the magnetic field in the shell between the simulation with cooling (Lc1p0) and the simulation without (Ln1p0) for early times when the superbubble is still spherical, though the density for the cooled shell is predictably larger. The images of the later superbubbles show a large difference in magnetic field orientation in the shell between a cooled shell and an adiabatic one. Near the top of the superbubble in Fig. 5.9 we see a magnetic field orientated predominately tangentially to the shock surface through out the entirety of the shell. Nearer to the plane, where the shock is essentially perpendicular to the galactic plane, we see very different structure. Here there is an increase in the vertical component of the magnetic field from the forward shock to the contact discontinuity. The field must be undergoing evolution in the post-shock environment.

It is unclear that the cooled superbubble would have this gradient in vertical field components. Our simulations are under-resolved, and the shell is so then that shell properties are not accurately resolved for a single average value, much less for a change in values across the shell. However, we do see in 5.8 that the field lines lie roughly tangential to the shock surface.

It is also important to mention that our cooled simulation, Lc1p0, is not a breakthrough superbubble as we have defined it at an age of 2.8 Myrs, though the simulation without cooling Ln1p0 is. This is due to the energy lost to cooling, which reduces the energy available for expansion into the ISM. As both bubbles are no longer spherical though, we continue with our analysis as it is clear that there has been some change to the superbubble's morphology due to the gradient of the galactic atmosphere.

5.3 Synthetic Polarization Maps

Now that we have created simulations of a superbubble with and without cooling we can investigate the plausibility of spherical and breakthrough superbubbles to produce detectable polarization changes in Near-IR and sub-millimeter polarization.

5.3.1 Cooled Superbubble - Lc1p0

First we discuss the polarization produced by simulation Lc1p0. In order to compare with our analytical results from Chapters 3 and 4 we first look at the polarization produced by just the superbubble in dust emission and transmitted starlight. Figures 5.10, 5.11, 5.12 and 5.13 show nearly identical polarization structure to that predicted by our model spherical superbubbles from Chapter 3. However there is a discrepancy between the predicted strength of the polarization and what was found from our simulated superbubbles, with our simulations not producing as strong a polarization. This is likely due to our inability to resolve a cooled superbubble shell properly.

Figures 5.18, 5.19, 5.20 and 5.21 show the polarization produced by the superbubble from simulation Lc1p0 at an age of 2.8 Myrs. As with the still spherical superbubble the polarization structure seen in these figures is remarkably similar to the polarization seen in Chapter 4, though the percent of light that is polarized is almost uniformly smaller in our simulations than in our analytical models of superbubbles. It is possible that this difference is due to our over-estimating the vertical magnetic field components. However, it is also possible that this difference is due to the poor resolution of our simulations.

Just as we did with our theoretical superbubbles, we embed the superbubble from simulation Lc1p0 in the galaxy to include foreground and background components. These maps can be seen in Figures 5.22, 5.23, 5.24 and 5.25. Here we do see a difference from our theoretical maps. Figure 5.22 shows evidence of the polarization created by the superbubble along the barely detectable in unpolarized intensity shell. This polarization is not as dramatic as that produced by our theoretical superbubble (see Figure 4.11). The theoretical superbubble shell is brighter in unpolarized intensity, but again, our simulations did not reproduce the large compression ratios of our theoretical model due to low resolution. It is possible that we could see more evident superbubble polarization

with a better resolved shell.

Looking at our synthetic images of the Lc1p0 simulated superbubble in transmitted starlight, figures 5.23 and 5.25, we see a good agreement with the predictions of our theoretical models in Chapter 4. A superbubble 1kpc distant towards the galactic center essentially disappears into the foreground. Our theoretical superbubble, as with dust emission, shows a stronger polarization than our simulation. However, the theoretical superbubble was not even detectable in polarized transmitted starlight.

5.3.2 Superbubble without Cooling- Ln1p0

Though we expect that strong cooling in the superbubble shell will provide the greatest chance of detecting superbubble polarization, we wish to compare the polarization signature of a strongly cooled superbubble to one without strong cooling. To do this we use the superbubble from our Ln1p0 simulation to create a polarization map for the most optimistic scenario found for the strongly cooled case. Figure 5.26 shows the expected dust polarization from the Ln1p0 superbubble and 5.27 shows the superbubble at an age of 2.8Myr at a galactic location of (0,0) with foreground and background components added. We see from Fig. 5.27 that the superbubble polarization signature is very obvious with a large angular area producing polarization with strong horizontal components.

How is it that our simulation without cooling produces such an obvious signature, larger than that produced by Lc1p0 despite the predictions of the work done in Chapter 3? Our findings in Chapter 3 were based on lines of sight that did not look out of the plane, but were instead always parallel to the galactic plane. GRIZZLYEYE can use non-parallel lines of sight, and this is likely the key to the detectability of this superbubble. Without cooling to remove part of the superbubble's energy, the bubble expands to a much larger size than the superbubble in Lc1p0. This places a portion of the shell, where vertical field components have been created, along a line of sight that passes out of the plane. By rising above the plane of the galaxy the foreground, and more so the background contributions dwindle leaving the superbubble's polarization more visible.

Our inability to resolve the shell and perhaps accurately capture the relevant aspects of superbubble evolution limits our authority to determine the plausibility of detecting

polarization from superbubbles. However, for select cases we are able to detect polarization from a superbubble even with galactic contributions.

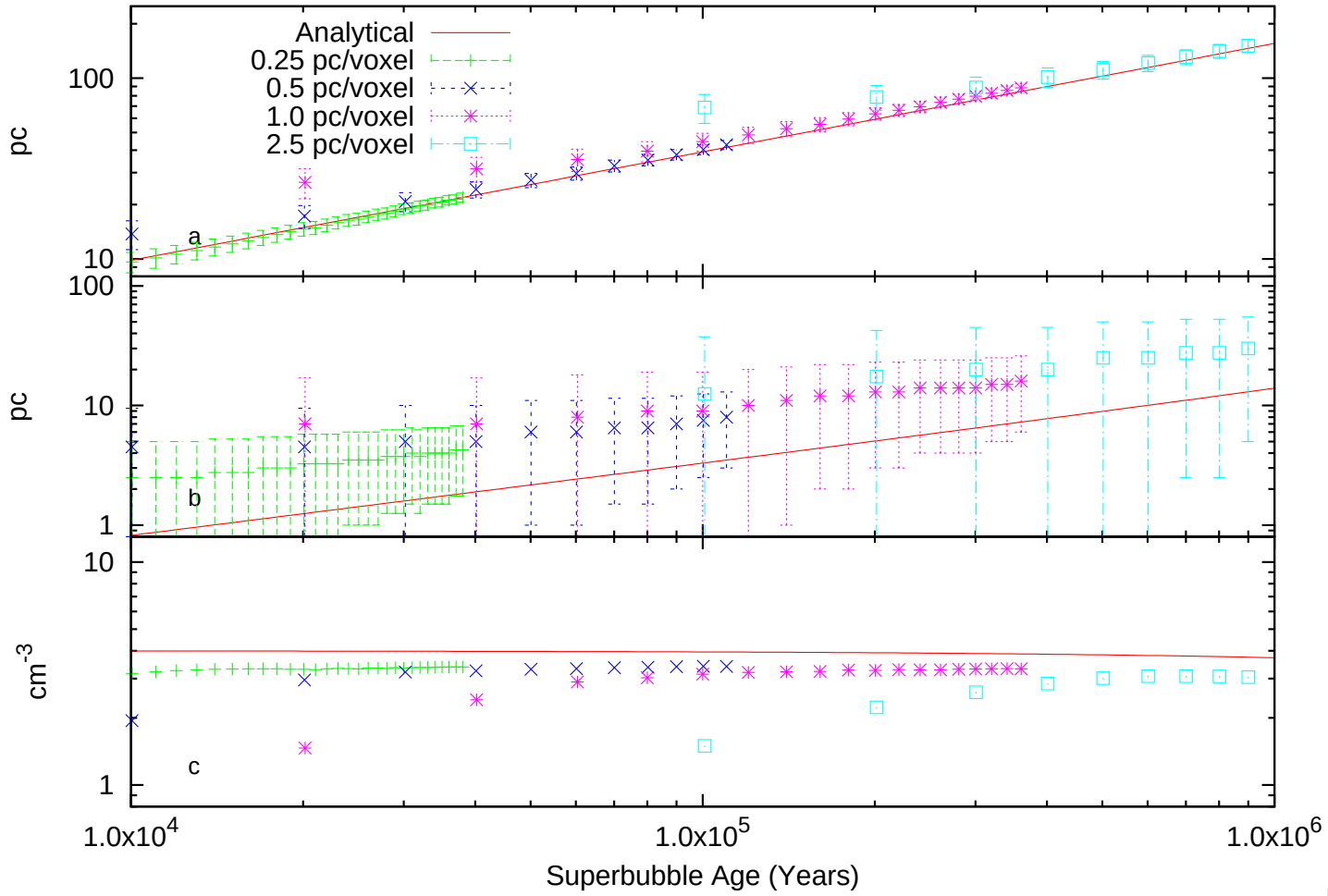

Figure 5.1 Resolution tests for an uncooled superbubble. Simulations with resolutions at 2.5, 1, 0.5 and 0.25 parsecs per voxel are shown with the analytical predictions discussed in §3.2 from Weaver et al. (1977). Plot (a) shows the location of the forward shock. Plot (b) shows the shell thickness and plot (c) shows the shell density.

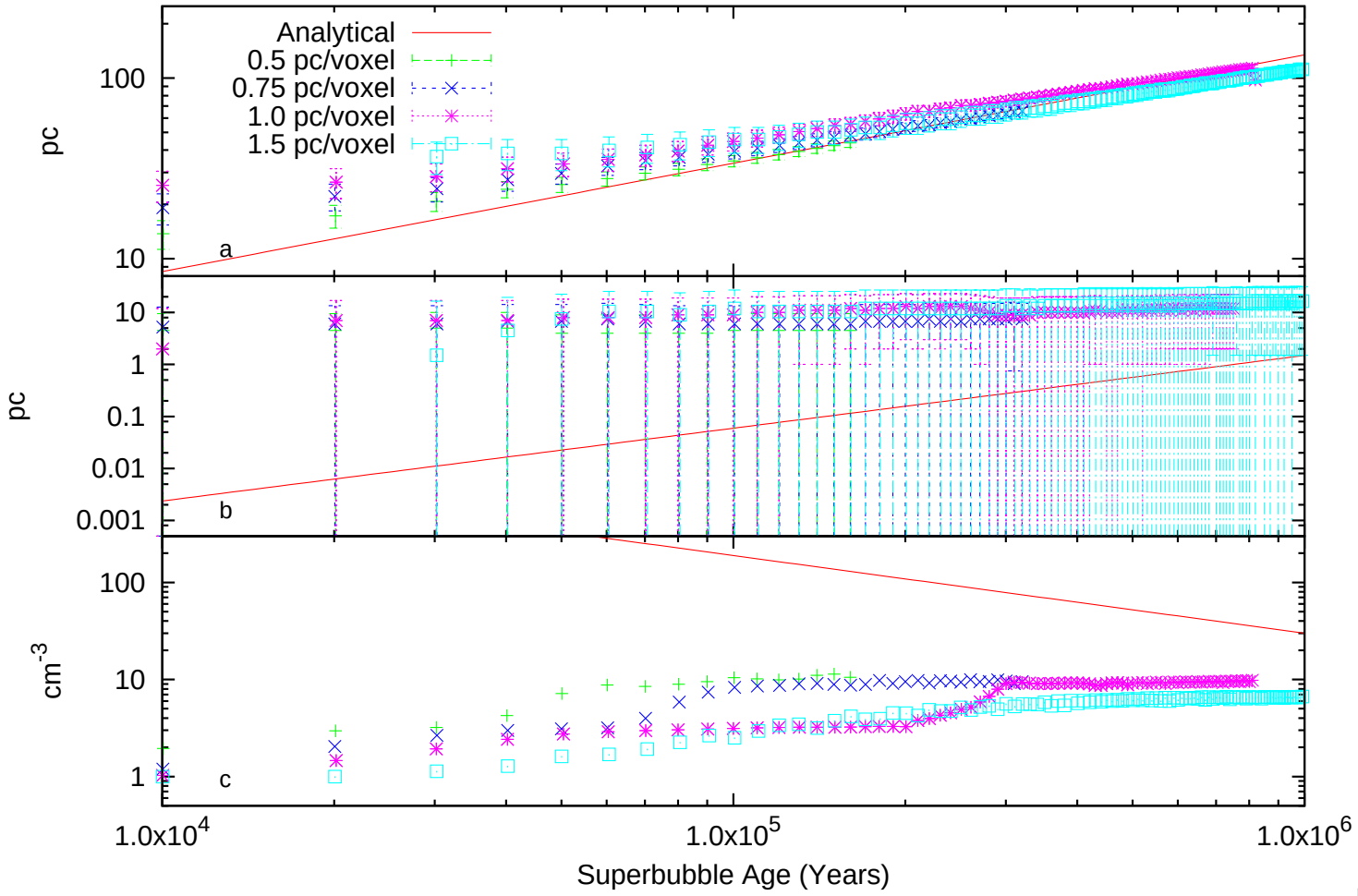

Figure 5.2 Resolution tests for a superbubble with a strongly cooled shell. Simulations with resolutions at 1.5, 1, 0.75 and 0.5 parsecs per voxel are shown with the analytical predictions discussed in §3.2 from Weaver et al. (1977). Plot (a) shows the location of the forward shock. Plot (b) shows the shell thickness and plot (c) shows the shell density.

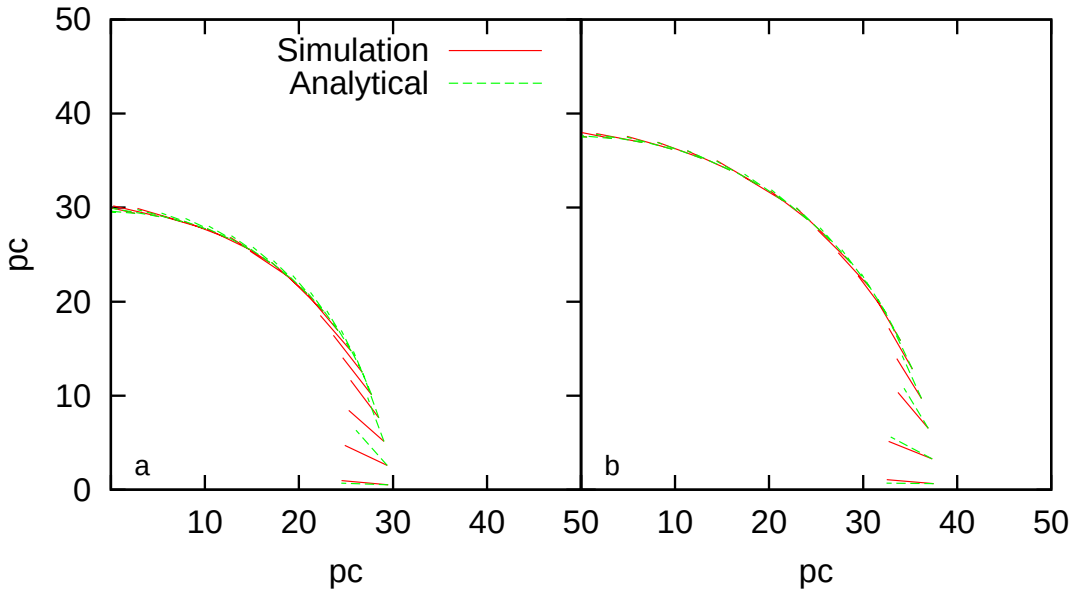

Figure 5.3 Superbubble shell magnetic field lines at (a) 0.2 Myrs and (b) 0.5 Myrs in x-y plane. Simulations field lines are shown in solid red, the analytical prediction (from RK jump conditions) are shown in dashed green.

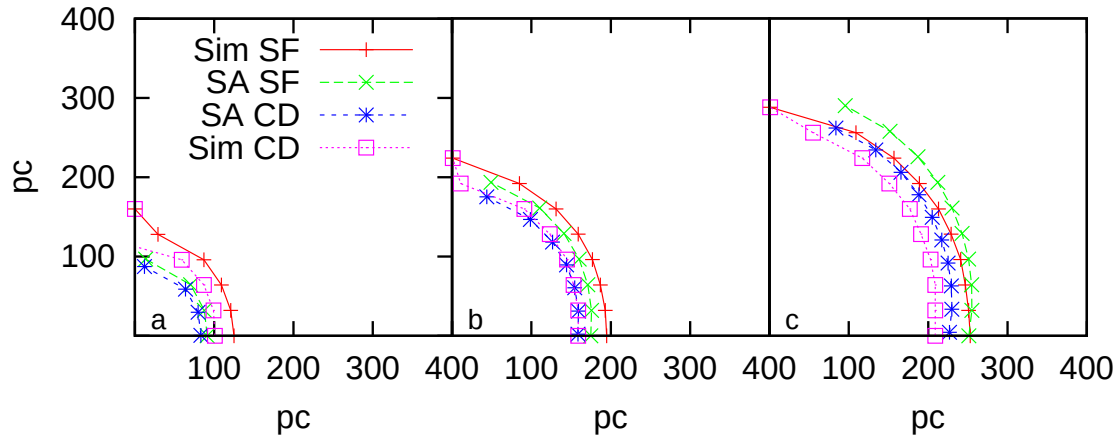

Figure 5.4 Comparison of superbubble shell for simulated superbubble with the shell predicted by Kompaneet's approximation for three epochs. Plot (a) shows 0.5 Myr, (b), 1.5 Myr and (c) 2.8 Myr. Sim SF is the simulation shock front, SA SF is the semi-analytical shock front, Sim CD is the simulation contact discontinuity and SA CD is the semi-analytical contact discontinuity.

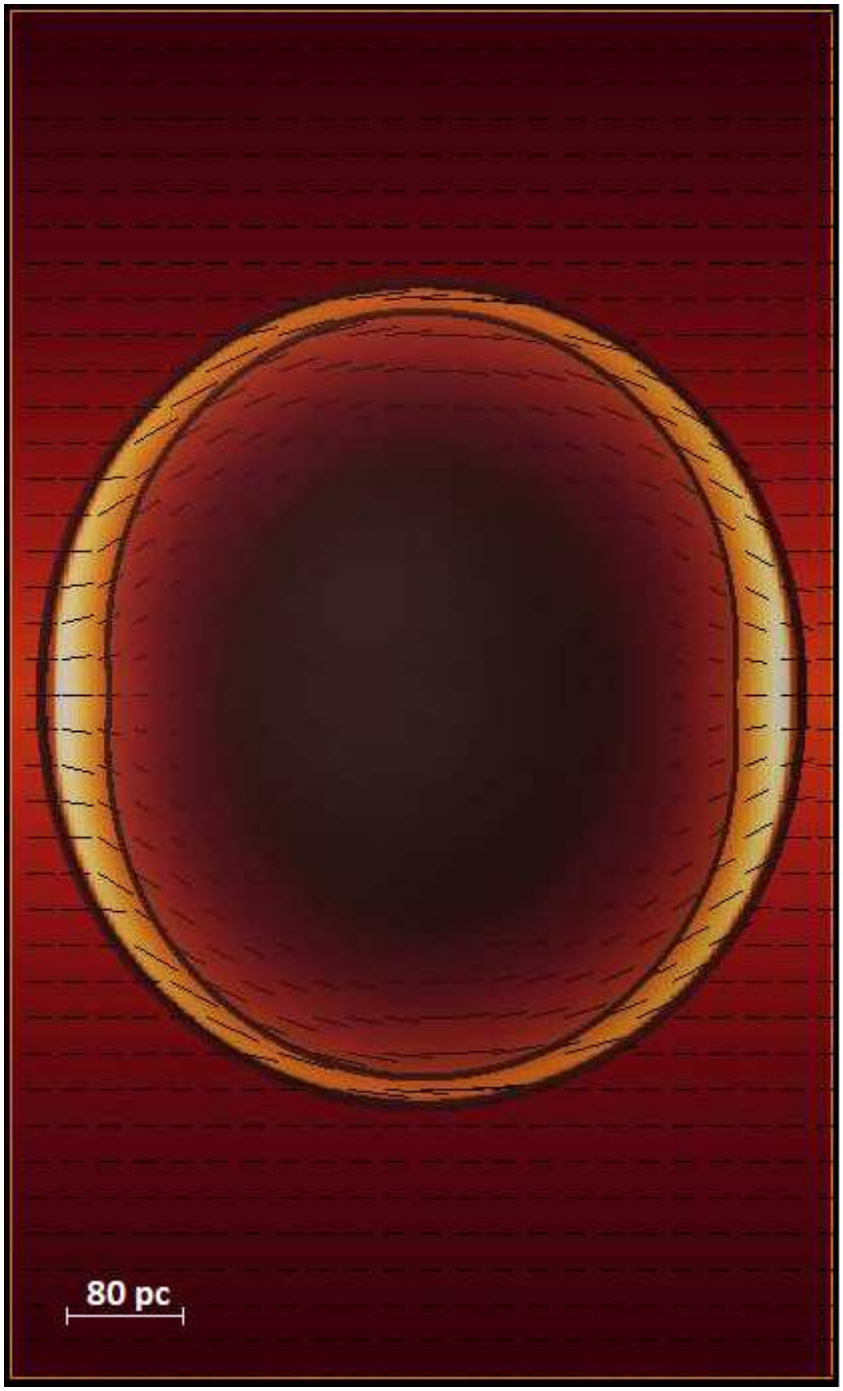

Figure 5.5 Slice in the $x-z$ plane of a simulation Kn2p0 at a time of 2.8 Myrs. Density is shown in color and the magnetic field orientation through this slice is shown as black lines through this slice. The density range is from 0 to 3.2 cm^{-3}.

Table 5.1. Simulation Parameters

Name	Atmosphere	Cooling	Resolution	Size
Kn2p0	Exponential	No	2 $^{pc}/_{voxel}$	$288 \times 288 \times 480$
Lc1p0	DL90	Yes	1 $^{pc}/_{voxel}$	$896 \times 896 \times 1408$
Ln1p0	DL90	No	1 $^{pc}/_{voxel}$	$704 \times 704 \times 1408$

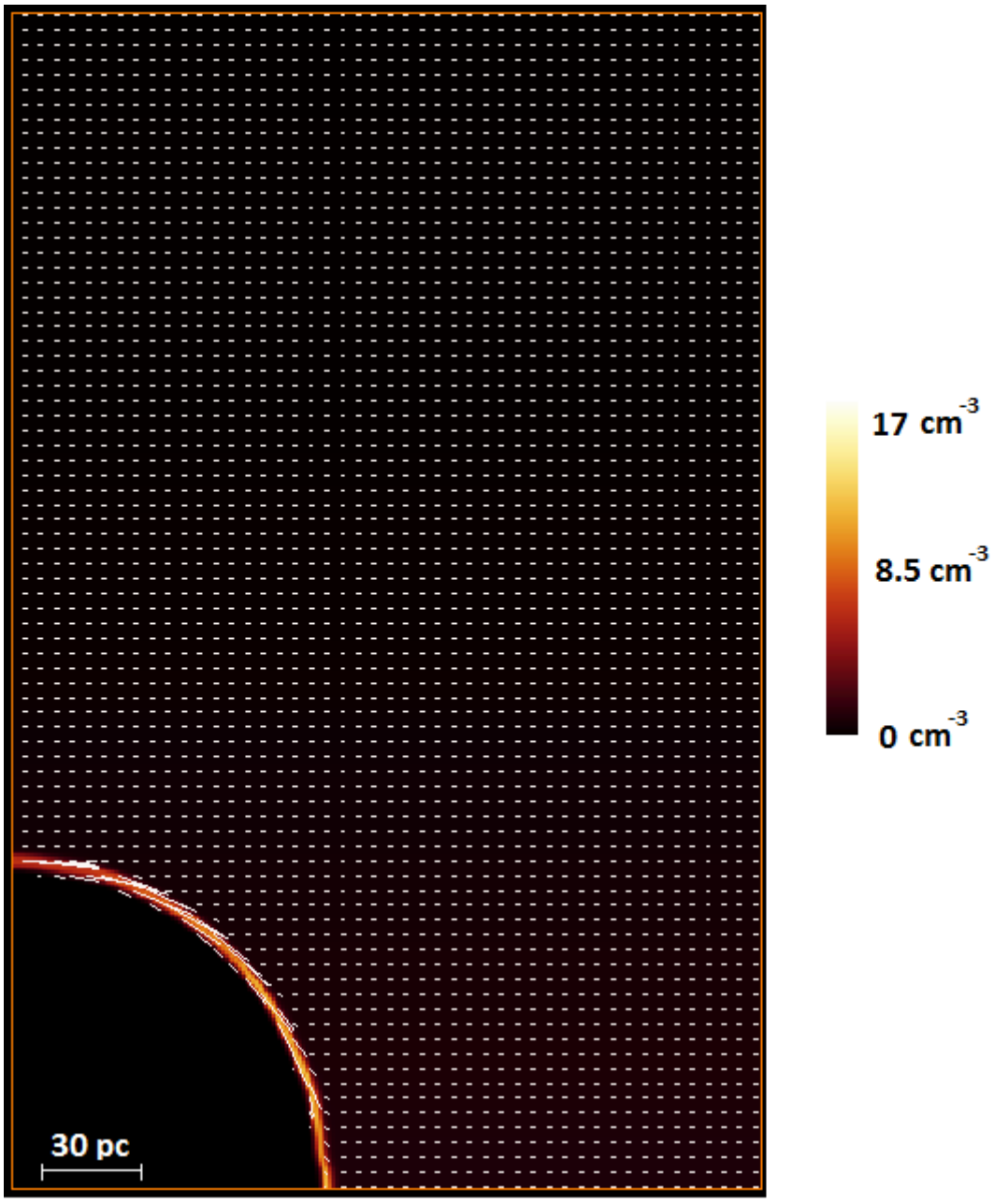

Figure 5.6 Slice in the $x-z$ plane of a simulation Lc1p0 at a time of 0.5 Myrs. Density is shown in color and the magnetic field orientation through this slice is shown as black lines through this slice.

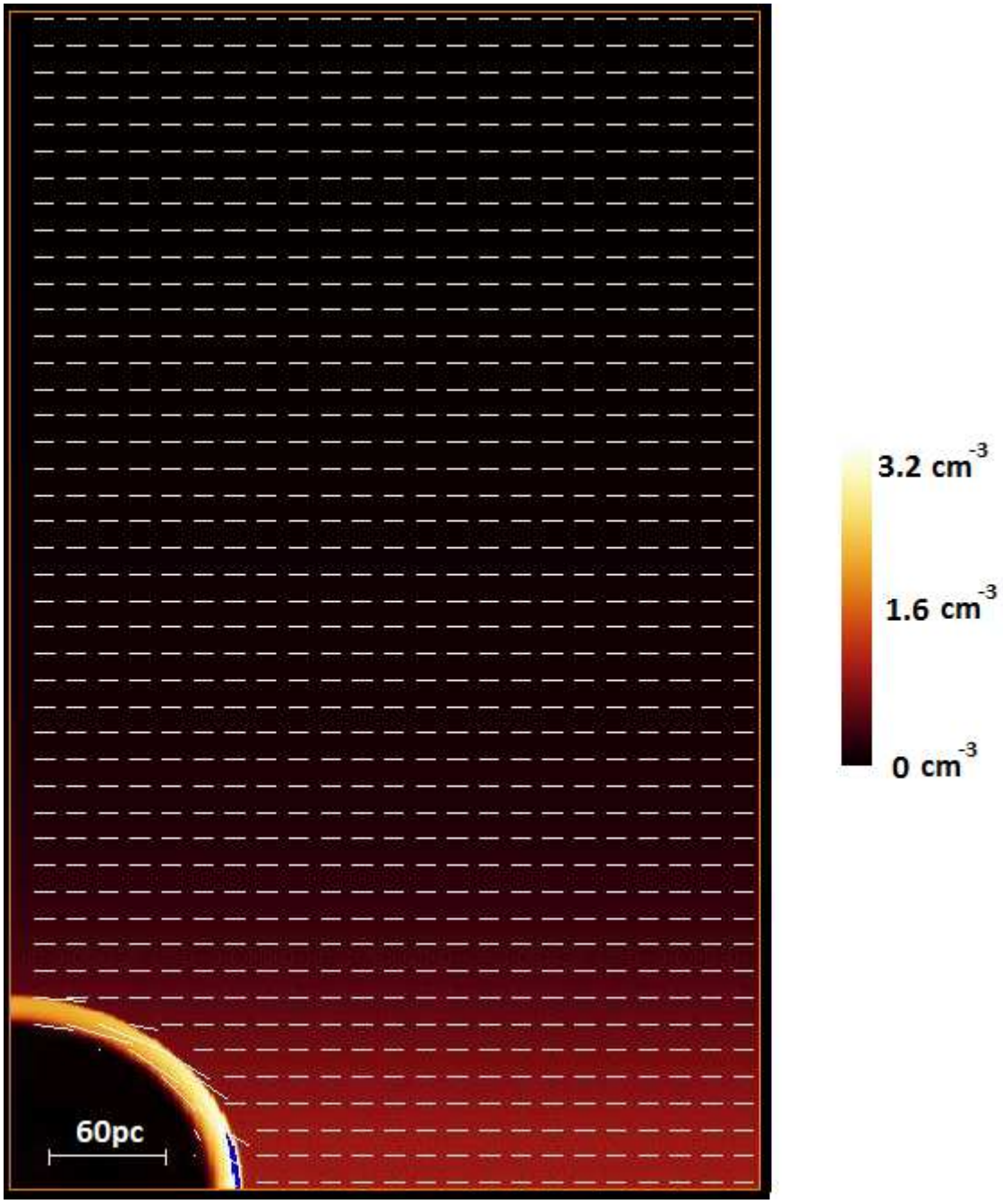

Figure 5.7 Slice in the $x-z$ plane of a simulation Ln1p0 at a time of 0.5 Myrs. Density is shown in color and the magnetic field orientation through this slice is shown as black lines through this slice.

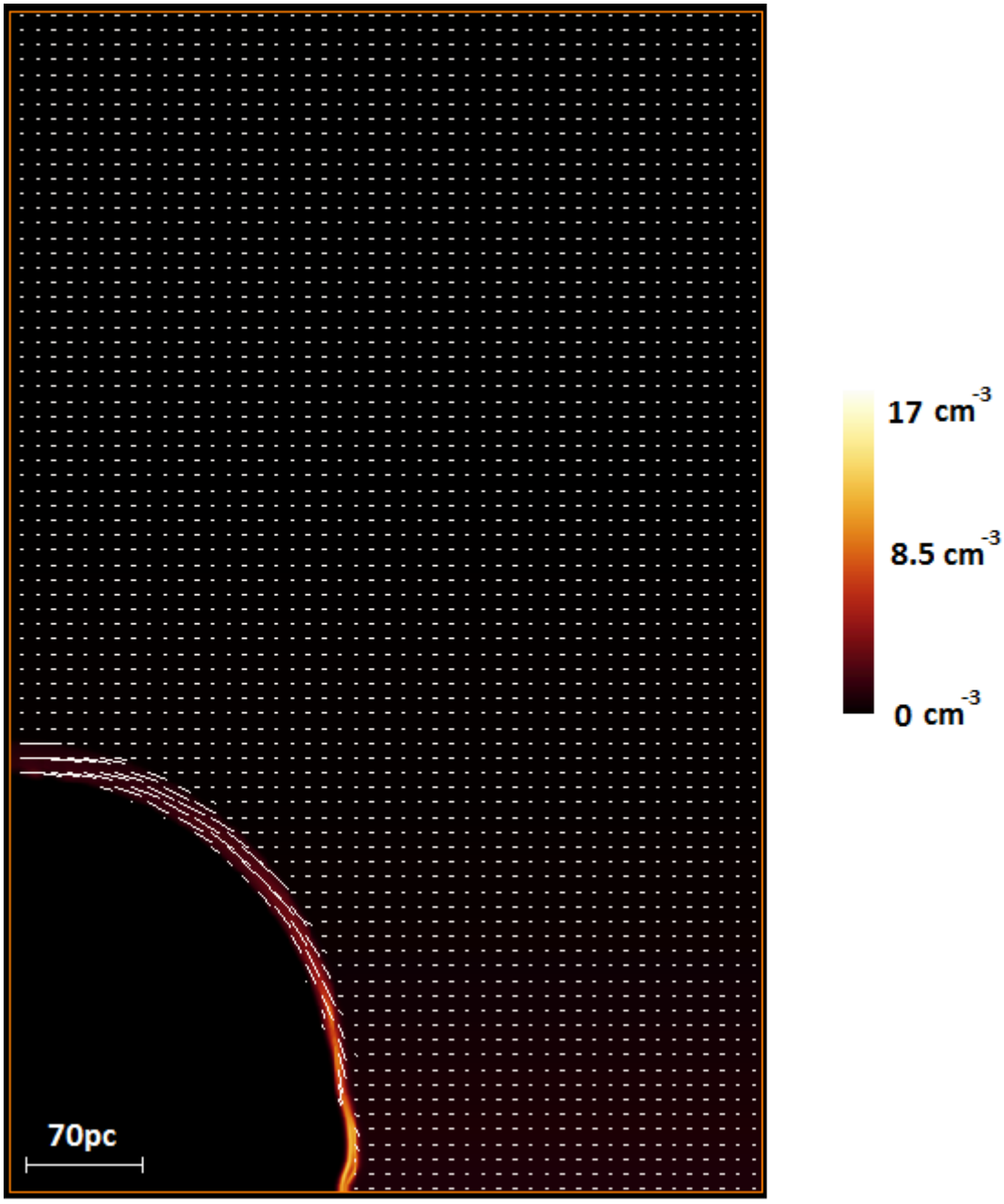

Figure 5.8 Slice in the $x-z$ plane of a simulation Lc1p0 at a time of 2.8 Myrs. Density is shown in color and the magnetic field orientation through this slice is shown as black lines through this slice.

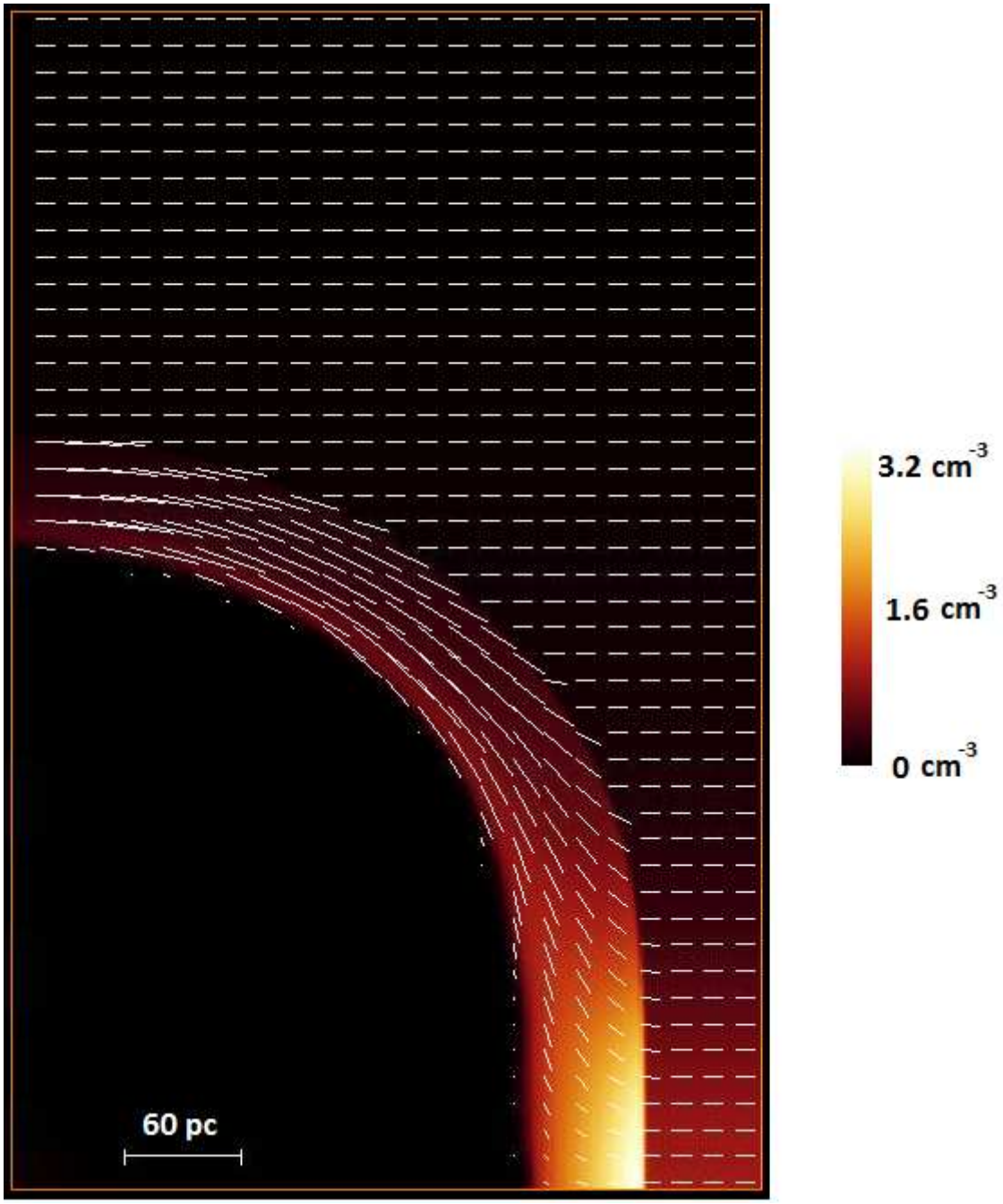

Figure 5.9 Slice in the $x-z$ plane of a simulation Ln1p0 at a time of 2.8 Myrs. Density is shown in color and the magnetic field orientation through this slice is shown as black lines through this slice.

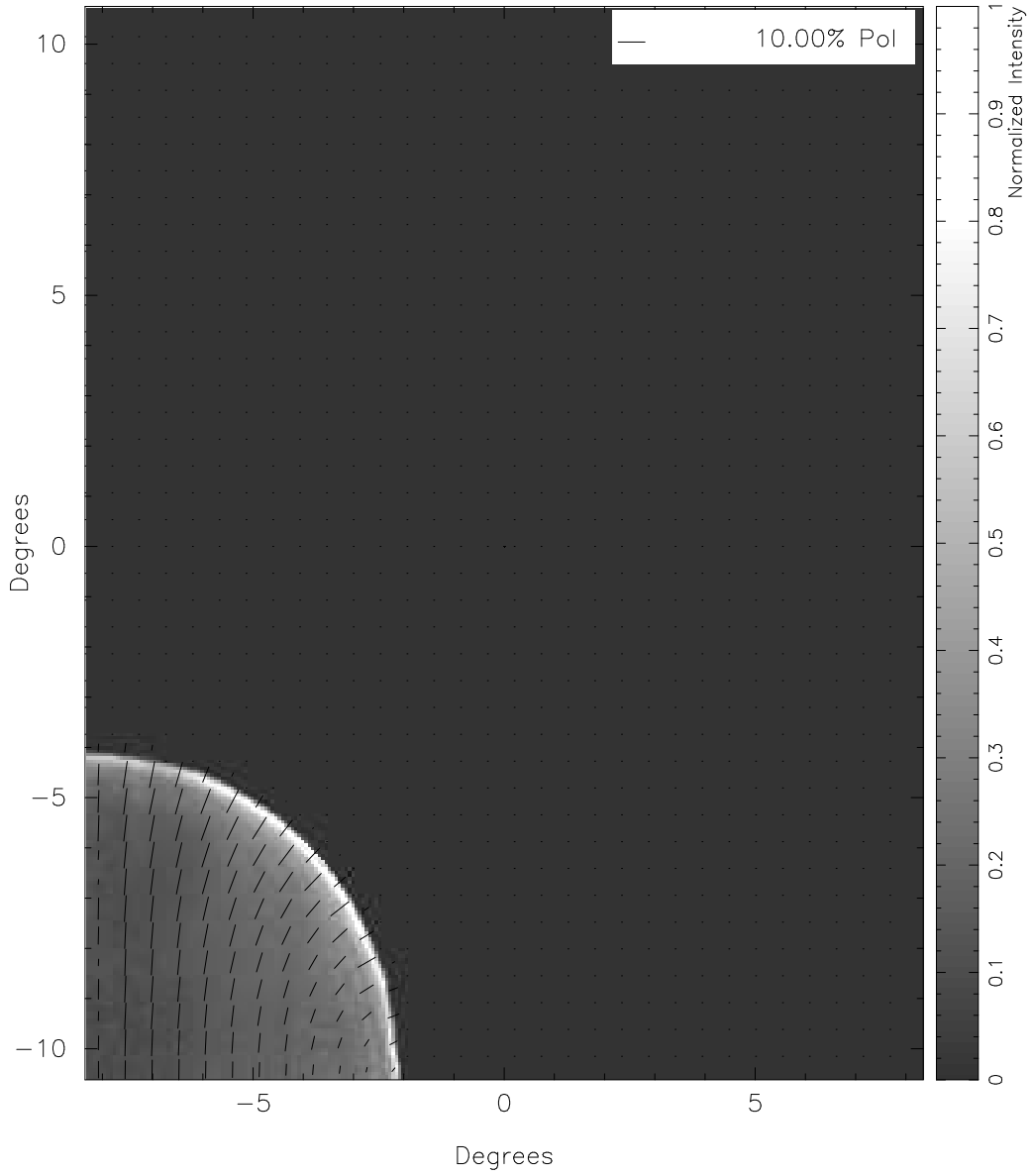

Figure 5.10 Polarization map of 100 micron dust emission from a simulation of a superbubble with a line of sight perpendicular to undisturbed magnetic field at 1kpc distance from observers ($(b, l) = (0, 0)$). Foreground and background neglected. Superbubble aged 0.5 Myrs with a luminosity of $3x10^{39} ergss^{-1}$. Resolution 4 arcmin for intensity, polarization vectors have a resolution of 32 arcmin.

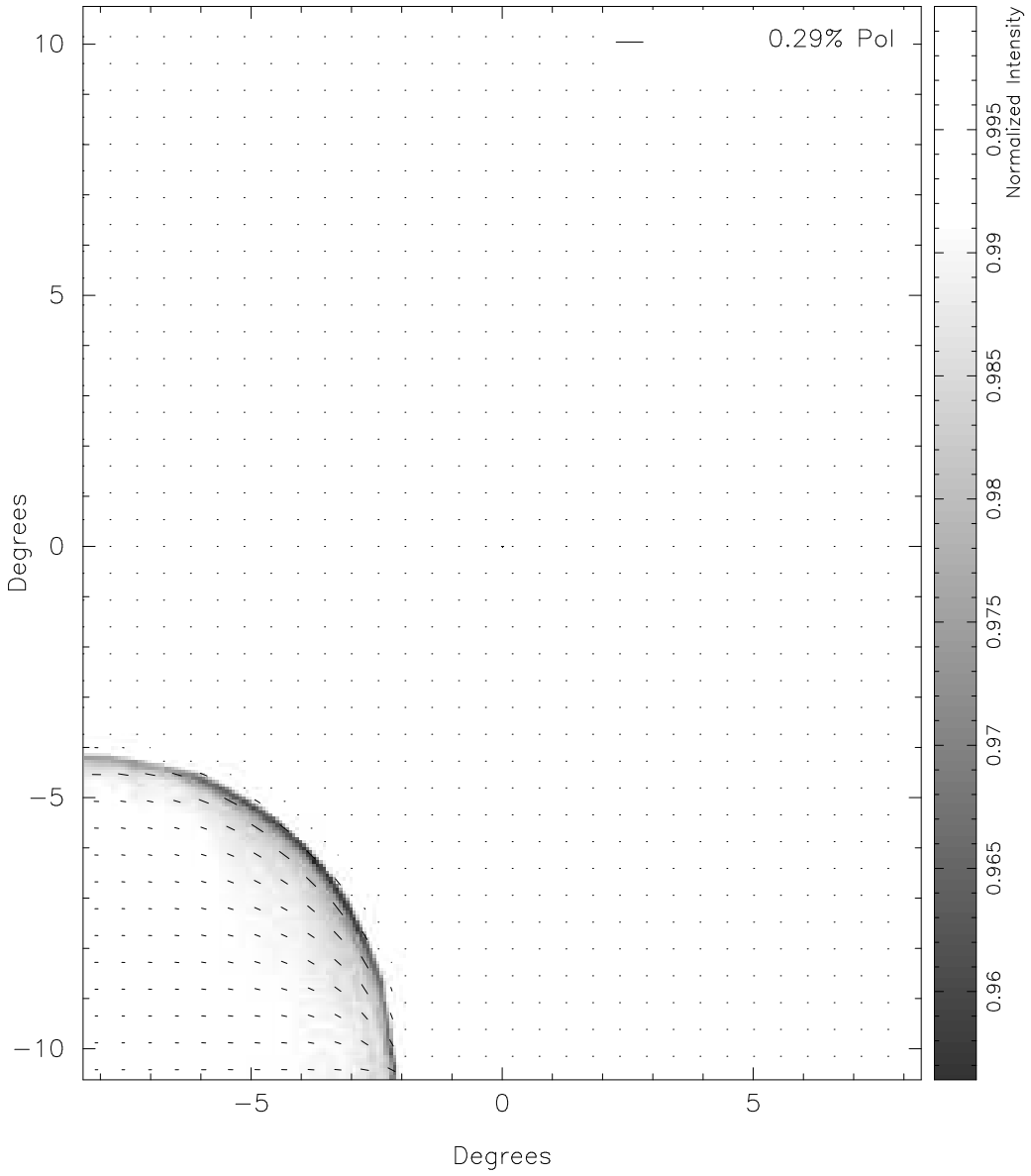

Figure 5.11 Polarization map of 2.2 micron unpolarized starlight passing through a simulation of a superbubble with a line of sight perpendicular to undisturbed magnetic field at 1kpc distance from observers ($(b, l) = (0, 0)$). Foreground and background neglected. Superbubble aged 0.5 Myrs with a luminosity of $3x10^{39} ergss^{-1}$. Resolution 4 arcmin for intensity, polarization vectors have a resolution of 32 arcmin.

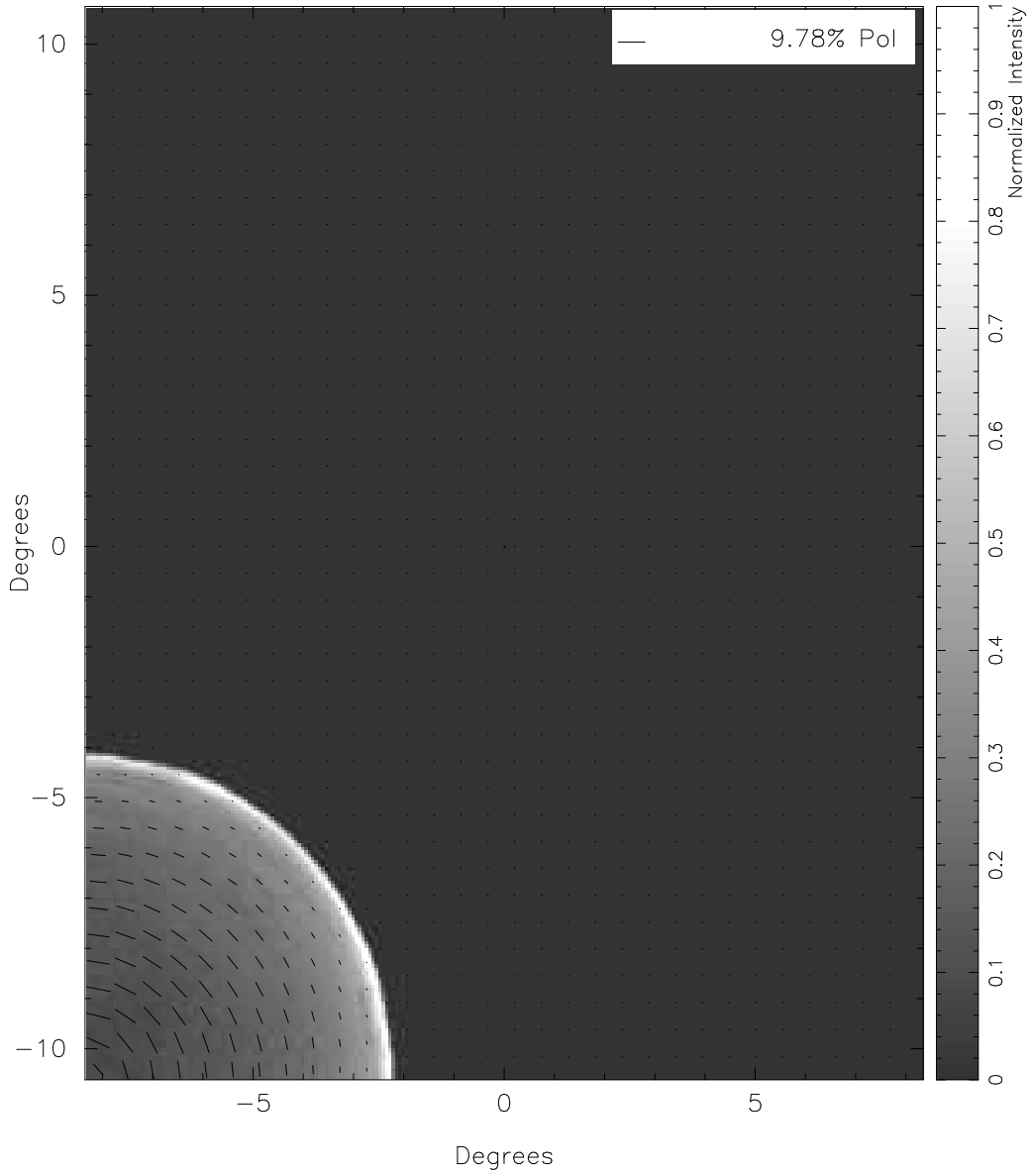

Figure 5.12 Polarization map of 100 micron dust emission from a simulation of a superbubble with a line of sight parallel to the undisturbed magnetic field at 1kpc distance from observers ($(b, l) \sim (80, 0)$) Foreground and background neglected. Superbubble aged 0.5 Myrs with a luminosity of $3x10^{39} ergs s^{-1}$. Resolution 4 arcmin for intensity, polarization vectors have a resolution of 32 arcmin.

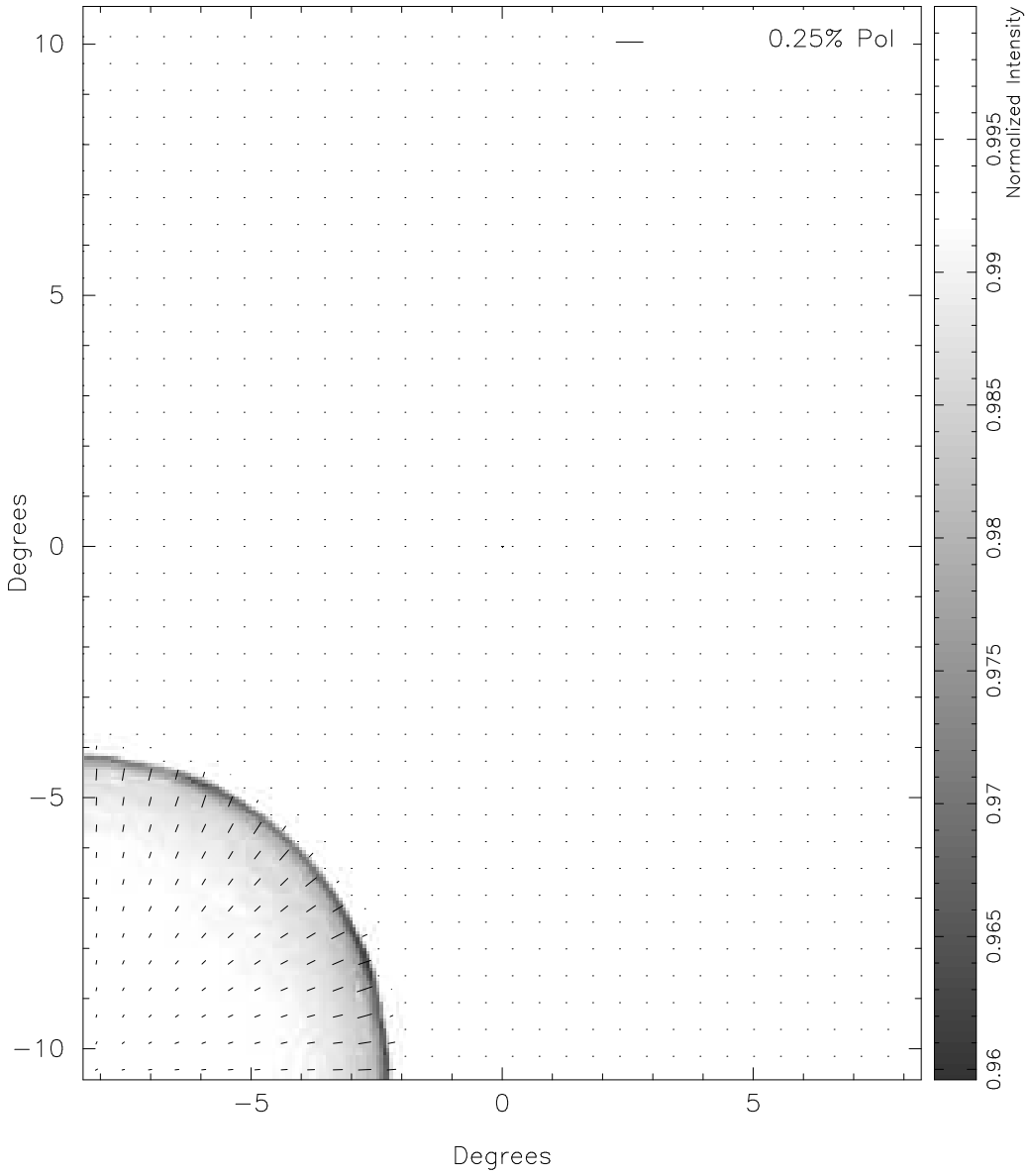

Figure 5.13 Polarization map of 2.2 micron unpolarized starlight passing through a simulation of a superbubble with a line of sight parallel to the undisturbed magnetic field at 1kpc distance from observers ($(b, l) \sim (80, 0)$) Foreground and background neglected. Superbubble aged 0.5 Myrs with a luminosity of $3x10^{39} ergss^{-1}$. Resolution 4 arcmin for intensity, polarization vectors have a resolution of 32 arcmin.

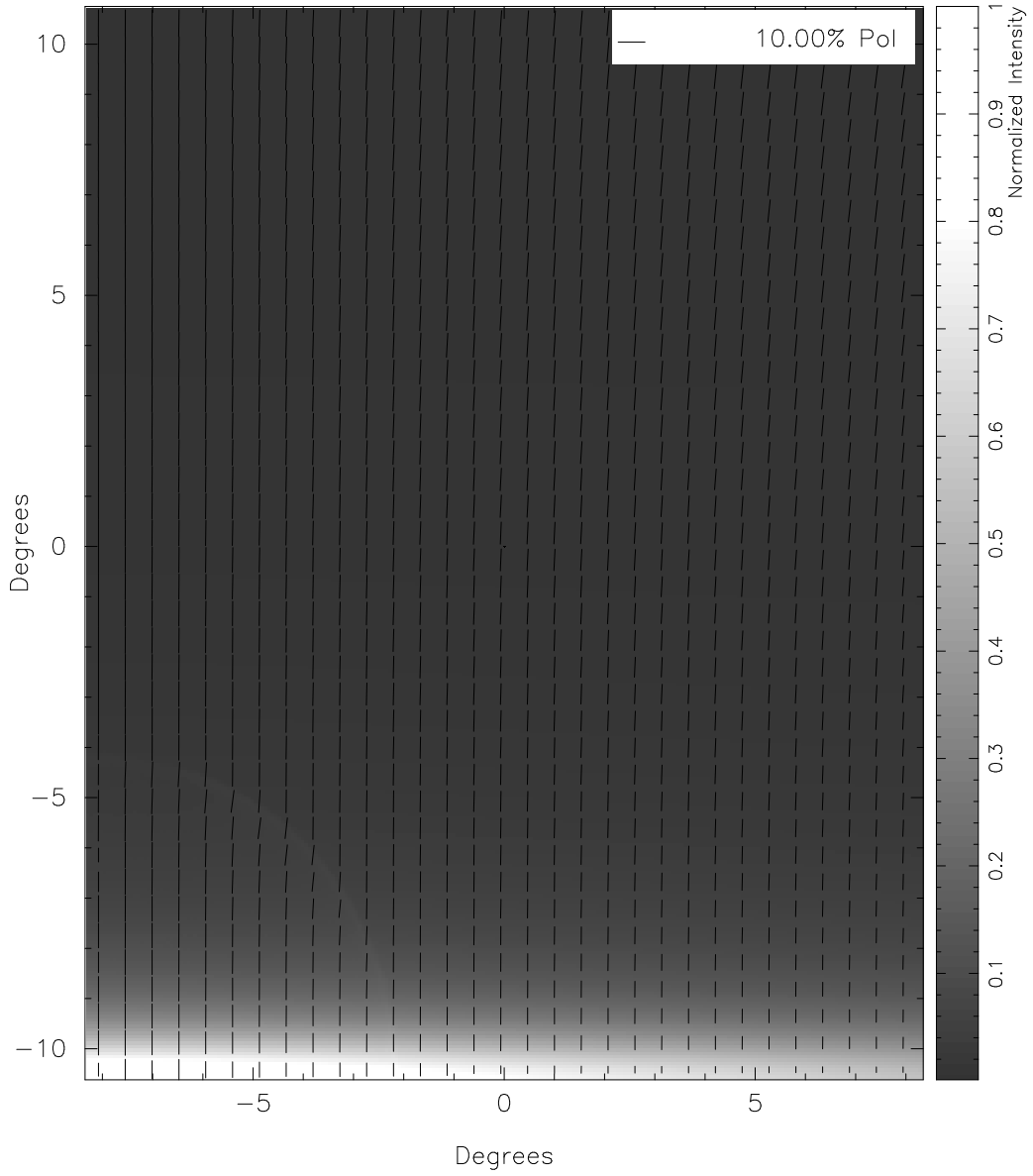

Figure 5.14 Polarization map of 100 micron dust emission from a simulation of a superbubble with a line of sight perpendicular to undisturbed magnetic field at 1kpc distance from observers ($(b, l) = (0, 0)$). Foreground and background included. Superbubble aged 0.5 Myrs with a luminosity of $3x10^{39} ergss^{-1}$. Resolution 4 arcmin for intensity, polarization vectors have a resolution of 32 arcmin.

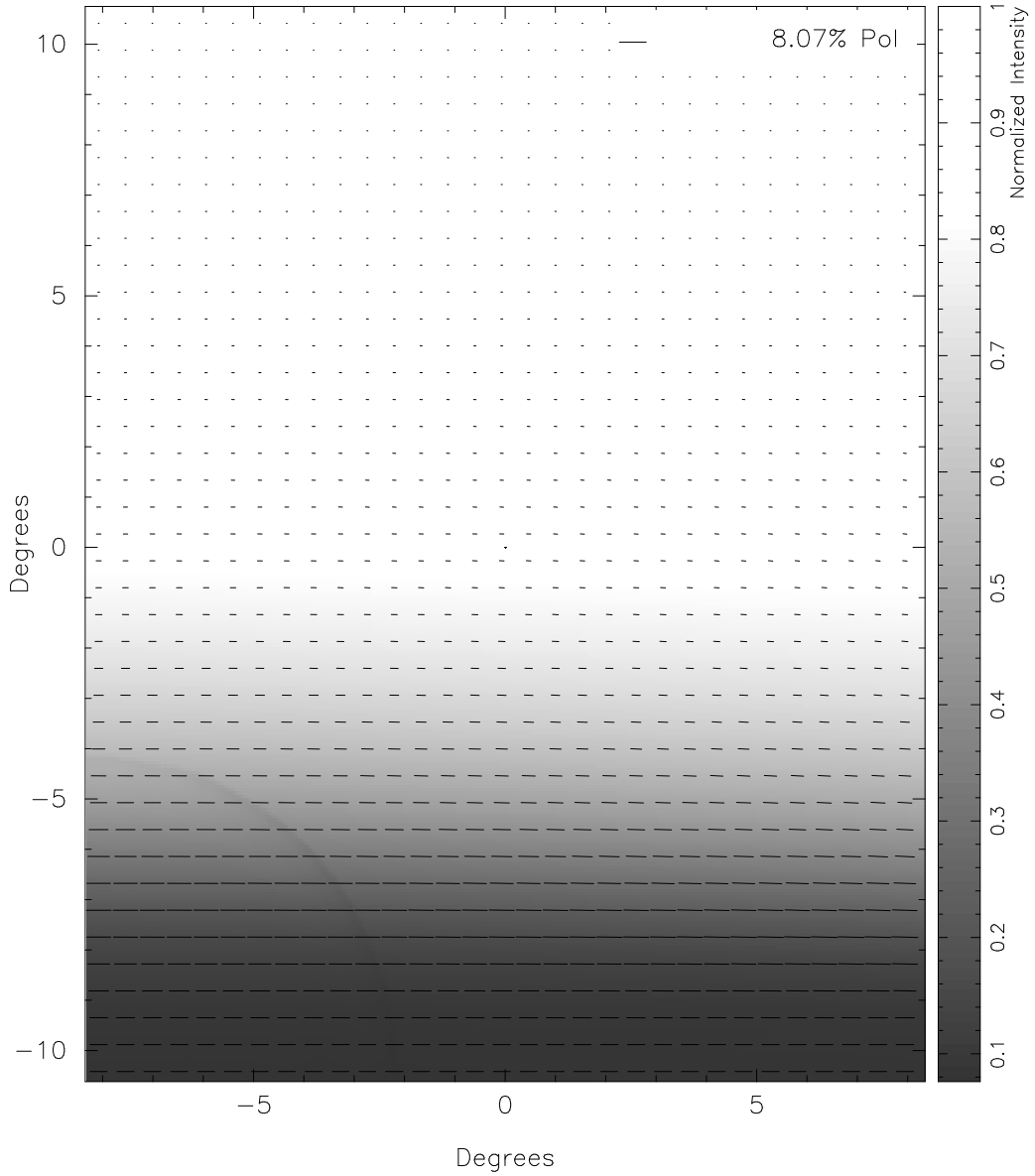

Figure 5.15 Polarization map of 2.2 micron unpolarized starlight passing through a simulation of a superbubble with a line of sight perpendicular to undisturbed magnetic field at 1kpc distance from observers ($(b, l) = (0, 0)$). Foreground and background included. Superbubble aged 0.5 Myrs with a luminosity of $3x10^{39} ergss^{-1}$. Resolution 4 arcmin for intensity, polarization vectors have a resolution of 32 arcmin.

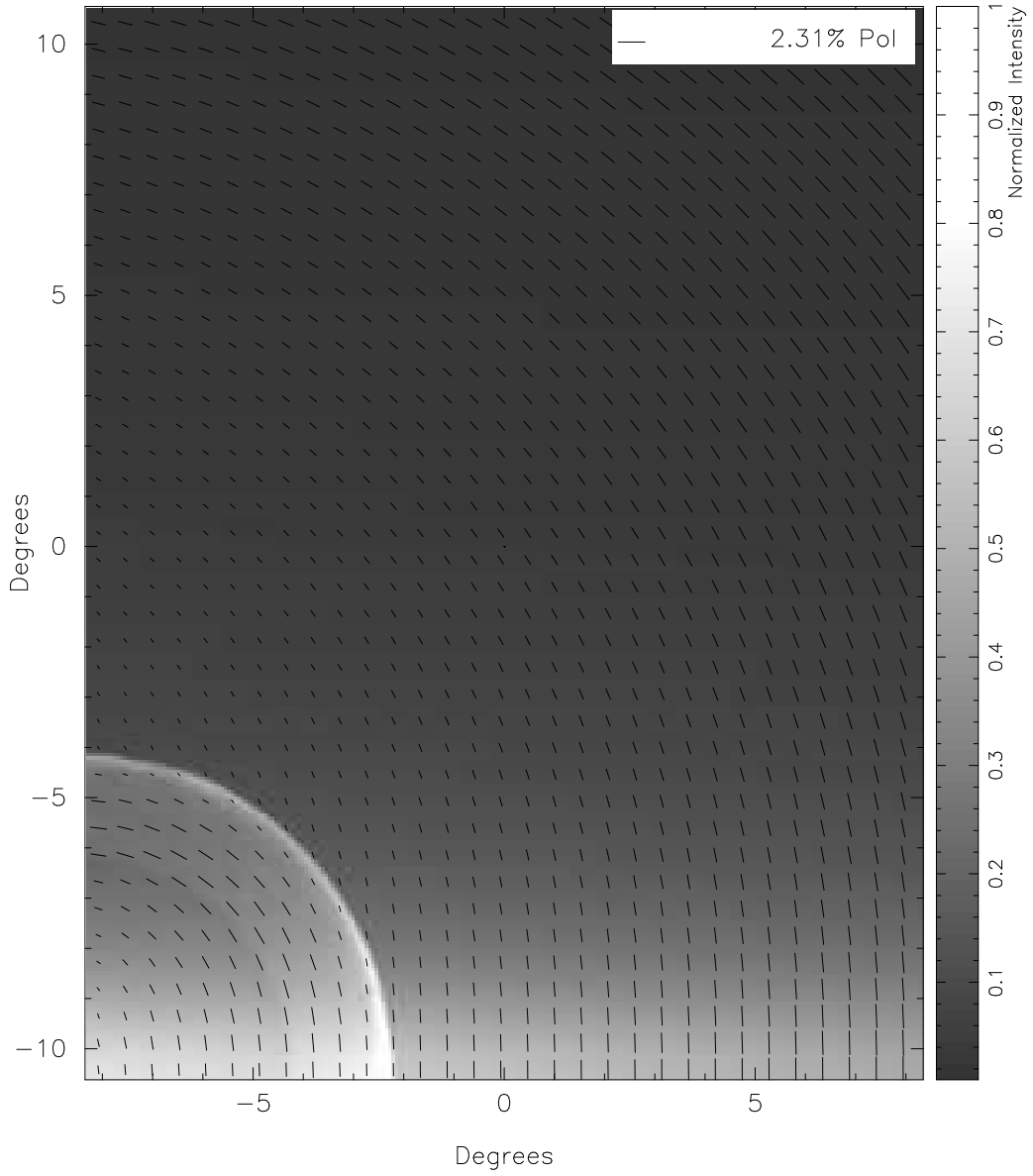

Figure 5.16 Polarization map of 100 micron dust emission from a simulation of a superbubble with a line of sight parallel to the undisturbed magnetic field at 1kpc distance from observers ($(b, l) \sim (80, 0)$). Foreground and background included. Superbubble aged 0.5 Myrs with a luminosity of $3x10^{39} ergss^{-1}$. Resolution 4 arcmin for intensity, polarization vectors have a resolution of 32 arcmin.

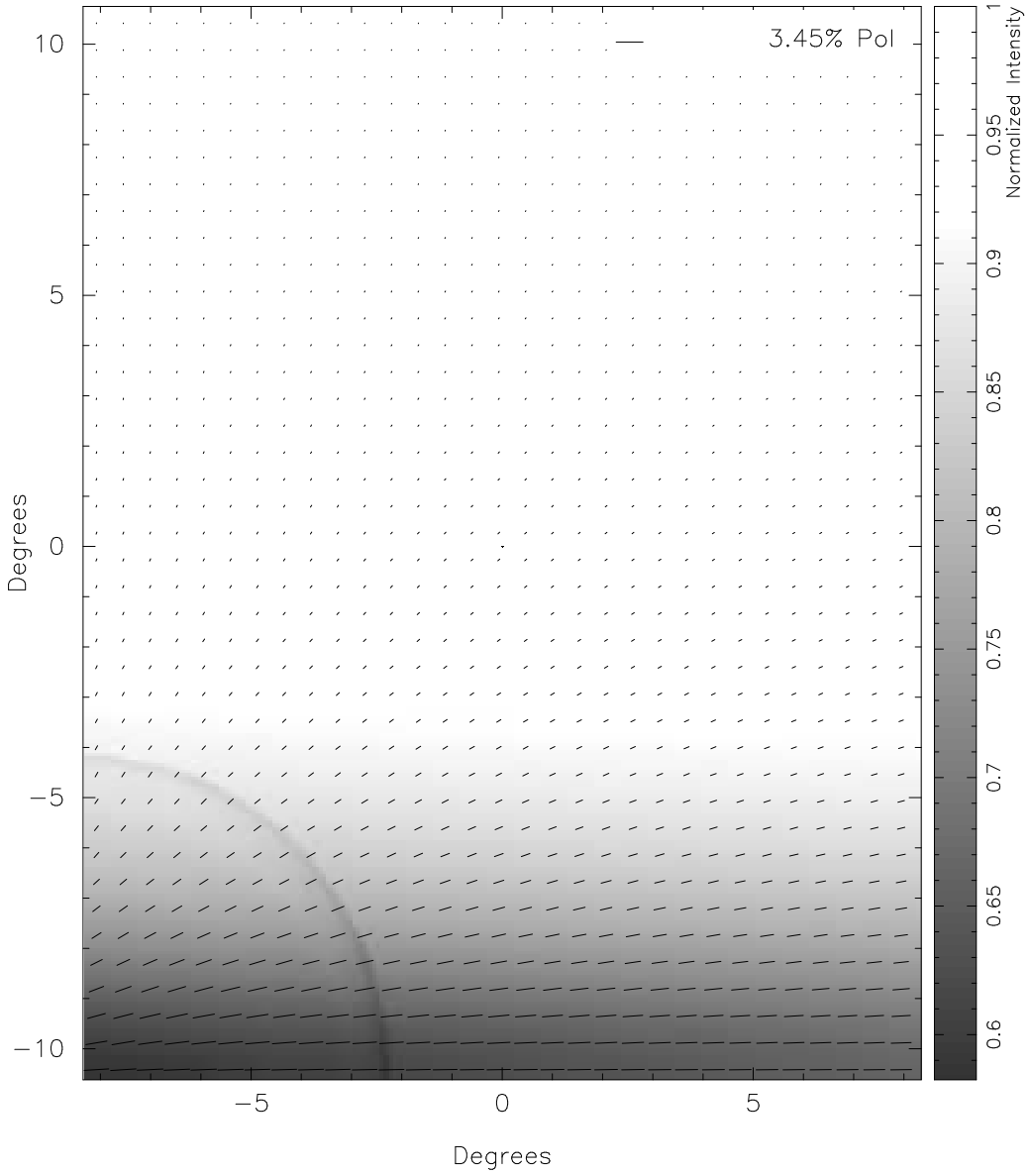

Figure 5.17 Polarization map of 2.2 micron unpolarized starlight passing through a simulation of a superbubble with a line of sight parallel to the undisturbed magnetic field at 1kpc distance from observers ($(b, l) \sim (80, 0)$). Foreground and background included. Superbubble aged 0.5 Myrs with a luminosity of $3x10^{39} ergss^{-1}$. Resolution 4 arcmin for intensity, polarization vectors have a resolution of 32 arcmin.

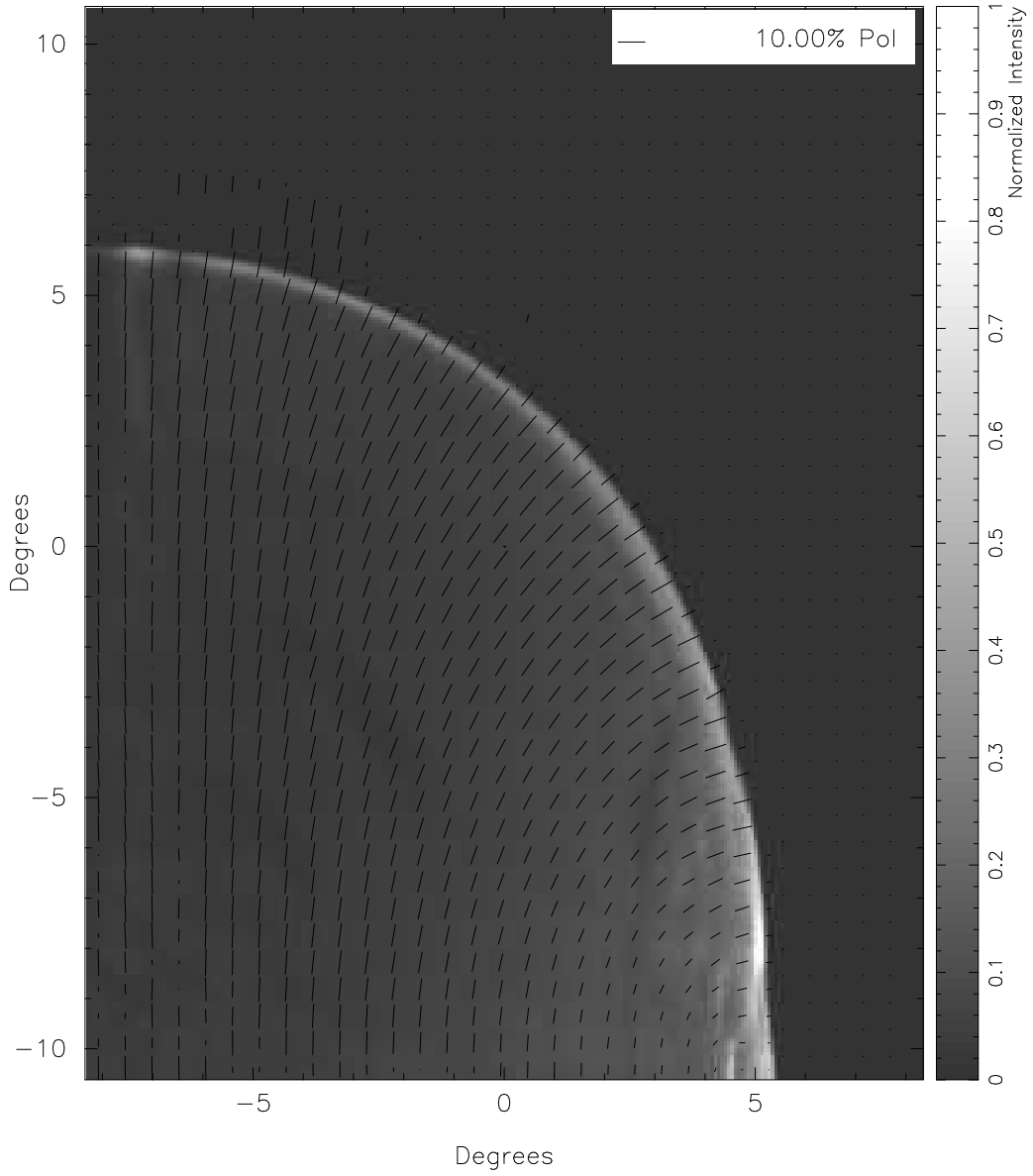

Figure 5.18 Polarization map of 100 micron dust emission from a simulation of a superbubble with a line of sight perpendicular to undisturbed magnetic field at 1kpc distance from observers ($(b, l) = (0, 0)$). Foreground and background neglected. Superbubble aged 2.8 Myrs with a luminosity of $3x10^{39} ergss^{-1}$. Resolution 4 arcmin for intensity, polarization vectors have a resolution of 32 arcmin.

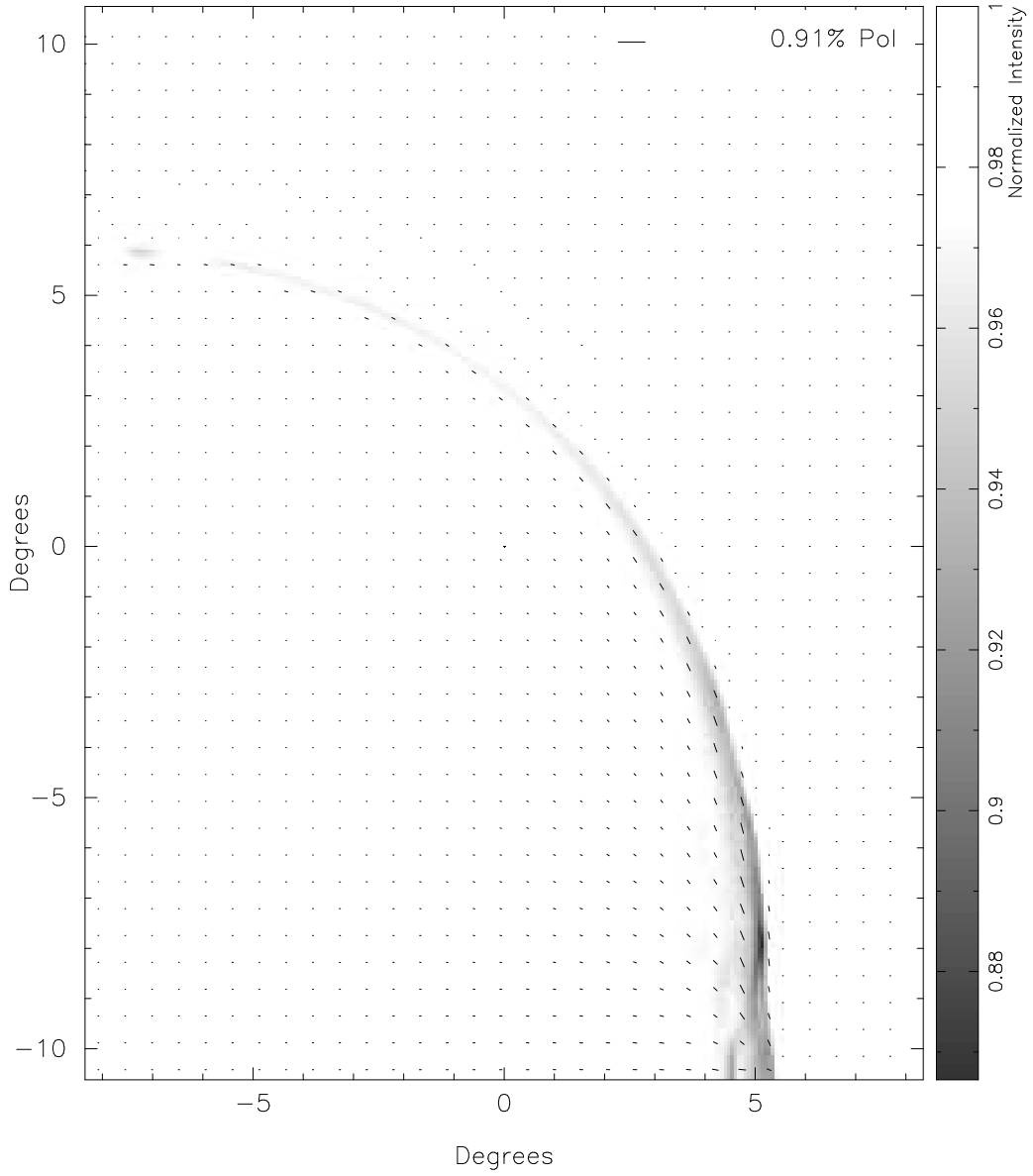

Figure 5.19 Polarization map of 2.2 micron unpolarized starlight passing through a simulation of a superbubble with a line of sight perpendicular to undisturbed magnetic field at 1kpc distance from observers ($(b, l) = (0, 0)$). Foreground and background neglected. Superbubble aged 2.8 Myrs with a luminosity of $3x10^{39} ergss^{-1}$. Resolution 4 arcmin for intensity, polarization vectors have a resolution of 32 arcmin.

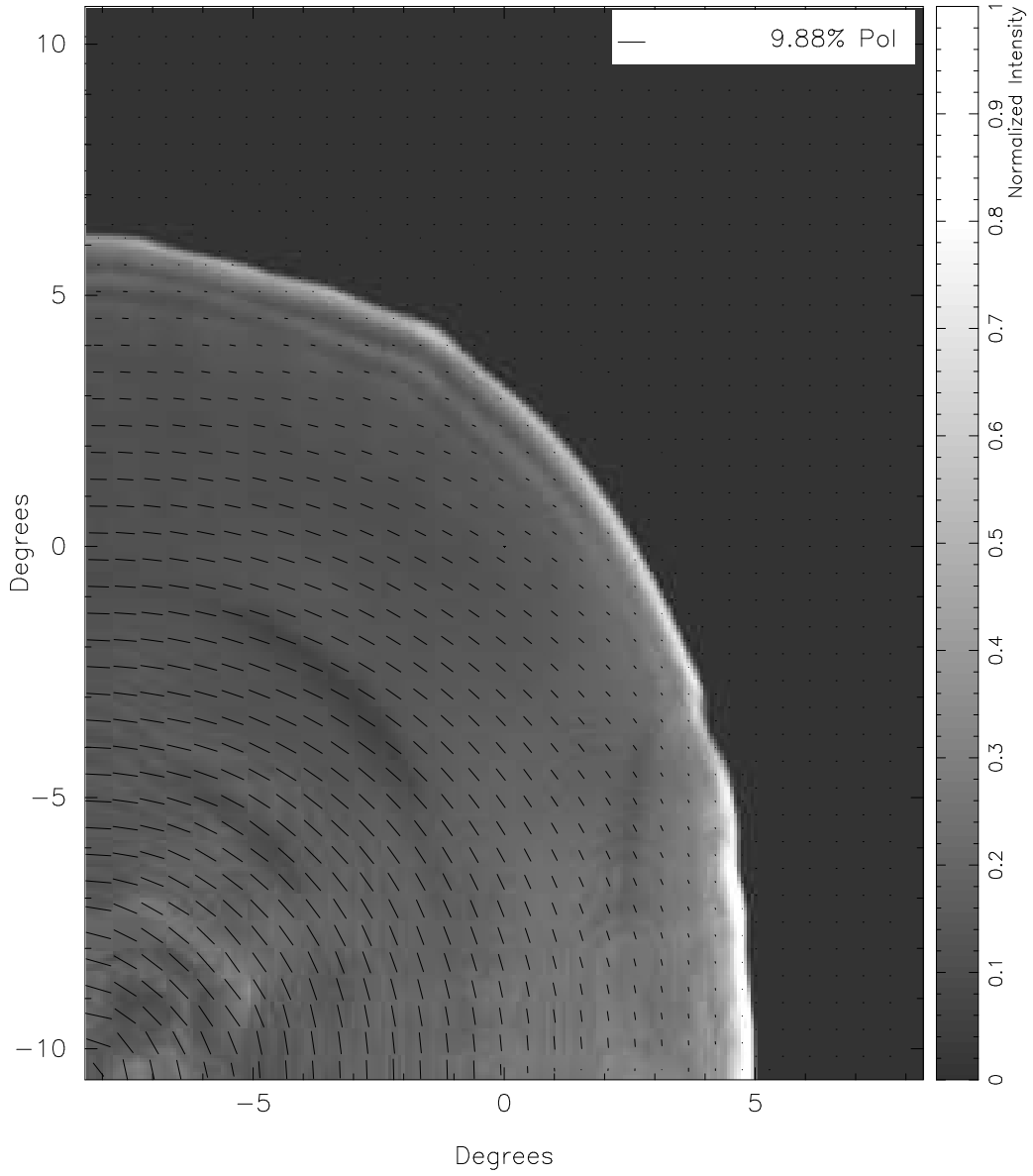

Figure 5.20 Polarization map of 100 micron dust emission from a simulation of a superbubble with a line of sight parallel to the undisturbed magnetic field at 1kpc distance from observers ($(b, l) \sim (80, 0)$) Foreground and background neglected. Superbubble aged 2.8 Myrs with a luminosity of $3x10^{39} ergss^{-1}$. Resolution 4 arcmin for intensity, polarization vectors have a resolution of 32 arcmin.

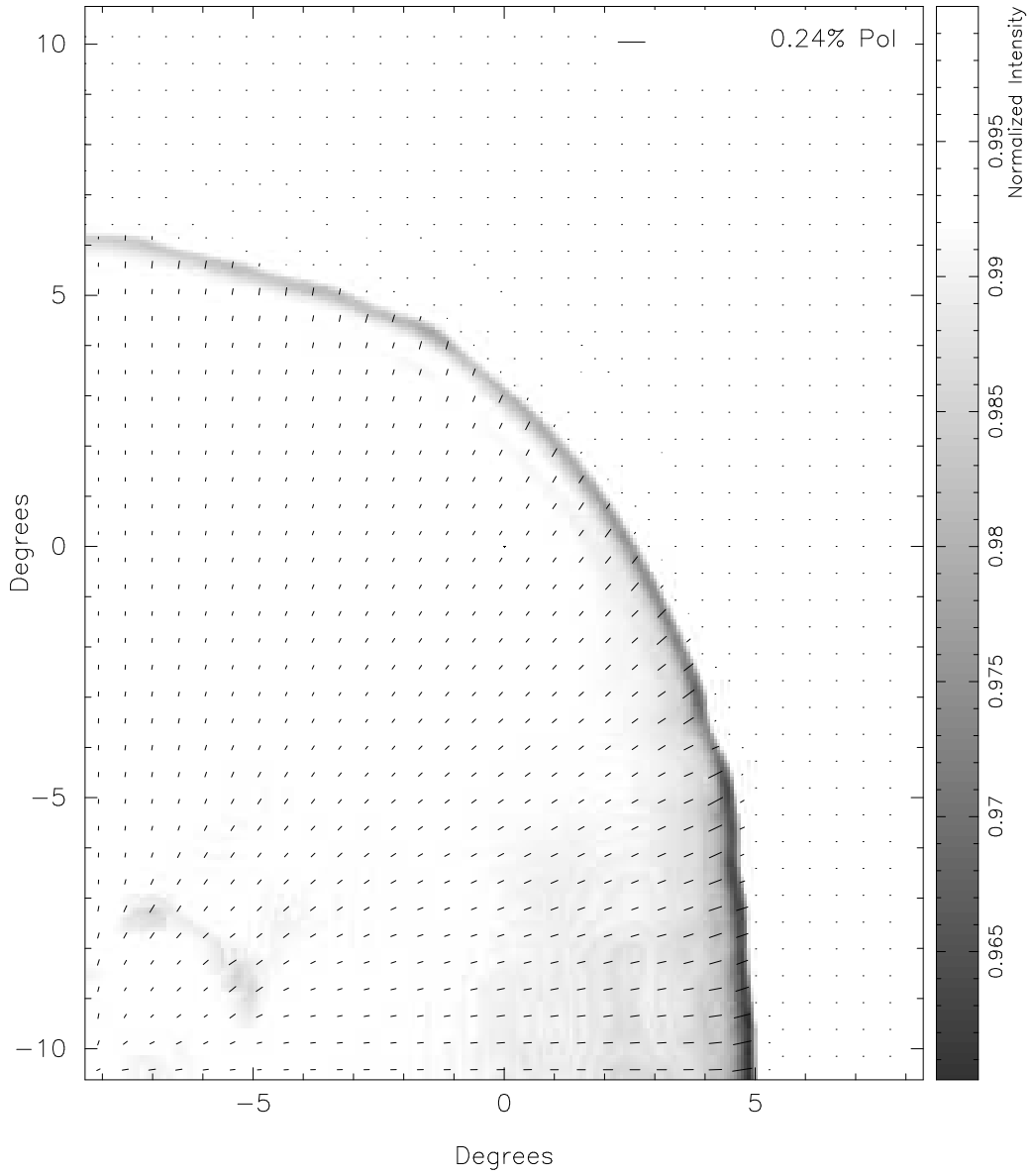

Figure 5.21 Polarization map of 2.2 micron unpolarized starlight passing through a simulation of a superbubble with a line of sight parallel to the undisturbed magnetic field at 1kpc distance from observers ($(b, l) \sim (80, 0)$) Foreground and background neglected. Superbubble aged 2.8 Myrs with a luminosity of $3x10^{39} ergss^{-1}$. Resolution 4 arcmin for intensity, polarization vectors have a resolution of 32 arcmin.

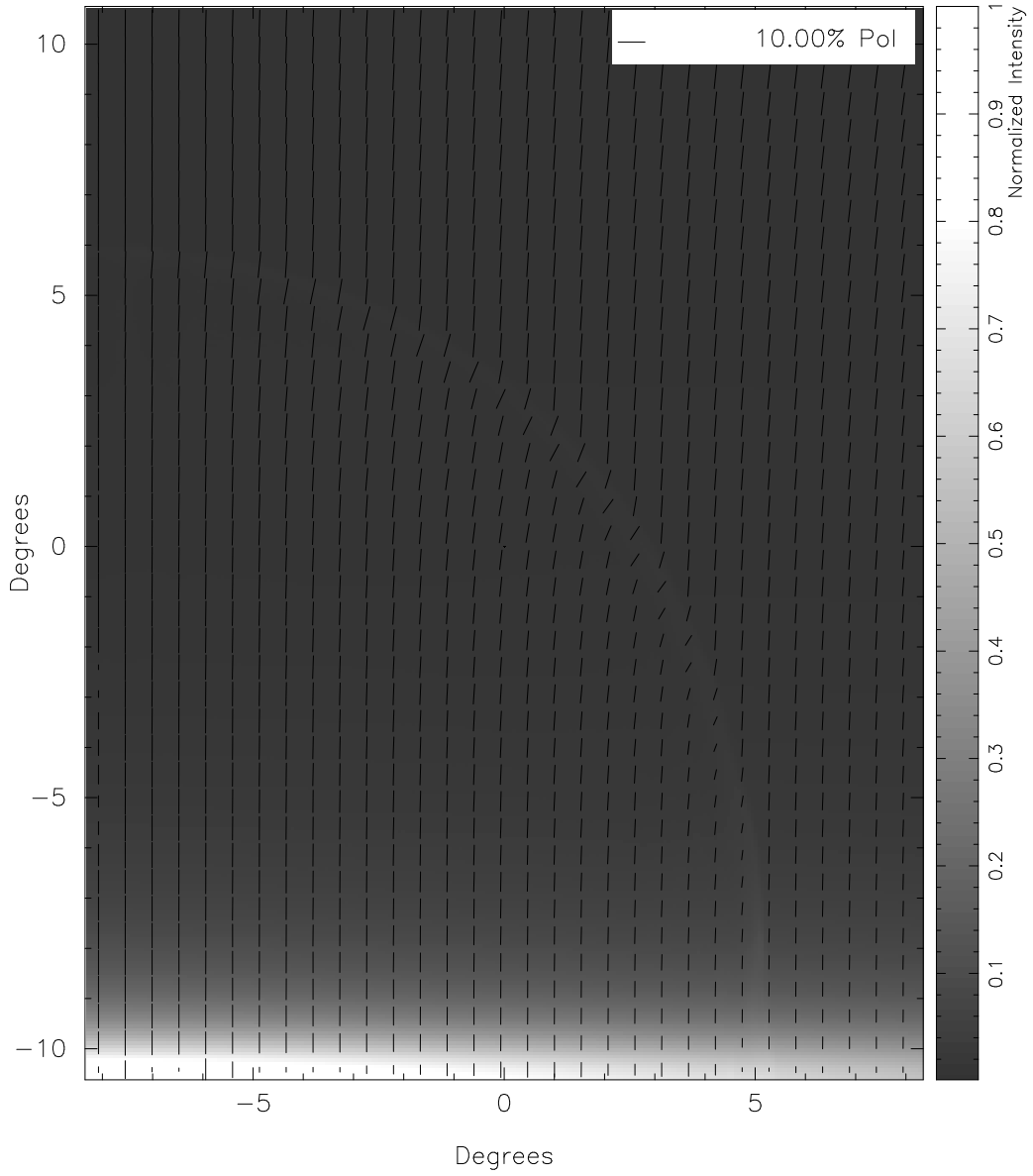

Figure 5.22 Polarization map of 100 micron dust emission from a simulation of a superbubble with a line of sight perpendicular to undisturbed magnetic field at 1kpc distance from observers ($(b, l) = (0, 0)$). Foreground and background included. Superbubble aged 2.8 Myrs with a luminosity of $3x10^{39} ergss^{-1}$. Resolution 4 arcmin for intensity, polarization vectors have a resolution of 32 arcmin.

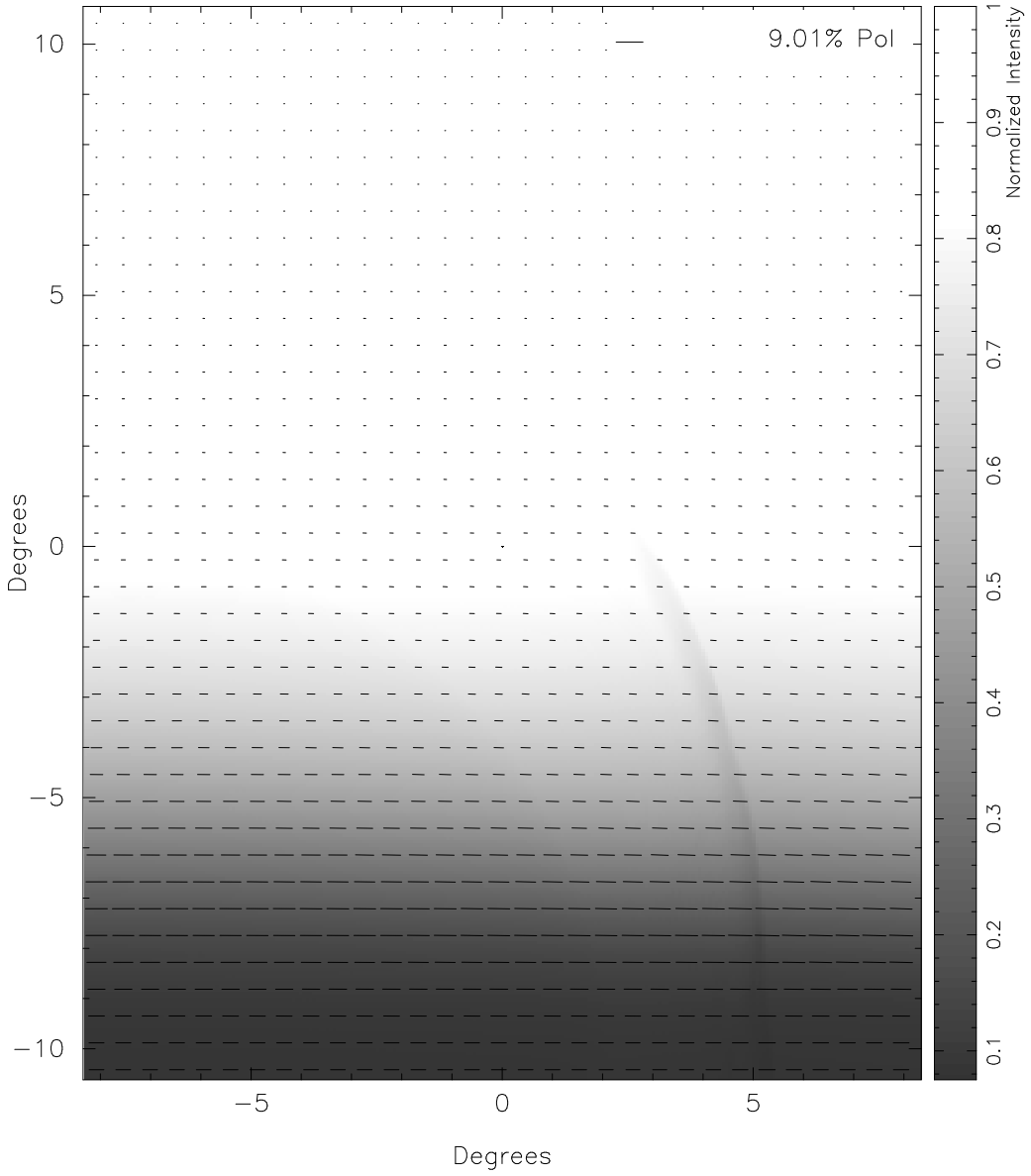

Figure 5.23 Polarization map of 2.2 micron unpolarized starlight passing through a simulation of a superbubble with a line of sight perpendicular to undisturbed magnetic field at 1kpc distance from observers ($(b, l) = (0, 0)$). Foreground and background included. Superbubble aged 2.8 Myrs with a luminosity of $3x10^{39} ergss^{-1}$. Resolution 4 arcmin for intensity, polarization vectors have a resolution of 32 arcmin.

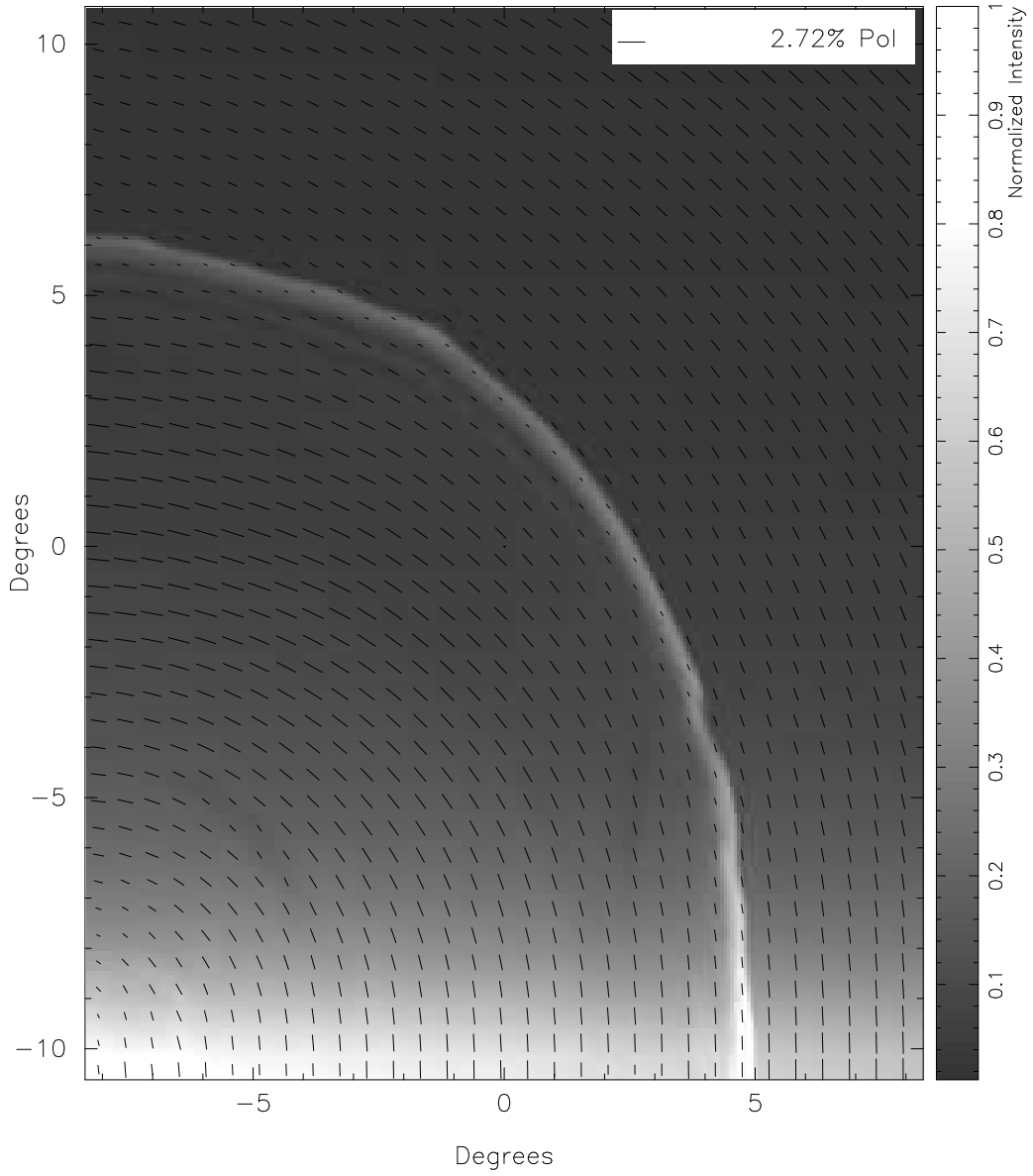

Figure 5.24 Polarization map of 100 micron dust emission from a simulation of a superbubble with a line of sight parallel to the undisturbed magnetic field at 1kpc distance from observers ($(b, l) \sim (80, 0)$). Foreground and background included. Superbubble aged 2.8 Myrs with a luminosity of $3x10^{39} ergss^{-1}$. Resolution 4 arcmin for intensity, polarization vectors have a resolution of 32 arcmin.

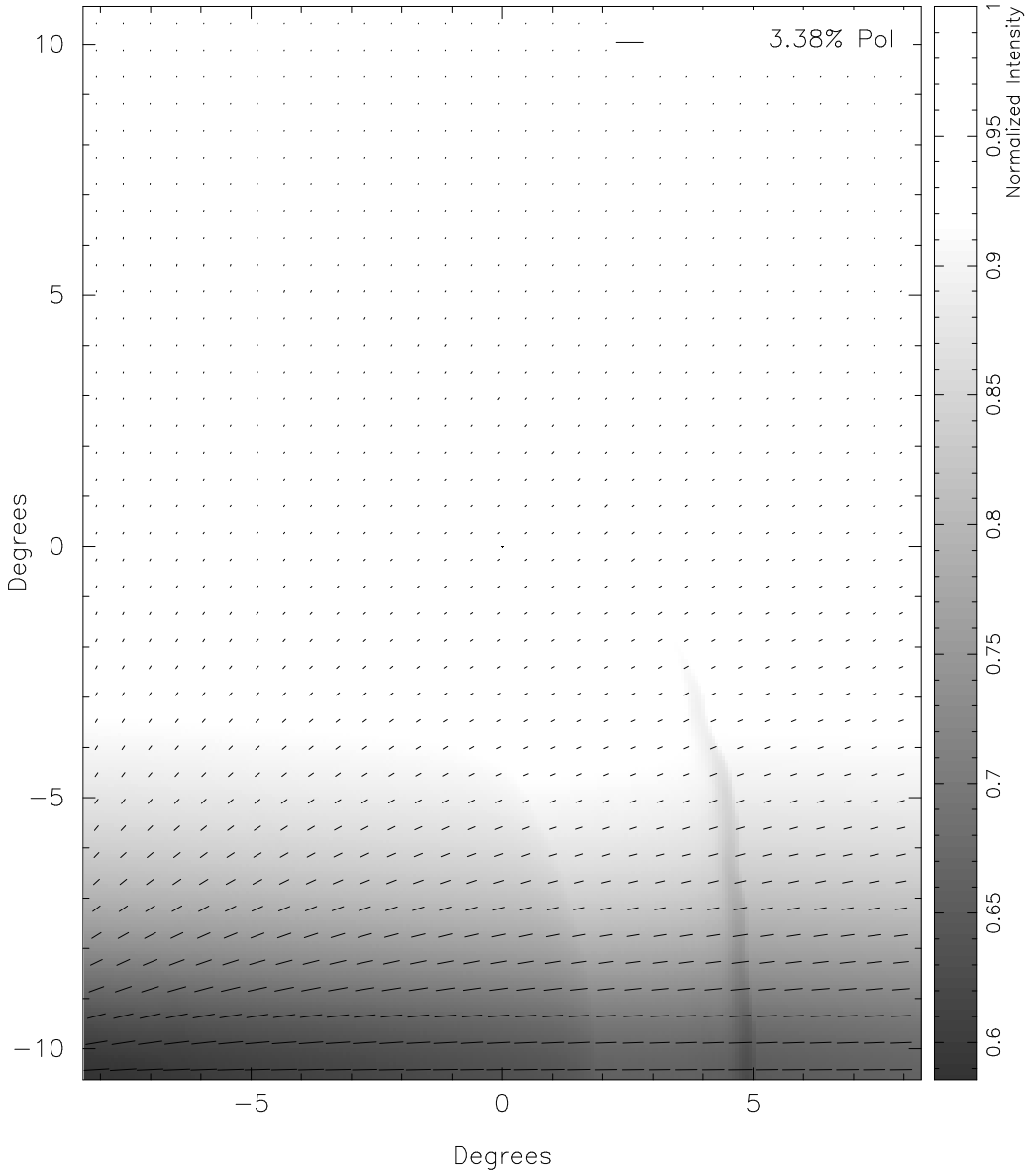

Figure 5.25 Polarization map of 2.2 micron unpolarized starlight passing through a simulation of a superbubble with a line of sight parallel to the undisturbed magnetic field at 1kpc distance from observers ($(b, l) \sim (80, 0)$). Foreground and background included. Superbubble aged 2.8 Myrs with a luminosity of $3x10^{39} ergss^{-1}$. Resolution 4 arcmin for intensity, polarization vectors have a resolution of 32 arcmin.

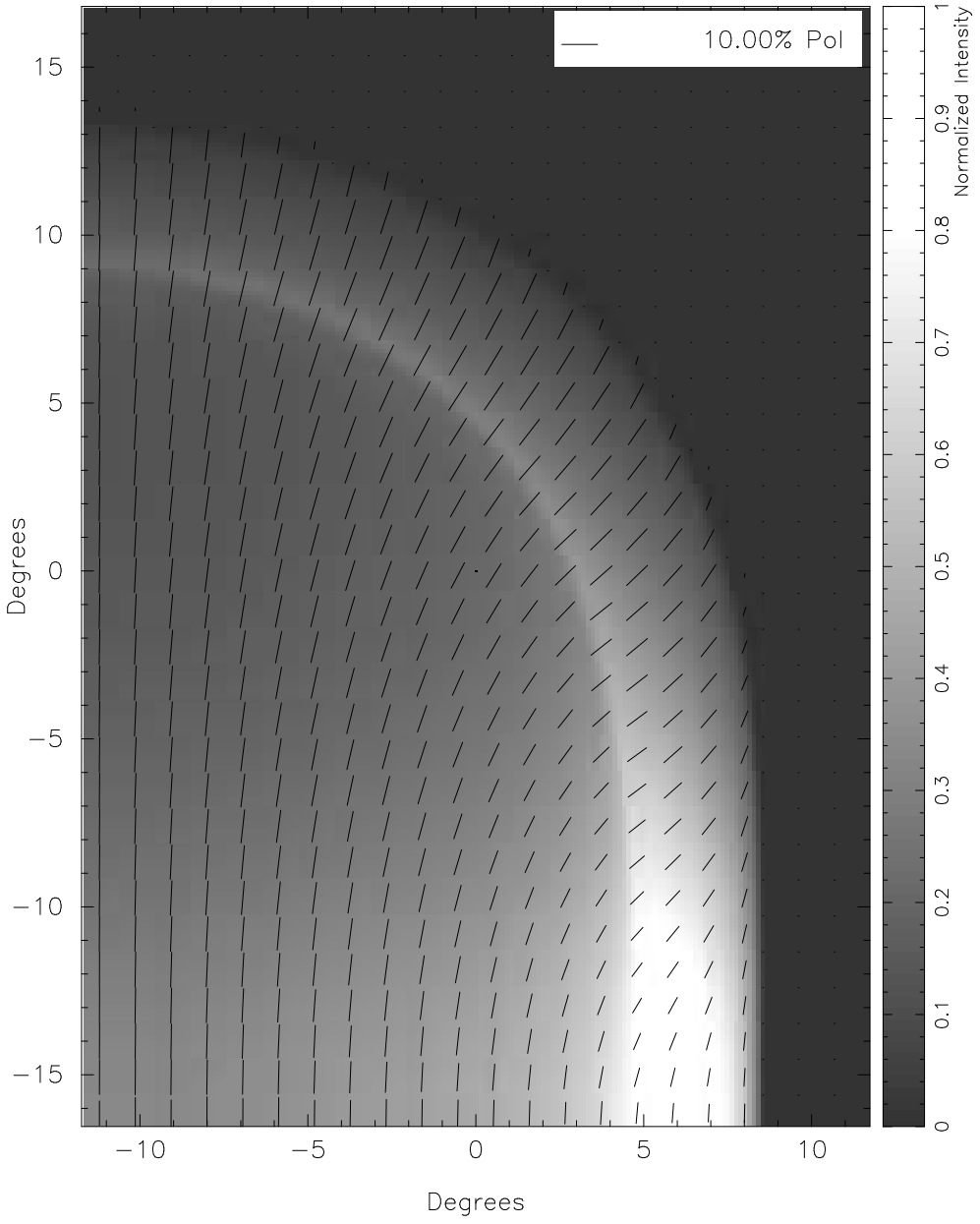

Figure 5.26 Polarization map of 100 micron dust emission from a simulation of a superbubble without cooling with a line of sight perpendicular to undisturbed magnetic field at 1kpc distance from observers ($(b, l) = (0, 0)$). Foreground and background neglected. Superbubble aged 2.8 Myrs with a luminosity of $3x10^{39} ergss^{-1}$. Resolution 8 arcmin for intensity, polarization vectors have a resolution of 64 arcmin.

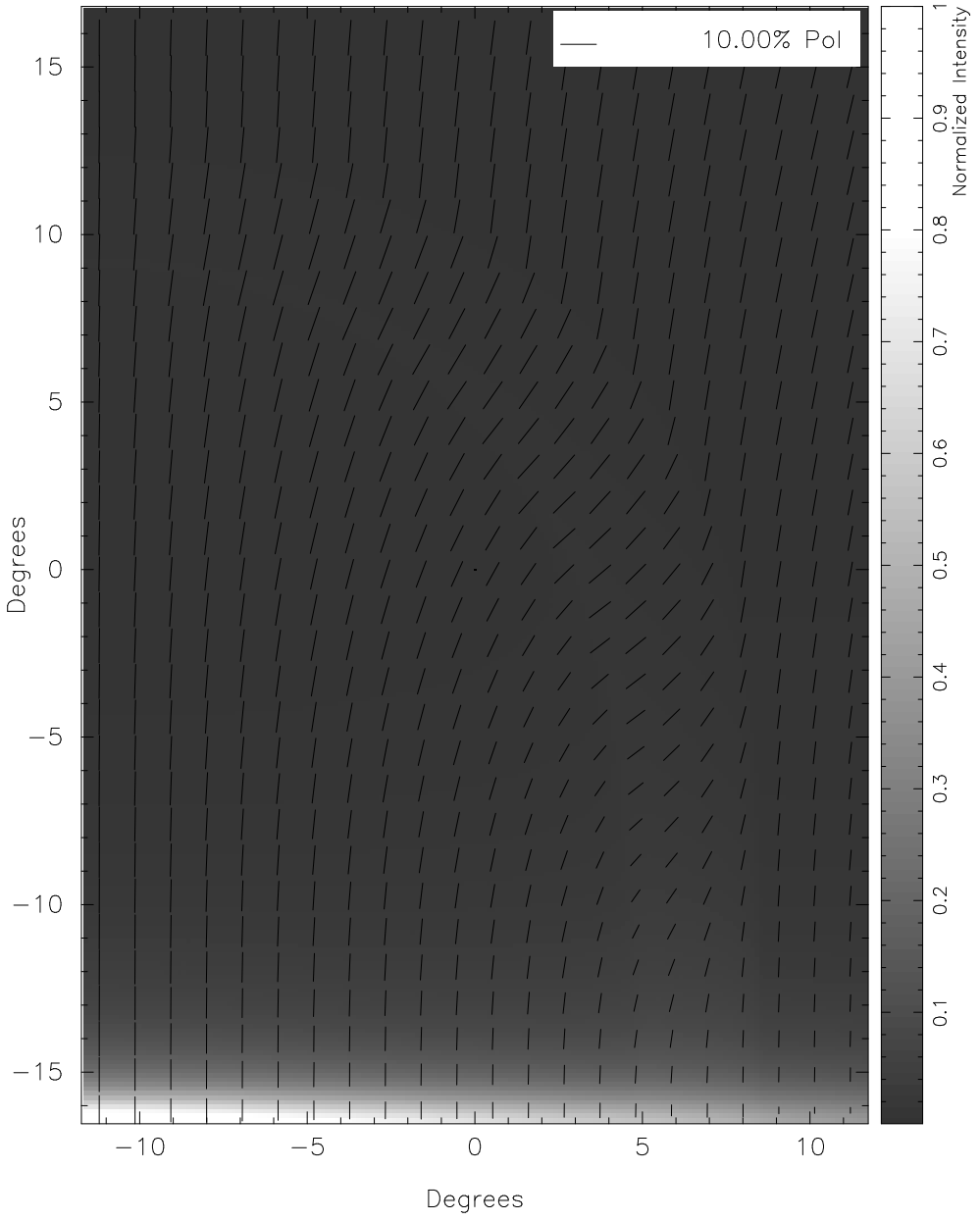

Figure 5.27 Polarization map of 100 micron dust emission from a simulation of a superbubble without cooling with a line of sight perpendicular to undisturbed magnetic field at 1kpc distance from observers ($(b, l) = (0, 0)$). Foreground and background included. Superbubble aged 2.8 Myrs with a luminosity of $3x10^{39} ergss^{-1}$. Resolution 8 arcmin for intensity, polarization vectors have a resolution of 64 arcmin.

Chapter 6

Conclusions and Future Work

6.1 Summary of Results

We created semi-analytical models and 3D MHD numerical simulations of superbubbles in plane-parallel galactic atmospheres. Using the results of these we produced synthetic polarization maps in 100 micron polarized dust emission and 2.2 micron starlight polarized by transmission through dust.

We found that superbubbles can produce magnetic fields with significant vertical components within the shell of the superbubble. The superbubbles that are most efficient at producing vertical magnetic fields are luminous, breakthrough bubbles that are strongly cooled. For the early stages in superbubble development that we were able to model we found that the superbubble did not produce any purely vertical (in the case of transmission) or horizontal (in the case of emission) polarization vectors along the edge of the superbubble image (where the path length through the shell is greatest). However we did find that when our line of sight was parallel to the initial, undisturbed magnetic field that near the center of the superbubble image large vertical (in the case of transmission) or horizontal (in the case of emission) polarization vectors were created.

The effect of contributions to our synthetic polarization maps from a foreground and background was appreciable. Superbubbles that were smaller in physical extent were more difficult, or impossible to discern from the surrounding polarization than extended superbubbles that had expanded preferentially perpendicular to the galactic plane.

6.2 Future Work

There are many avenues left to explore with this research. One of the original goals of this work was to apply our understanding of how superbubbles affect polarization to actual observations of interesting polarization observations or suspected regions of very active star formation. First on the list of potential sources for comparison to our simulated superbubble synthetic polarization maps are NGC 891, M82 and the Local Bubble. Maps of these objects could be reasonably approximated with minor modifications to our existing GRIZZLYEYE software if we were able to first create appropriate simulations.

However, we know that our simulations of superbubbles are significantly hindered by our dramatically under-resolving the forward shock and contact discontinuity. It is possible that we do not reproduce theoretical shell densities and widths, particularly for the strongly cooled superbubbles because we do not have a large enough resolution. Since AMR reduces the computational effort to simulate fluid dynamics over a large range in scales AMR may be the next step in modeling these large objects with thin shells. The next version of WOMBAT, WOMBAT 2.0 is already in progress and will include AMR.

With a working AMR 3D MHD code we could model a cooled superbubble more accurately and for longer into the superbubble's development. A major deficiency of this work is the inability to properly address the post-shock evolution of the magnetic field. Without an analytical description of this behavior, numerical methods are vital. Without reliably resolving the problem, however, our numerical descriptions of the field evolution are suspect. With AMR we could better simulate the post-shock field evolution, and create better synthetic polarization maps to compare to real observations. The pieces necessary for the generation of vertical magnetic fields by superbubbles are likely there, more accurate simulations would give us the tools to understand this potentially important aspect of galactic magnetic field evolution.

Additionally, future work will focus on more realistic modeling of superbubbles and their environments than was possible within the scope of this work. Aspects of superbubble morphology that we would like to investigate further are the placement of a superbubble relative to the galactic mid-plane, a non-static, non-centrally located

injection region (modeling the superbubble with discreet SNII) and the effect of various galactic environments, including dwarf galaxies. With more realistic simulation environments, our fore and background modeling can also become more sophisticated.

6.3 Conclusions

It is the conclusion of this work that polarization from superbubbles for a few cases is possible. The level of contribution to the polarizing intensity from sources along the light of sight is a large determining factor in the detectability of superbubble polarization. Polarization observations that are attributed to energetic stellar feedback should demonstrate a favorable line of sight and a very energetic stellar population. Superbubbles of small physical extent, or those obscured by dense foregrounds are not likely to be observed with polarized dust emission or starlight polarized by aligned grains.

References

Basu, S., Johnstone, D., & Martin, P. G. 1999, ApJ, 516, 843

Beck, R. 2009, Astrophysics and Space Sciences Transactions, 5, 43

Castor, J., McCray, R., & Weaver, R. 1975a, ApJ, 200, L107

Castor, J. I., Abbott, D. C., & Klein, R. I. 1975b, ApJ, 195, 157

Chu, Y.-H. 2008, in IAU Symposium, Vol. 250, IAU Symposium, ed. F. Bresolin, P. A. Crowther, & J. Puls, 341–354

Clemens, D. P., Pinnick, A. F., Pavel, M. D., & Taylor, B. W. 2012, ApJS, 200, 19

Dalgarno, A. & McCray, R. A. 1972, ARA&A, 10, 375

Davis, Jr., L. & Greenstein, J. L. 1951, ApJ, 114, 206

de Avillez, M. A. & Breitschwerdt, D. 2005, A&A, 436, 585

Dickey, J. M. & Lockman, F. J. 1990, ARA&A, 28, 215

Draine, B. T. 2003, ARA&A, 41, 241

Everett, J. E. & Churchwell, E. 2010, ApJ, 713, 592

Ferrière, K. M. 2001, Reviews of Modern Physics, 73, 1031

Ferriere, K. M., Mac Low, M., & Zweibel, E. G. 1991, ApJ, 375, 239

Gaetz, T. J. & Salpeter, E. E. 1983, ApJS, 52, 155

Heckman, T. M., Armus, L., & Miley, G. K. 1990, ApJS, 74, 833

Heiles, C. 1990, ApJ, 354, 483

Jones, T. J. 1993, ApJ, 403, 135

—. 1997, AJ, 114, 1393

—. 2000, AJ, 120, 2920

Jones, T. W. & Odell, S. L. 1977, ApJ, 214, 522

Kerr, F. J. & Lynden-Bell, D. 1986, MNRAS, 221, 1023

Kompaneets, A. S. 1960, Soviet Physics Doklady, 5, 46

Koo, B.-C. & McKee, C. F. 1992, ApJ, 388, 103

Korpi, M. J., Tuominen, I., Brandenburg, A., & Shukurov, A. 1999, in Astronomical Society of the Pacific Conference Series, Vol. 168, New Perspectives on the Interstellar Medium, ed. A. R. Taylor, T. L. Landecker, & G. Joncas, 445

Kothes, R. & Brown, J.-A. 2009, in IAU Symposium, Vol. 259, IAU Symposium, ed. K. G. Strassmeier, A. G. Kosovichev, & J. E. Beckman, 75–80

Mac Low, M. & McCray, R. 1988, ApJ, 324, 776

Mac Low, M., McCray, R., & Norman, M. L. 1989, ApJ, 337, 141

Mendygral, P. J. 2011, PhD thesis, University of Minnesota

Newman, W. I., Symbalisty, E. M. D., Ahrens, T. J., & Jones, E. M. 1999, , 138, 224

Olano, C. A. 2009, A&A, 506, 1215

Ponthieu, N., Macías-Pérez, J. F., Tristram, M., Ade, P., Amblard, A., Ansari, R., Aumont, J., Aubourg, É., Benoît, A., Bernard, J., Blanchard, A., Bock, J. J., Bouchet, F. R., Bourrachot, A., Camus, P., Cardoso, J., Couchot, F., de Bernardis, P., Delabrouille, J., Désert, F., Douspis, M., Dumoulin, L., Filliatre, P., Fosalba, P., Giard, M., Giraud-Héraud, Y., Gispert, R., Grain, J., Guglielmi, L., Hamilton, J., Hanany, S., Henrot-Versillé, S., Kaplan, J., Lagache, G., Lange, A. E., Madet, K., Maffei, B., Masi, S., Mayet, F., Nati, F., Patanchon, G., Perdereau, O., Plaszczynski, S., Piat, M., Prunet, S., Puget, J., Renault, C., Rosset, C., Santos, D., Vibert, D., & Yvon, D. 2005, A&A, 444, 327

Reichborn-Kjennerud, B., Aboobaker, A. M., Ade, P., Aubin, F., Baccigalupi, C., Bao, C., Borrill, J., Cantalupo, C., Chapman, D., Didier, J., Dobbs, M., Grain, J., Grainger, W., Hanany, S., Hillbrand, S., Hubmayr, J., Jaffe, A., Johnson, B., Jones, T., Kisner, T., Klein, J., Korotkov, A., Leach, S., Lee, A., Levinson, L., Limon, M., MacDermid, K., Matsumura, T., Meng, X., Miller, A., Milligan, M., Pascale, E.,

Polsgrove, D., Ponthieu, N., Raach, K., Sagiv, I., Smecher, G., Stivoli, F., Stompor, R., Tran, H., Tristram, M., Tucker, G. S., Vinokurov, Y., Yadav, A., Zaldarriaga, M., & Zilic, K. 2010, in Society of Photo-Optical Instrumentation Engineers (SPIE) Conference Series, Vol. 7741, Society of Photo-Optical Instrumentation Engineers (SPIE) Conference Series

Ryu, D. & Jones, T. W. 1995, ApJ, 442, 228

Ryu, D., Jones, T. W., & Frank, A. 1995, ApJ, 452, 785

Ryu, D., Miniati, F., Jones, T. W., & Frank, A. 1998, ApJ, 509, 244

Serkowski, K., Mathewson, D. S., & Ford, V. L. 1975, ApJ, 196, 261

Stil, J., Wityk, N., Ouyed, R., & Taylor, A. R. 2009, ApJ, 701, 330

Sukumar, S. & Allen, R. J. 1991, ApJ, 382, 100

Tenorio-Tagle, G., Rozyczka, M., & Bodenheimer, P. 1990, A&A, 237, 207

The Planck Collaboration. 2006, ArXiv Astrophysics e-prints

Tomisaka, K. 1992, PASJ, 44, 177

Tomisaka, K. & Ikeuchi, S. 1986, PASJ, 38, 697

Townsend, R. H. D. 2009, ApJS, 181, 391

Veltz, L., Bienaymé, O., Freeman, K. C., Binney, J., Bland-Hawthorn, J., Gibson, B. K., Gilmore, G., Grebel, E. K., Helmi, A., Munari, U., Navarro, J. F., Parker, Q. A., Seabroke, G. M., Siebert, A., Steinmetz, M., Watson, F. G., Williams, M., Wyse, R. F. G., & Zwitter, T. 2008, A&A, 480, 753

Weaver, R., McCray, R., Castor, J., Shapiro, P., & Moore, R. 1977, ApJ, 218, 377